Exploring the Relationship Between Crustal Permeability and Hydrothermal Venting at Mid-ocean Ridges Using Numerical Models

Shreya Singh

Dissertation submitted to the Faculty of the
Virginia Polytechnic Institute and State University
in partial fulfillment of the requirements for the degree of

Doctor of Philosophy
in
Geosciences

Robert P. Lowell, Chair
Robert J. Bodnar
Scott D. King
John A. Hole

April 30, 2015
Blacksburg, Virginia

Keywords: Hydrothermal systems, Numerical Modeling, Mid-ocean Ridges, Porous media flows

Exploring the Relationship Between Crustal Permeability and Hydrothermal Venting at Mid-ocean Ridges Using Numerical Models

Shreya Singh

ABSTRACT

Hydrothermal systems associated with oceanic spreading centers account for a quarter of Earth's total heat flux and one third of the heat flux through the ocean floor. Circulation of seawater through these systems alters both the crust and the circulating fluid, impacting global geochemical cycles. The warm vent fluids rich in nutrients support a wide variety of unique biological communities. Thus, understanding hydrothermal processes at oceanic spreading centers is important to provide insight into thermal and biogeochemical processes. In this dissertation I present the results of numerical modeling efforts for mid-ocean ridge hydrothermal systems. In the three manuscripts presented, permeability emerges as a key controlling factor for hydrothermal venting. In the first manuscript, I use 2-D numerical models to find that the distribution of permeability in the crust controls fluid velocity as well as the amount of mixing between hot hydrothermal fluids and cold seawater. This, in turn, effects the temperature and composition of fluids emerging on the surface. For the second manuscript, I construct single-pass 1-D models to show that a sudden increase in permeability caused due to magmatic or seismic events in the seafloor causes a sharp rise in the fluid output of the system. This, in conjunction with steep thermal gradients close to the surface, results in a rapid increase of venting temperatures. In the third manuscript, I develop a particle tracking model to study fluid trajectories in the subsurface. The results show that permeability distribution in the subsurface governs fluid paths and consequently, the residence time of fluids in the crust. Based on the work presented in this document, I conclude that permeability distribution, both local and field scale, exerts a major control on hydrothermal circulation in the subsurface and on the temperature and composition of venting fluids on the surface.

This work was partially supported by NSF Grant OCE-0819084 and OCE 0926418 to RPL, and OCE-0818783 to K.C.L. Partial summer support was provided by the Department of Geoscience, Virginia Tech.

Attributes

Several colleagues participated in the research and aided in the writing of the three manuscripts that comprise this dissertation. A brief description of their contributions are included here.

R.P. Lowell: Dr. Lowell is currently a Professor at the Department of Geoscience, Virginia Tech. He was my advisor for this work and his mentor-ship and patient guidance has enabled me to accomplish the work presented here. He is also a co-author on the three manuscripts presented here

K. C. Lewis: Dr. Lewis is currently an Assistant Professor at the Department of Chemistry and Physics, Monmouth University. She is the primary author of the numerical code FISHES. Without FISHES and her troubleshooting efforts, this work would not have been possible. She is a coauthor on the first manuscript.

I also want to express heartfelt gratitude for my committee members for their valuable suggestions and the reviewers of the first two manuscripts for their acute observations and comments. I want to thank the Department of Geoscience, Virginia Tech for providing the students with an environment conducive to growth and for protecting our child-like curiosities.

Contents

1 Introduction **1**

2 Numerical Modeling of Phase Separation at Main Endeavour Field, Juan de Fuca Ridge **3**

2.1 Introduction 4

2.2 Main Endeavour Field 5

2.2.1 Bathymetry and Structure 6

2.2.2 Thermal data 6

2.3 Numerical Modeling Code FISHES 7

2.4 Model setup 9

2.4.1 Homogenous permeability model 11

2.4.2 Heterogeneous permeability model 11

2.5 Results 12

2.5.1 Homogeneous permeability model 12

2.5.2 Heterogeneous Permeability Model with Layer 2A 17

2.5.3 Heterogeneous permeability with anhydrite shell 17

2.6 Discussion 18

2.6.1 Role of bottom temperature 18

2.6.2 Heterogeneous permeability 19

2.6.3 Low surface salinity at the MEF 19

2.7 Conclusions 20

2.8 References 21

3 Thermal Response of Mid-Ocean Ridge Hydrothermal Systems to Perturbations 26

3.1 Introduction . . . 27

3.2 Response of Hydrothermal Systems to Perturbations at Mid-Ocean Ridges . 28

3.3 Previous Modeling Work . . . 30

3.3.1 Thermal and pressure perturbation mechanisms . . . 30

3.3.2 Effect of a thermal boundary layer and permeability changes associated with diking . . . 31

3.3.3 Motivation . . . 32

3.4 The Classic Single-pass Model . . . 33

3.5 Parametrization . . . 34

3.5.1 East Pacific Rise . . . 36

3.5.2 Main Endeavour Field . . . 36

3.6 Numerical Results . . . 38

3.6.1 Effect of dike width 'w' . . . 38

3.6.2 Effect of dike height 'h' . . . 38

3.6.3 Effect of increase in permeability 'k' . . . 41

3.7 Discussion . . . 45

3.7.1 Vent-Field Scale Single Pass Model . . . 45

3.7.2 Single phase modeling . . . 47

3.7.3 Rapid Response of Hydrothermal Systems to Perturbations . . . 47

3.8 Conclusion . . . 48

3.9 References . . . 51

4 A Particle in Cell Algorithm for Tracing Fluid Trajectories in Seafloor Hydrothermal Systems 54

4.1 Introduction . . . 54

4.2 Recharge Zones and Residence Time in MORHS . . . 56

4.3 The Particle in Cell Method . . . 57

4.3.1 Introduction . . . 57

4.3.2 Algorithm 58
4.4 Model Setup 60
4.5 Results 61
4.5.1 Recharge Zones 62
4.5.2 Along axis models 66
4.5.3 Summary: Recharge zones 66
4.6 Residence Time 67
4.7 Discussion 71
4.8 Conclusion 72
4.9 References 72

A Formulation of the Single-Pass Model **75**
A.1 Boundary Conditions 78
A.2 Initial Conditions 78
A.3 Numerical Results 79
A.4 Generic Model of a Hydrothermal System 79

B Particle in Cell Code **82**
B.1 Main Code 82
B.2 Function: Track Points 85
B.3 Function: Writing Model Parameters 86

List of Figures

2.1 Vent fluid salinity (wt% NaCl) and temperature (^{0}C) data from the MEF. Data from 1988 are from Butterfield et al. [1994]; data from 1990 to 2000 are from Lilley et al. [2003]; and 2005 data are from Foustoukos et al. [2009]. . . 4

2.2 Figure High-resolution (∼5 m) bathymetry map of the Endeavour Integrated Study Site "bulls-eye" the Main Endeavour Field. The bathymetry was collected in 2005 as part of a joint project between the University of Washington, the W.M. Keck Foundation, and NEPTUNE Canada using the autonomous vehicle ABE. http://media.marine-geo.org/image/main-endeavour-field-2012. 5

2.3 Stack of cross-axis line 7 from Van Ark et al. [2007]. Triangles show location of the hydrothermal vent fields. Blue arrows indicate the seismic layer 2A event, and red arrows indicate the AMC reflection. 6

2.4 (Top) Heat flow data from Johnson et al. [2010] are coordinated with the thermal blanket station positions. The easternmost station lies in the topographic low east of the axial valley. Colored circles correspond to recharge (blue), conductive (yellow),and discharge (red). (Bottom) Interpretive cartoon of North Line data from Johnson et al. [2010], with recharge occurring on the valley eastern boundary fault and lateral subsurface transport beneath the valley to discharge on the valley western boundary fault. Sloping dashed line represents the shallower magma chamber beneath the western side of the axial valley. Cartoon dimensions not to scale. 8

2.5 Schematic representation of across-axis model with boundary conditions and bottom boundary temperature profile. (a) Homogenous permeability model, (b) general representation of heterogeneous permeability model with layer 2A and anhydrite shell. Exact permeability structure for each simulation is given in Table 2.1. 10

2.6 a. Contour plot of temperature for homogenous permeability model. Negative depth indicates meters below sea floor. b. Average of maximum surface temperature for homogenous permeability model. c. Average minimum surface salinity v/s time plot for homogenous permeability model. Seawater indicates seawater salinity of 3.2 wt %. 13

2.7 a. Contour plot of highlighted box (top) shown on Figure 6a showing salinities of the liquid phase in the hydrothermal plume. b. Contour plot of highlighted box (bottom) on Figure 6a showing salinities of vapor phase in the phase separation zone. c. Contour plot of highlighted box (bottom) on Figure 6a showing salinities of brine phase in the phase separation zone. All salinity values are in wt %. 14

2.8 a. Contour plot of temperature for heterogeneous permeability model with Layer 2A. Negative depth indicates meters below sea floor. b. Average of maximum surface temperature for heterogeneous permeability models 1, 2, 3 and 4 compared with the 'basic model'. For legend, please refer to Table 2.1 c. Average of minimum surface salinity for heterogeneous permeability models 1, 2, 3 and 4. 'Seawater' indicates seawater salinity of 3.2 wt %. 15

2.9 a. Contour plot of temperature for heterogeneous permeability model with Layer 2A and anhydrite shell. Negative depth indicates meters below sea floor. White contours represent diffuse flow. b. Average of maximum surface temperature for heterogeneous permeability models 5 and 6 compared with the 'basic model'. For legend, please refer to Table 2.1 c. Average of minimum surface salinity for heterogeneous permeability models 5 and 6. 'Seawater' indicates seawater salinity of 3.2 wt %. 16

3.1 Thermal response of the Bio9 vent at East Pacific Rise $9^0 50'$ N [from Sohn et al., 1998], Nature, 396, 159161, 1998. 28

3.2 Temperature data from the three Endeavour axial valley sites. Red traces, data from thermistors located within hydrothermal fluids from vents; blue traces, data from thermistors deployed in the adjacent (non-vent) bottom water at each site. (a). Data from the bio-column thermistors at the Beach site, located in a diffuse vent within a sediment pond 200m south of the MEF. The earthquake activity (815 June 1999) is marked by the vertical shaded bar. Note that the temperature scale for this site is different from the other three sites shown. (b). Temperatures from the EI/MEF site, showing the slow temperature rise after the 8 June event. (c). Data from one of the Clam Bed thermistor pairs, near the High Rise vent field. (d). Temperature data from the Clam Bed site, located only a few tens of meters from those in c. . 29

3.3 Cartoon of the single-pass model showing key features. For meaning of legends please see Table 2.1. 34

3.4 Temperature distribution for East Pacific Rise in steady state (a) for the whole system for (b) for the boundary layer (c) near the surface. 35

3.5 Temperature distribution for Main Endeavour Field in steady state (a) for the whole system for (b) for the boundary layer (c) near the surface. 35

3.6 Temperature distribution for Main Endeavour Field in steady state (blue) and perturbed state for dike w = 1, 2, 10 and 20 m (a) for the whole system for (b) for the boundary layer (c) near the surface. Values were plotted $\sim$ 25 days after dike emplacement. 37

3.7 Temperature at the surface (top) and mass flow rate (bottom) for Main Endeavour Field in steady state (blue) and perturbed state (other colors) for dike w = 1, 2, 10 and 20 m, $\sim$ 25 days after diking event. 37

3.8 Temperature distribution for Main Endeavour Field in steady state (blue) and perturbed state for dike h = 250, 500, 750 and 1000 m (a) for the whole system for (b) for the boundary layer (c) near the surface. Values were plotted $\sim$ 25 days after dike emplacement. 39

3.9 Temperature at the surface (top) and mass flow rate (bottom) for Main Endeavour Field in steady state (blue) and perturbed state (other colors) for dike h = 250, 500, 750 and 1000 m, $\sim$ 25 days after diking event. 39

3.10 Temperature distribution for EPR $9^0$50' N in steady state (blue) and perturbed state when k in the diking zone is increased by 10%, 20%, 50% and 2 times (a) for the whole system for (b) for the boundary layer (c) near the surface. Values were plotted $\sim$ 25 days after dike emplacement. 40

3.11 Temperature at the surface (top) and mass flow rate (bottom) for EPR $9^0$50' N in steady state (blue) and perturbed state (other colors) when k in the diking zone is increased by 10%, 20%, 50% and 2 times, $\sim$ 25 days after diking event. 40

3.12 Temperature distribution for Main Endeavour Field in steady state (blue) and perturbed state when k in the diking zone is increased by 10%, 20%, 50% and 2 times (a) for the whole system for (b) for the boundary layer (c) near the surface. Values were plotted $\sim$ 25 days after dike emplacement. Dike w = 2 m, and h = 500 m. 42

3.13 Temperature at the surface (top) and mass flow rate (bottom) for Main Endeavour Field in steady state (blue) and perturbed state (other colors) when k in the diking zone is increased by 10%, 20%, 50% and 2 times, 25 days after diking event. 42

3.14 Temperature distribution for EPR $9^0$50' N in steady state (blue) and perturbed state for no diking scenario when k in the diking zone is increased by 10%, 20%, 50% and 2 times (a) for the whole system for (b) for the boundary layer (c) near the surface. Values were plotted $\sim$ 25 days after the event. . . 43

3.15 Temperature at the surface (top) and mass flow rate (bottom) for EPR $9^0$50' N in steady state (blue) and perturbed state (other colors) for no diking scenario when k in the diking zone is increased by 10%, 20%, 50% and 2 times, $\sim$ 25 days after the event. 43

3.16 Temperature distribution for Main Endeavour Field in steady state (blue) and perturbed state for no diking scenario when k in the diking zone is increased by 10%, 20%, 50% and 2 times (a) for the whole system for (b) for the boundary layer (c) near the surface. Values were plotted $\sim$ 25 days after the event. . . 44

3.17 Temperature at the surface (top) and mass flow rate (bottom) for Main Endeavour Field in steady state (blue) and perturbed state (other colors) for no diking scenario when k in the diking zone is increased by 10%, 20%, 50% and 2 times, $\sim$ 25 days after the event. 45

4.1 Simulation results depicting hydrothermal plume from (a) 2-D model [Singh et al., 2013] and (b) 3-D model of hydrothermal system at mid-ocean ridges [from Coumou et al., 2008, Reprinted with permission from AAAS]. 55

4.2 Schematic flowchart of algorithm adopted in the paper. The dashed box represents the iterative part of PIC model. 59

4.3 Schematic representation of the geometrical setup of the models for (a) across-axis model with homogenous permeability, (b) across-axis model with heterogeneous permeability (c) along-axis model 60

4.4 Plot of temperature contours for simulation results from FISHES showing the hydrothermal plumes structure for (a) homogeneous permeability across-axis model (b) along axis model. (c) Temperature contours of simulation results where dashed lines mark the zones as discussed in the paper (i) discharge zone (ii) near recharge zone (iii) far recharge zone (iv) top recharge zone. 62

4.5 Simulation results of the PIC model for across axis model with homogeneous permeability and uniform distribution of particles in the entire domain for different snapshots in time. 63

4.6 Simulation results of the PIC model for across axis model with homogeneous permeability and top recharge zone for different snapshots in time. 64

4.7 Simulation results of the PIC model for across axis model with homogeneous permeability and near recharge zone for different snapshots in time. 65

4.8 Simulation results of the PIC model for along axis model with homogeneous permeability and near recharge zone for different snapshots in time. 66

4.9 Contour plot of the across axis model showing approximate paths for discharge (red dashed line) and residence (blue dashed line) times for the fluid. 67

4.10 Determination of discharge time for across axis model for one particle. The blue dots represent the trajectory taken by the particle. 69

4.11 Determination of residence time for across axis model for one particle. The blue dots represent the trajectory taken by the particle. 70

4.12 Determination of residence time for across axis model with layer 2A for one particle. The blue dots represent the trajectory taken by the particle. 71

A.1 Temperature distribution for the generic model in steady state (blue) and perturbed state for no diking scenario when k in the diking zone is increased by 50% (a) for the whole system for (b) for the boundary layer (c) near the surface. Values were plotted 25 days after the event. 80

A.2 Temperature at the surface (top) and mass flow rate (bottom) for the generic model in steady state (blue) and perturbed state (other colors) for no diking scenario when k in the diking zone is increased by 50%, 25 days after the event. 81

List of Tables

2.1 Model specifications for generalized model shown in Figure 2.5b. Names of each simulation have been used as legend in Temperature and Salinity v/s Time plots. 21

3.1 Table of Symbols 50

3.2 Table of Symbols 51

Chapter 1

Introduction

Hydrothermal systems essentially consist of a heat source and a fluid circulation system. For high-temperature hydrothermal systems at oceanic spreading centers, the heat comes primarily from the emplacement of magma bodies in the shallow crust. The circulating fluid is mainly seawater, with some input of magmatic volatiles. In the simplest scenario, seawater enters the crust through faults and fractures and descends along permeable pathways to near the top of the magma body where it reaches temperatures exceeding 400^0C. The heated fluid then ascends through other permeable faults or fracture zones and emerges at the seafloor as mineral-rich "black smoker" vents. The temperature and composition of fluids collected at these vents vary greatly depending upon the geological and thermal constraints of the system.

As mid-ocean ridges are sites of creation of new oceanic crust, the hydrothermal systems associated with them represent one of the most fundamental Earth systems. Our understanding of these systems, however, is fairly limited. This dissertation is an attempt to address a few questions regarding these systems and is divided into three manuscripts.

The first manuscript titled "Numerical Modeling of Phase Separation at Main Endeavour Field, Juan de Fuca Ridge" was published in the journal Geochemistry, Geophysics, Geosystems in 2013 with co-authors Dr. R.P. Lowell (Virginia Tech) and Dr. K.C. Lewis (Monmouth Univeristy). Before being disrupted by a magmatic event in 1999, the vent temperatures and salinities along the axis of the Main Endeavour Field on the Juan de Fuca Ridge exhibited a quasi-steady spatial gradient in which the southern vent fluids were hotter and less saline than the northern vent fluids. This manuscript presents 2-D numerical models of two phase flow in a NaCl-H2O system to understand these gradients. I present homogenous permeability models with a range of bottom boundary temperature distributions and heterogeneous permeability models by imposing layer 2A extrusives with a constant bottom boundary temperature distribution. The aim is to understand the impact of both bottom boundary temperature and layer 2A permeability on hydrothermal fluids and to determine what combination of these controlling factors could cause the observed trend.

The second manuscript titled "The Thermal Response of Mid-Ocean Ridge Hydrothermal Systems to Perturbations" was accepted for publication in the journal Deep Sea Research vol. II in 2015 with Dr. R.P. Lowell (Virginia Tech) as coauthor. This work aims to understand the rapid thermal response of hydrothermal systems to magmatic and seismic disturbances.

The third manuscript is titled "A Particle in Cell Algorithm for Tracing Path-lines in Hydrothermal Systems" is prepared for submission with Dr. R.P. Lowell (Virginia Tech) as coauthor. In this paper I introduce a method of calculating particle trajectories for subsurface flows and for the estimation of fluid residence times.

Chapter 2

Numerical Modeling of Phase Separation at Main Endeavour Field, Juan de Fuca Ridge

Published in Geochemistry, Geophysics, Geosystems in 2013, with co-authors Dr. R.P. Lowell (Virginia Tech) and Dr. K.C. Lewis (Monmouth Univeristy)

Abstract

Before being disrupted by a magmatic event in 1999, the vent temperatures and salinities along the axis of the Main Endeavour Field on the Juan de Fuca Ridge exhibited a quasi-steady spatial gradient in which the southern vent fluids were hotter and less saline than the northern vent fluids. We present 2-D numerical models of two phase flow in a NaCl-H2O system to understand these gradients. We consider homogenous permeability models with a range of bottom boundary temperature distributions and heterogeneous permeability models by imposing layer 2A extrusives with a constant bottom boundary temperature distribution. The aim is to understand the impact of both bottom boundary temperature and layer 2A permeability on hydrothermal fluids and to determine what combination of these controlling factors could cause the observed trend. We find that variations in bottom boundary temperature alone cannot explain the span of surface temperatures and salinities measured at the Main Endeavour Field. Heterogeneous permeability within layer 2A that has higher overall permeability in the northern part of the vent field than the southern part can reproduce the observed north to south temperature gradient, but such a permeability distribution cannot reproduce the observed salinity gradient. We conclude that both deep-seated heterogeneous permeability, perhaps localized by a fault zone, and a heterogeneous layer 2A are required to produce the trend of temperatures and salinities in vent fluids at the Main Endeavour Field prior to the 1999 event.

2.1 Introduction

In this chapter, we have used numerical code FISHES to construct models of phase separation within the Main Endeavour Field (MEF) on the Juan de Fuca Ridge (JDFR). In particular, we attempt to explain the observed quasi-steady north to south gradients in salinity and temperature of the hydrothermal vent fluids [Butterfield et al., 1994] that existed between 1984 and the non-eruptive magmatic event in 1999 [Johnson, 2000; Lilley et al., 2003; Figure 2.1].

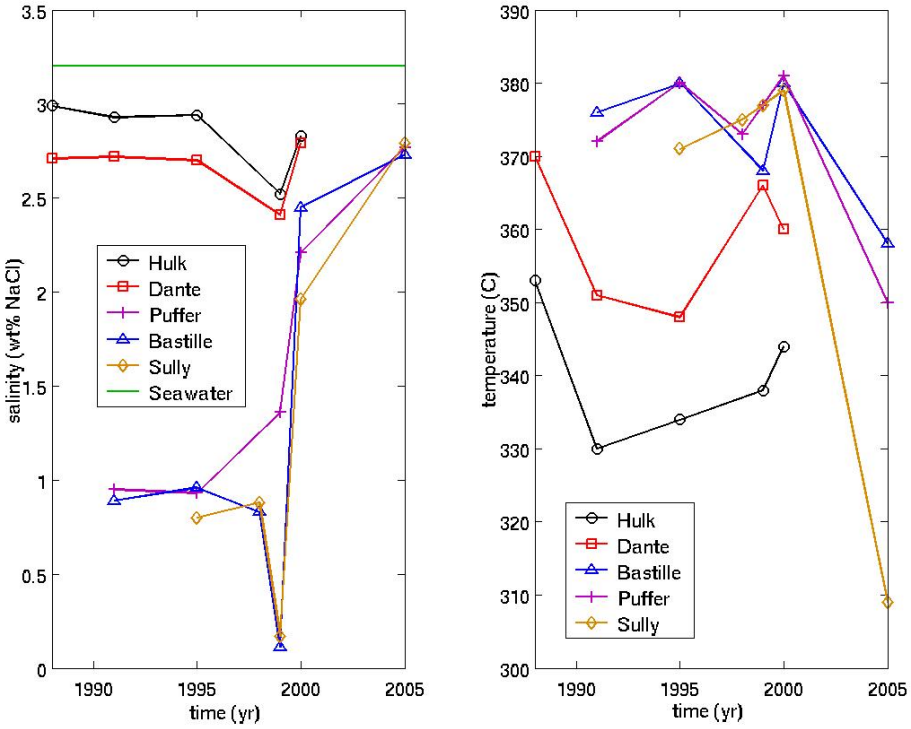

Figure 2.1: Vent fluid salinity (wt% NaCl) and temperature (^{0}C) data from the MEF. Data from 1988 are from Butterfield et al. [1994]; data from 1990 to 2000 are from Lilley et al. [2003]; and 2005 data are from Foustoukos et al. [2009].

Our models, while not addressing all aspects of the hydrothermal circulation system, provide significant insight into the effects of bottom boundary temperature and crustal permeability structure on temperature and salinity of the vent fluid as well as on fluid mixing between deep seated, high-temperature circulation and low temperature circulation in Layer 2A. In the next section, we describe the study area and the principal field data used to constrain the models. Then we present the numerical modeling code FISHES, the model setup and results, and finally, the implications of the model results. We end by offering some

concluding remarks.

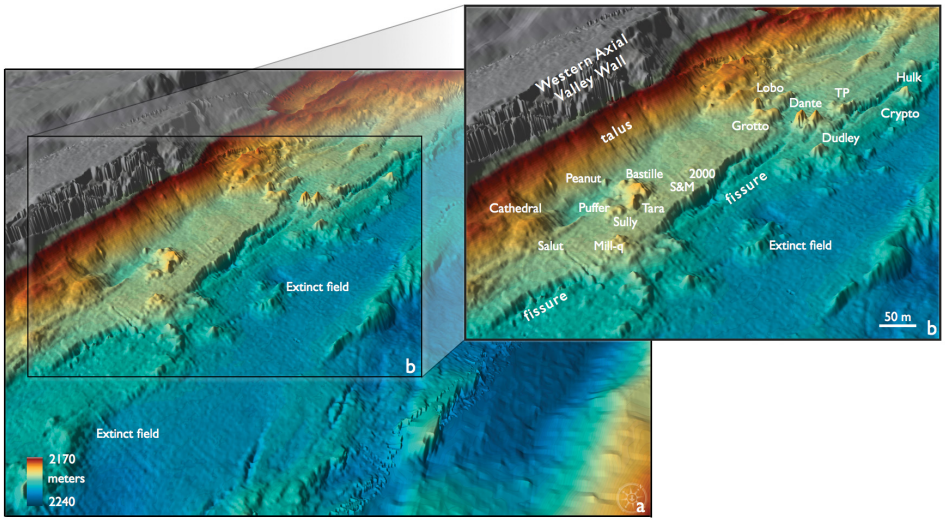

Figure 2.2: Figure High-resolution (∼5 m) bathymetry map of the Endeavour Integrated Study Site "bulls-eye" the Main Endeavour Field. The bathymetry was collected in 2005 as part of a joint project between the University of Washington, the W.M. Keck Foundation, and NEPTUNE Canada using the autonomous vehicle ABE. http://media.marine-geo.org/image/main-endeavour-field-2012.

2.2 Main Endeavour Field

The MEF located at $57^0$47'N on the JDFR is one of five high-temperature hydrothermal fields on the Endeavour Segment. Each of these vent fields is several hundred meters in length and separated by a few kilometers; they are characterized by a number of large sulfide edifices and areas of low-temperature diffuse flow [Kelley et al., 2002]. The MEF has had a history of study that spans nearly two decades [Kelley et al., 2012 and references therein]. Before it got significantly perturbed by 1999-2000 magmatic events [Johnson et al., 2000; Davis et al., 2001; Lilley et al., 2003], the MEF had been relatively stable since its discovery in 1982 [Delaney et al., 1992; Kelley et al., 2002]. The consistency of high temperature, low salinity fluids at MEF and prolonged scientific interest in the area make it a type-setting for mid-ocean ridge hydrothermal studies.

In order to develop a numerical model of two-phase flow and phase separation at MEF, we incorporate a number of observational constraints. These data include seafloor bathymetry data, seismic data revealing important features of the sub-axial magma chamber (AMC) and structure of the extrusive layer 2A [Van Ark et al., 2007], time series measurements of vent fluid temperature (T), salinity (X) and chemistry [Butterfield et al., 1994], measurements of hydrothermal heat output [Bemis et al., 1993; Ginster et al., 1994; Veirs et al., 2006; Johnson et al., 2010], and integrated thermal blanket heat flow data [Johnson et al., 2010].

2.2.1 Bathymetry and Structure

Figure 2.2 [Kelley et al., 2012] shows that the MEF, which is located near the western margin of the median valley, is situated at seafloor depths between approximately 2000 and 2200 m. The MEF, along with other hydrothermal systems on the Endeavour Segment, are localized by major faults [Wilcock and Delaney, 1996], the existence of which may be partially related to episodic dike emplacement [Carbotte et al., 2006].

Seismic data [Van Ark et al., 2007] indicate that layer 2A (identified as extrusive basalts) is variable in the neighborhood of the MEF with a mean thickness of 460 ± 160 m. The data also show a sub-axial magma chamber beneath the MEF at a depth ranging between 2 and 2.5 km with a width of 0.8 km, dipping to the east (Figure 2.3). As discussed below, Johnson et al. [2010] suggest that this dip controls hydrothermal flow paths and gives rise to an east-west gradient in conductive heat flow.

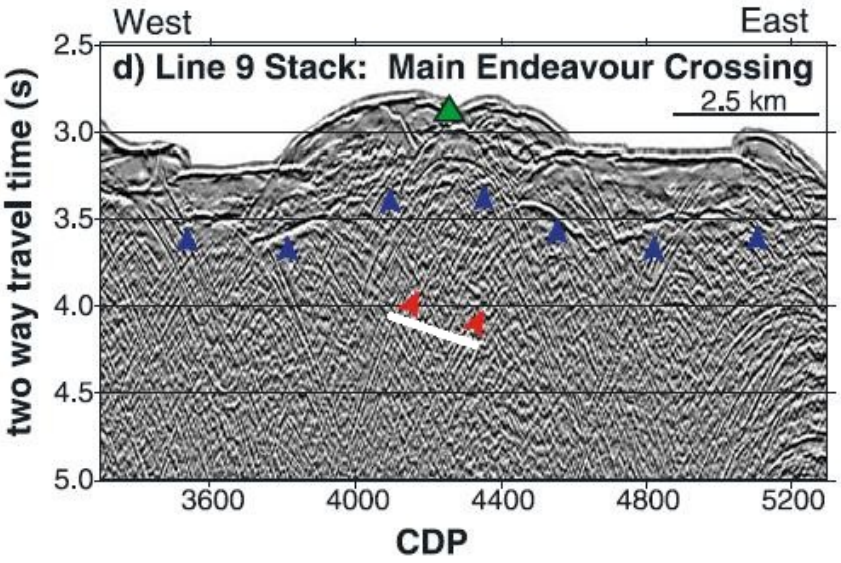

Figure 2.3: Stack of cross-axis line 7 from Van Ark et al. [2007]. Triangles show location of the hydrothermal vent fields. Blue arrows indicate the seismic layer 2A event, and red arrows indicate the AMC reflection.

2.2.2 Thermal data

Data collected in 1984, 1987 and 1988 from the MEF [Butterfield et al., 1994] shows a significant gradient in salinity of the vent fluid, with the lowest salinity fluids in the southwest approximately half of that of the fluids in the northeast (Figure 2.1). Although there is more variability as a function of time, the temperatures of the vent fluids show a complementary trend, in which vent fluid temperatures were highest in the southwest and lowest in the northeast (Figure 2.1). The low salinity of the vent fluid across the MEF indicates the

occurrence of phase separation and loss of brine phase below the seafloor [Butterfield et al., 1994]. This characteristic fluid salinity varied very little from year to year but changed dramatically after a diking event in 1999 [Lilley et al., 2003]. Following this event, the vent temperatures in the southern part of the field ($\sim 380^0$C prior to the event) have declined and salinity of fluids (< 2.5 wt% seawater) has risen back toward seawater values (Figure 2.1).

Heat flux at the MEF was first measured by Bemis et al. [1993] and Ginster et al. [1994]. According to their estimates, heat output from focused venting on MEF was $\sim$ 200 MW - 350 MW. Viers et al. [2006] conducted a hydrographic study on the MEF to show that the total heat output from the field is partitioned nearly equally between focused and diffused flow and estimated the total heat output to be $\sim$ 500 MW. Using a mean heat output of 450 MW derived from a number of studies [Baker, 2007], a mean vent temperature of 365^0C, and a vent field area of 106 m^2, Lowell et al. [2013], estimate the permeability of the discharge zone to be 2 x$10^{-13}m^2$. Consequently, we have used a value of $10^{-13}m^2$ in our homogenous permeability models.

Johnson et al. [2010] use thermal blankets to measure conductive heat flow on the Endeavour Segment. They interpret the low heat flow sites on the valley boundary wall directly east of the MEF to indicate a pervasive east-west two-dimensional cross-valley flow, with seawater recharge on the eastern valley wall and fluid discharge near the western wall of the axial valley (Figure 2.4).

Although hydrothermal circulation is likely to be three-dimensional, we use the thermal blanket data as a first-order justification to consider a 2-D across-axis model for the MEF hydrothermal system. As described in section 4, we assign the western bottom boundary of the model a temperature so that the basal region is in the two-phase liquid-vapor region of P-T-X space. We then assume the temperature declines sharply along the dip of the AMC and then assign a shallower gradient for the remaining width of the model. To explain the differences in vent salinity and temperature across the MEF, we consider several of 2-D across-axis simulations in which the bottom boundary temperatures and/or crustal permeability structures are different.

2.3 Numerical Modeling Code FISHES

Fully Implicit Seafloor Hydrothermal Event Simulator or FISHES is a numerical scheme capable of simulating two-phase flow in a permeable medium containing a NaCl-H2O fluid [Lewis and Lowell, 2009a, 2009b]. It provides solutions to the equations governing fluid flow together with an equation of state that calculates thermodynamic properties of the fluid as functions of temperature, pressure and salinity at each time step. These equations stem from Faust and Mercer [1979] with the addition of an equation for conservation of salt. Conservation of mass is given by

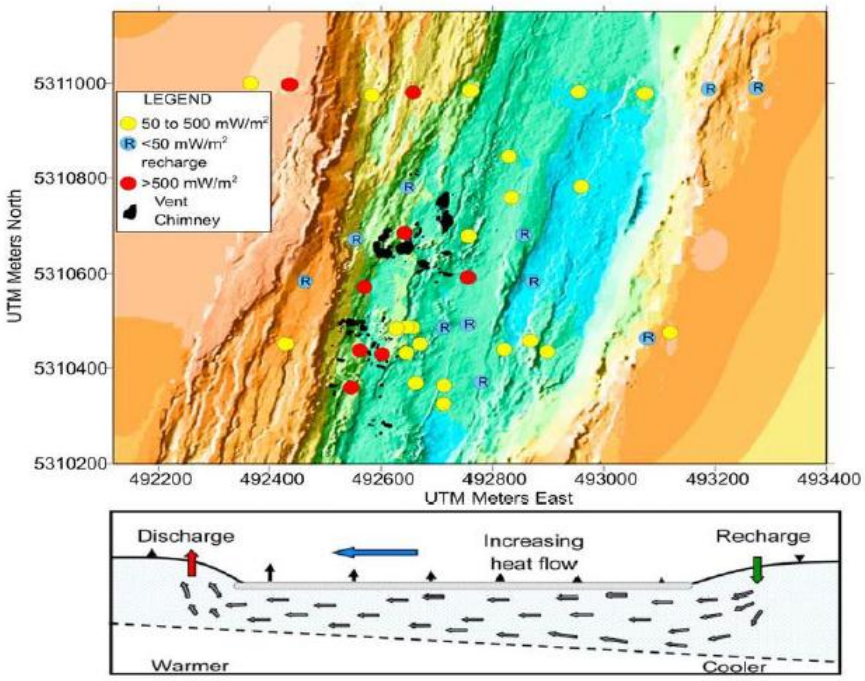

Figure 2.4: (Top) Heat flow data from Johnson et al. [2010] are coordinated with the thermal blanket station positions. The easternmost station lies in the topographic low east of the axial valley. Colored circles correspond to recharge (blue), conductive (yellow),and discharge (red). (Bottom) Interpretive cartoon of North Line data from Johnson et al. [2010], with recharge occurring on the valley eastern boundary fault and lateral subsurface transport beneath the valley to discharge on the valley western boundary fault. Sloping dashed line represents the shallower magma chamber beneath the western side of the axial valley. Cartoon dimensions not to scale.

$$\frac{\partial(\phi\rho)}{\partial t} + \nabla \cdot (\rho_v \vec{v_v} + \rho_l \vec{v_l}) = 0 \tag{2.1}$$

where ϕ is the porosity, ρ is the bulk density, v is the Darcian velocity and the subscripts v and l refer to the vapor phases and the liquid phases, respectively. Conservation of momentum is assumed to be governed by Darcy's Law for each fluid phase, which states

$$\vec{v_v} = -\frac{kk_{rv}}{\mu}(\nabla P - \rho_v g \nabla z) \tag{2.2}$$

$$\vec{v_l} = -\frac{kk_{rl}}{\mu}(\nabla P - \rho_l g \nabla z) \tag{2.3}$$

Where k is the permeability, P is the pressure, z is the depth, m is the dynamic viscosity,

and g is the gravitational acceleration. The relative permeability k_r is assumed to be linearly proportional to the respective volume saturation of each phase, and the residual saturation is assumed to be zero.The energy conservation equation is

$$\frac{\partial \left[\phi\rho h + (1-\phi)\rho_r c_r T\right]}{\partial t} + \nabla \cdot (\rho_v h_v \vec{v_v} + \rho_l h_l \vec{v_l}) = \nabla \cdot (\lambda_m \nabla T) \tag{2.4}$$

where h is the specific enthalpy, T is the temperature, m is the effective medium thermal conductivity, and the subscript r refers to the rock; and h without subscript refer to bulk quantities. The equation describing the conservation of salt from Bai et al. [2003] is given by

$$\frac{\partial(\phi\rho X)}{\partial t} + \nabla \cdot (\rho_v \vec{v_v} X_v + \rho_l \vec{v_l} X_l) = \nabla \cdot (\phi\rho_v D \nabla X_v + \phi\rho_l D \nabla X_l) \tag{2.5}$$

The solutions to equations (1) through (5) are obtained using Patankar's [1980] scheme for a finite control volume with upstream weighting, implying that each of the internal nodes are considered as the centroid of a control volume through which the fluid flows. The densities, salinities, and enthalpies as functions of P-T-X are evaluated via linear interpolation between values in thermodynamic lookup tables. These tables are valid for pressures between 85 and 1000 bars, temperatures between 0 and 800C, and salinities between 0 and 100 wt% NaCl.

The bulk density from 300 to 800^0C and the salinity and density on the upper boundary of the two-phase region are based on the work of Anderko and Pitzer [1993], and the bulk density from 0 to 300C is based upon the work of Archer [1992]. The specific enthalpy is compiled using the framework of Tanger and Pitzer [1989] and Archer [1992]. The salinity on the halite-saturated vapor surface is obtained using the correlation equation from Palliser and Mckibbin [1998]. Lewis and Lowell [2009a] provide additional details on the FISHES code. FISHES and the users guide may be downloaded using the link: http://www.geophys.geos.vt.edu/rlowell/kaylal/ from the "downloads" section.

2.4 Model setup

The across-axis models (Figure 2.5) are assigned a depth of 2 km and a width of 1.5 km. Side walls of the system are impermeable and insulated. The top boundary of the system is permeable and maintained at constant seafloor pressure of 220 bars. For fluid leaving the surface of the model, the numerical scheme is upwinded for temperature and salinity, which means that the value at the surface is calculated based on the value of the parameter one node below. The bottom boundary of the system is impermeable and maintained at a constant temperature. The western (left) bottom boundary is made hotter than the eastern (right) bottom boundary to simulate the effect of the dip in the magma chamber.

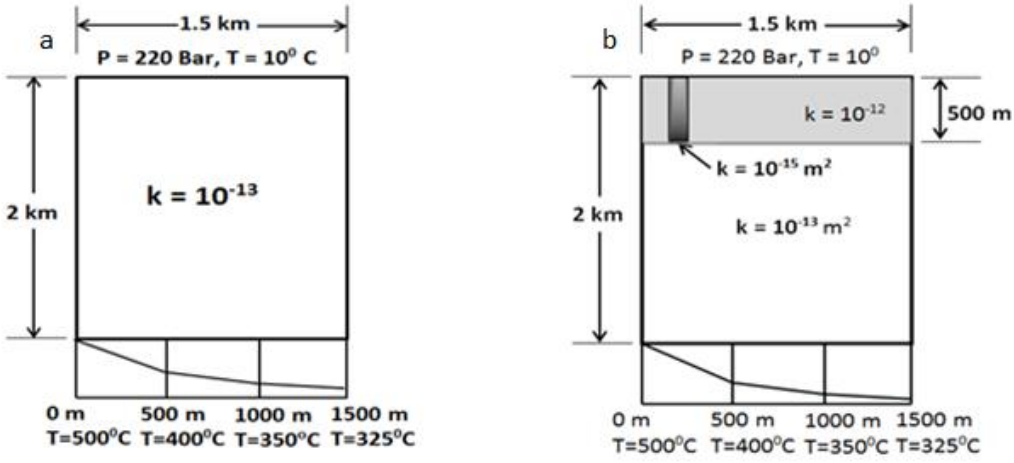

Figure 2.5: Schematic representation of across-axis model with boundary conditions and bottom boundary temperature profile. (a) Homogenous permeability model, (b) general representation of heterogeneous permeability model with layer 2A and anhydrite shell. Exact permeability structure for each simulation is given in Table 2.1.

In the 'basic' model, the highest bottom boundary temperature (BBT) is 500^0C (Figure 2.5a). Simulations are also run for highest BBT of 475^0C, 450^0C and 400^0C. We consider a maximum BBT of 500^0C to be a reasonable assumption based on Fontaine et al. [2009]. They have used geothermobarometry to infer that, for several mid ocean ridge hydrothermal systems, the temperature on the top of the 'reaction zone' or zone where chloride and silicate equilibrate lies between 415^0-445^0C. Additionally, Jupp and Schultz [2004] argue that that water in hydrothermal convection cells upwells at $\sim 400^0$C when driven by a heat source above $\sim 500^0$C.

In each case, the temperatures are decreased from the western to eastern edge with similar temperature gradients. Temperature at the seafloor is set to 10^0C and initially increases linearly from top to bottom of the system. The initial pressure distribution is hydrostatic and salinity is set to 3.2 wt% everywhere. Three permeability models were used: homogenous, heterogeneous with layer 2A, and heterogeneous with layer 2A and an anhydrite shell. Each is described below.

The cell size in our models is (25x25) m. Although this spacing is too coarse to model individual vent chimneys, this cell size corresponds roughly to the spatial scale of the large sulfide structures at the MEF. Vent fluids from these structures tend to have relatively uniform temperature [Butterfield et al., 1994]. Because we are not trying to model individual vents, but only the general N-S gradients, we believe that this resolution is sufficient.

2.4.1 Homogenous permeability model

Han et al. [2013] show that permeability plays an important role in plume structure and heat output of hydrothermal systems, but that it has relatively little effect on vent fluid temperature and salinity, given the same bottom temperature distribution. Therefore, the purpose of the homogeneous permeability model was to understand the effect of different maximum BBTs (500^0C, 475^0C, 450^0C and 400^0C) while keeping other model parameters the same. The goal was to determine whether changes in bottom boundary temperature could explain the observed gradients in vent temperature and salinity in the MEF.

Although the Rayleigh number does not fully describe convection in a phase separating system, it is still a useful parameter for approximating the vigor of convection. Here we use the classical expression

$$R_a = \frac{\alpha \rho_l g k \Delta T H}{\mu \kappa} \tag{2.6}$$

where α, μ, and ρ_l represent the thermal expansion coefficient, dynamic viscosity and density of the fluid, respectively; g is the gravitational acceleration, H is the vertical thickness of the system, k is the permeability, ΔT is the temperature difference between the top and the bottom boundaries, and is the effective thermal diffusivity. Assuming approximate high-temperature values of $\alpha = 10^{-3}$ ^{0}C^{-1}, $\mu = 10^{-4}$ Pa-s, $\rho_l = 10^3$ kg/m^3, $g = 9.8$ m/s^2, $\Delta T = 400^0$C, $\kappa = 8$ x 10^{-7} m^2/s, H = 2 x 10^3 m, and k = 10^{-13} m^2, we find Ra $\approx$ 10000 for these simulations. This value greatly exceeds the critical Rayleigh number R_{ac} =27.1 for a fluid-saturated open-top porous medium [Nield, 1968]; consequently, we expect temporal and spatial variations in temperature and salinity of vent fluids. However, by specifying the basal temperature, P-T conditions for phase separation at the base of the system for a given temperature and permeability remain essentially constant [Han et al., 2013]. This enables us to potentially determine the effect of changing BBT for our homogenous permeability model and also understand how permeability affects seafloor temperature and salinity for the same temperature boundary condition at depth.

2.4.2 Heterogeneous permeability model

The permeability structure of the crust may be important because it controls the extent of seawater mixing with rising hydrothermal fluid and thus affects both the temperature and salinity of venting fluid. Lowell et al. [2007] show that the hydrothermal discharge temperature decreases as the permeability in the extrusive layer 2A increases relative to that in the deep discharge zone. They also show that the presence of a low-permeability barrier, perhaps resulting from anhydrite precipitation, lessens the impact of the higher permeability in layer 2A. Fontaine et al. [2007] explore a similar idea using single-phase, two-dimensional numerical models of hydrothermal circulation to investigate the physical

controls on maximum venting salinities. They argue that the venting salinity is dependent on the permeability structure and that the simplest models with uniform or layered permeability are unable to account for both the maximum observed salinity and temperature. When they use a more complex model in which the upflow is surrounded by a low-permeability shell, they infer that such models are more consistent with the observational data. Their models fit the observations best when the permeabilities of the upper layer differ from the permeability of the lower layer by factors of 10 and 100 in upflow and downflow regions, respectively, and when the permeability of the shell is one tenth that of the lower layer.

Seismic data collected at the MEF [Van Ark et al., 2007] indicates that layer 2A is continuous for the region with a mean thickness of 460±160 m. To study the impact of layer 2A on surface fluid properties, we have assumed that it is 500 m thick and has higher permeability than the underlying sheeted dikes. Furthermore, to account for heterogeneities in layer 2A due to local mineral precipitation, we added a low permeability shell surrounding the upflow region to some models. The assumed values of permeability in layer 2A and in the anhydrite shell, for various combinations of magnitude and spatial location, are given in Table 2.1. Figure 2.5b shows a general schematic.

2.5 Results

2.5.1 Homogeneous permeability model

Figure 2.6a shows the results of a 'basic' across-axis simulation with a maximum BBT of 500^0C after a simulation time of 60 years. For the specified geometry and P-T conditions of our model, phase separation occurs in a small region close to western end of the bottom boundary (Figure 2.7b and 2.7c). The rest of the system remains in a single phase regime (Figure 2.7a). We interpret the single plume to represent a MEF vent structure associated with a cross-axis convection cell. The surface temperature varies from $\sim 370^0$C at the center of the plume and drops of sharply to the seafloor temperature of 10^0C. Although the plume structure is stable, the maximum temperature of the fluid fluctuates by a few degrees on a time scale of years. The average salinity of the plume also varies with time and VDF and BDF fluids vent at different times, again with episodic fluctuation on the time scale of a year.

We ran the homogeneous model for BBTs 475^0C, 450^0C and 400^0C to investigate the effect of different BBTs on the vent fluid temperature and salinity. These simulations are referred to as T500, T475, T450 and T400, respectively. Figure 2.6b is a plot of average of maximum temperatures values (AMT) with their respective standard deviations for the different simulations. These values were calculated by averaging the maximum values of temperature in the plume for each year over the duration of the simulation. Similarly, average minimum salinity (AMS) values were obtained at the center of the plume (where the temperature is the greatest) for each of the homogenous permeability models (Figure 2.6c).

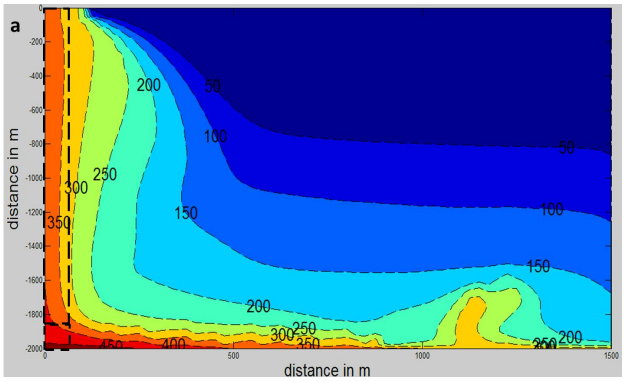

(a)

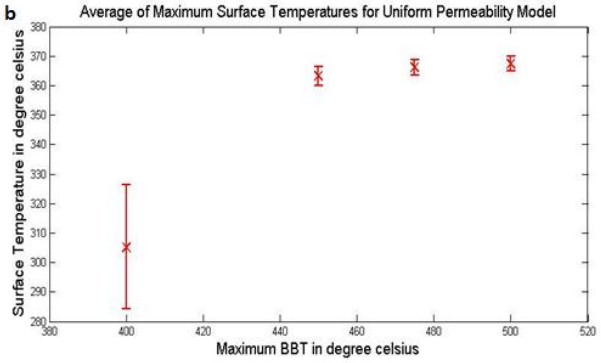

(b)

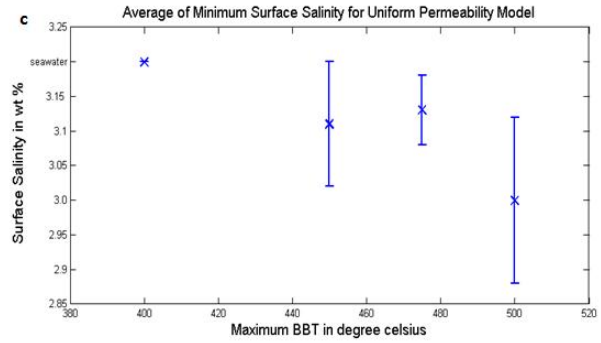

(c)

Figure 2.6: a. Contour plot of temperature for homogenous permeability model. Negative depth indicates meters below sea floor. b. Average of maximum surface temperature for homogenous permeability model. c. Average minimum surface salinity v/s time plot for homogenous permeability model. Seawater indicates seawater salinity of 3.2 wt %.

Figure 2.6b shows that there is not much difference in the AMTs of models T500, T475 and T450, whereas for T400, AMT is noticeably lower. The high AMTs for models T500,

T475 and T450 are close to what is observed for southern MEF vent structures such as Puffer and Sully. However, for the range of BBT temperatures between 450^0-500^0C, it is not possible to detect differences in surface temperature. Low AMT obtained for T400 $\sim$ 305 $\pm$ 20^0C is similar to the vent temperatures at northern vent structures such as Hulk, which recorded values $\sim 330^0$C before 1999. The simulation T400 is in the single phase regime, however, resulting in vent salinity fixed at seawater value of 3.2 wt %. Figure 2.6c shows that although there is some variation in the AMS values for all the models, the range of temporal variability suggests that AMS values are also essentially independent of BBT in the range 450^0C-500^0C.

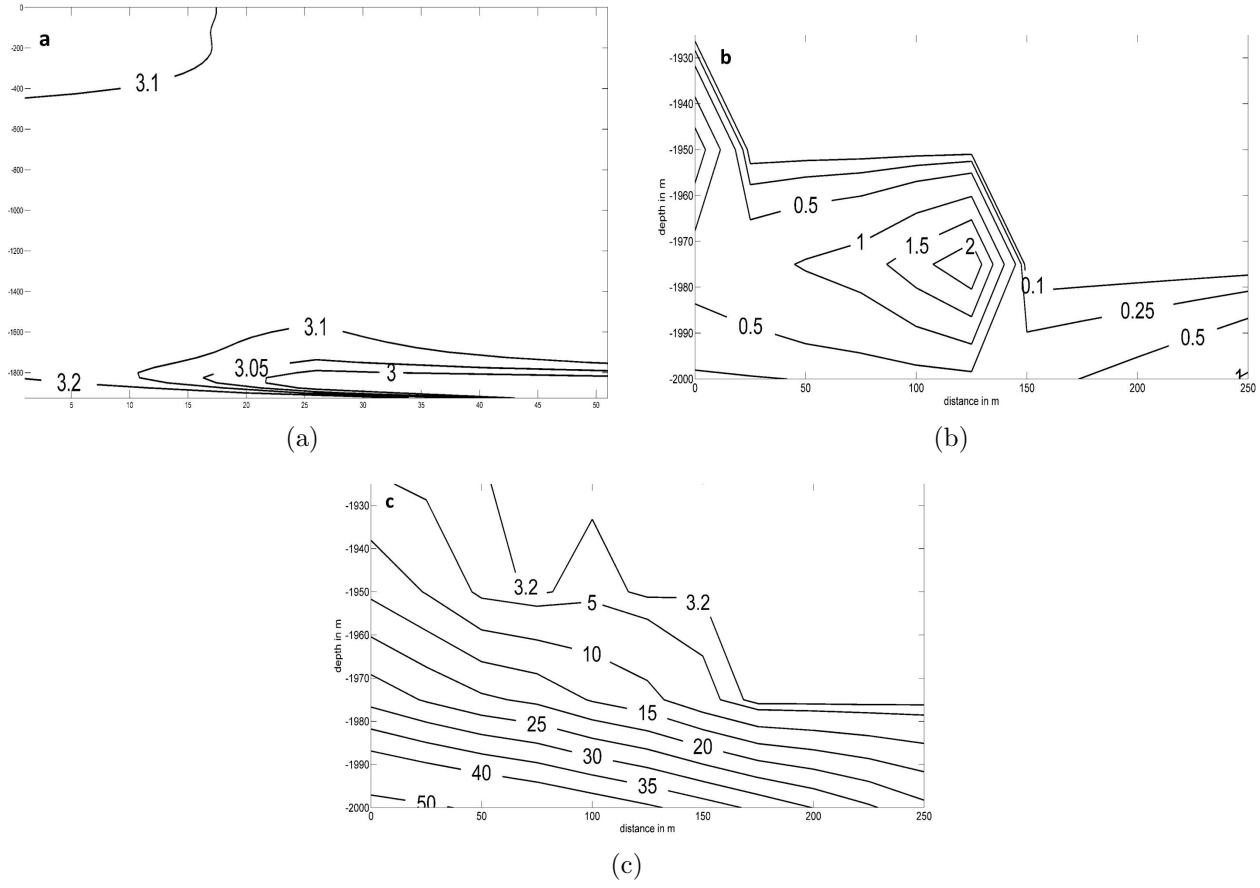

(a) (b)

(c)

Figure 2.7: a. Contour plot of highlighted box (top) shown on Figure 6a showing salinities of the liquid phase in the hydrothermal plume. b. Contour plot of highlighted box (bottom) on Figure 6a showing salinities of vapor phase in the phase separation zone. c. Contour plot of highlighted box (bottom) on Figure 6a showing salinities of brine phase in the phase separation zone. All salinity values are in wt %.

Although the AMT values correspond to values recorded at vent structures on the southern MEF, salinity values for the same simulations are higher than those observed. As mentioned before, the zone of phase separation in these models is confined to the bottom-most

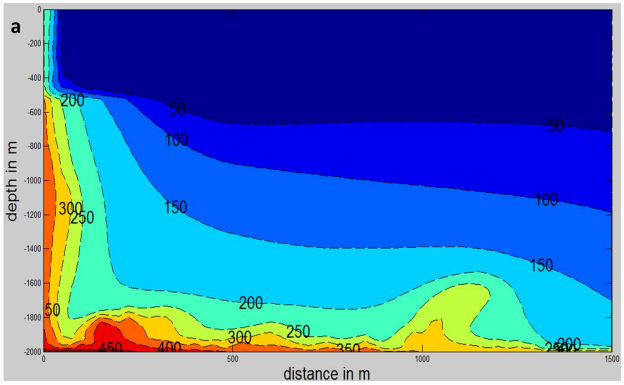

(a)

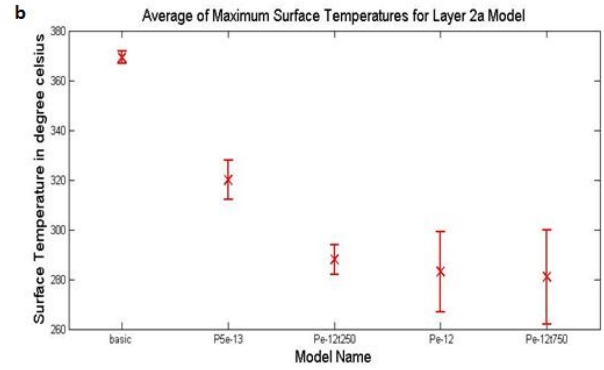

(b)

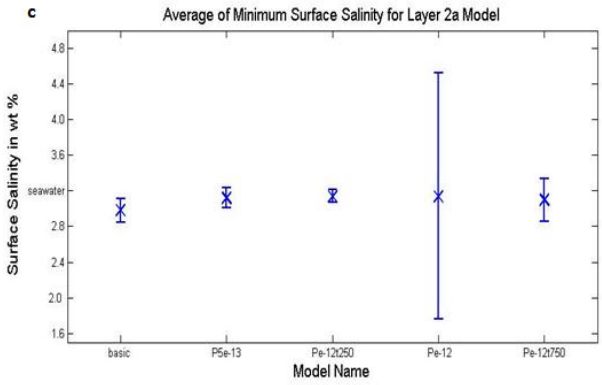

(c)

Figure 2.8: a. Contour plot of temperature for heterogeneous permeability model with Layer 2A. Negative depth indicates meters below sea floor. b. Average of maximum surface temperature for heterogeneous permeability models 1, 2, 3 and 4 compared with the 'basic model'. For legend, please refer to Table 2.1 c. Average of minimum surface salinity for heterogeneous permeability models 1, 2, 3 and 4. 'Seawater' indicates seawater salinity of 3.2 wt %.

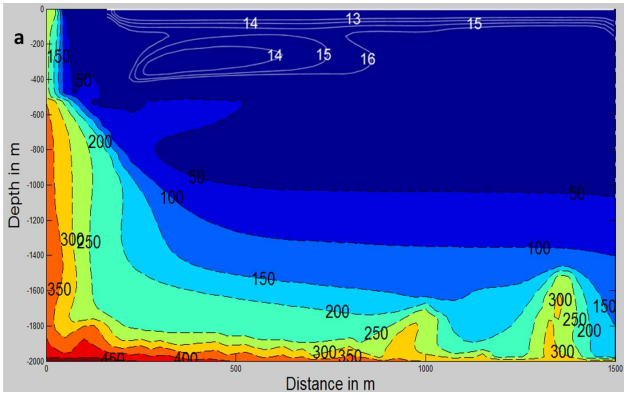

(a)

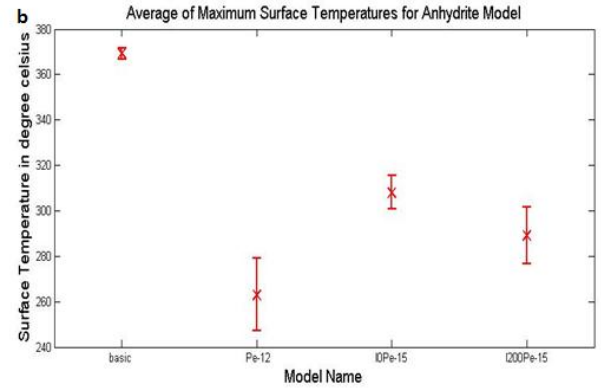

(b)

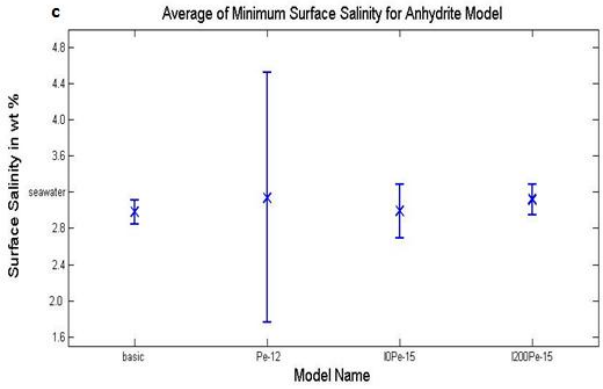

(c)

Figure 2.9: a. Contour plot of temperature for heterogeneous permeability model with Layer 2A and anhydrite shell. Negative depth indicates meters below sea floor. White contours represent diffuse flow. b. Average of maximum surface temperature for heterogeneous permeability models 5 and 6 compared with the 'basic model'. For legend, please refer to Table 2.1 c. Average of minimum surface salinity for heterogeneous permeability models 5 and 6. 'Seawater' indicates seawater salinity of 3.2 wt %.

region of the system. As the hot, vapor rich, low salinity fluid rises, it mixes with relatively hot, but single-phase fluid that is circulating deep in the system. As a result, although both the temperature and salinity of the upwelling fluid are changed as a result of mixing, vent salinity may be changed to a greater extent than the temperature. To investigate the effects of mixing, particularly in the shallow part of the system, we consider the effects of heterogeneous permeability by imposing a layer 2A on the model.

2.5.2 Heterogeneous Permeability Model with Layer 2A

For these simulations, BBT distribution is fixed as shown in Figure 2.5b and simulations were run for scenarios 1-6 in Table 2.1. The results of scenarios 1- 4 are shown in Figure 2.8 and scenarios 5 and 6 are shown in Figure 2.9. Introduction of layer 2A in our models increases overall permeability of the system thereby increasing the effective Rayleigh number. This leads to more vigorous convection and increased mixing of cold seawater into the plume before the fluids come to the surface (Figure 2.8) thereby decreasing the temperature and increasing the salinity. By introducing layer 2A, the vent fluid temperature which initially was similar to that at southern vent structures ($\sim 370^0$C) is now more similar to temperatures at northern vent structures ($\sim 320^0$C). AMS values are still below but quite close to seawater value, similar to what is observed at northern MEF vent (Hulk, Dante, Figure 2.1, Figure 2.7c). The thickness of layer 2A does not seem to cause major variations in surface temperature and salinity (Figure 2.8c). Compared to the homogenous models, lower temperature VDF are obtained on the surface while the system is undergoing phase separation at depth.

2.5.3 Heterogeneous permeability with anhydrite shell

We ran simulations 5 and 6 as shown in Table 2.1 with a region of low permeability ($10^{-}15$ m^2) in the extrusive layer near the main discharge zone. This zone represents the precipitation of anhydrite that might occur as a result of mixing between the deeply circulating sulfate-poor hydrothermal fluid and sulfate-rich seawater circulating through the extrusive layer 2A [e.g., Lowell et al., 2003, 2007]. High-resolution magnetic data from the Endeavour vent field [Tivey and Johnson, 2002] also supports the idea of a vertical chemical barrier surrounding high-temperature vent fields. As in Lowell et al. [2007], we simulate the precipitation of anhydrite by introducing the 'shell' directly without actually considering the process of precipitation. We assume the shell is 50 m thick, extending the entire depth of layer 2A, which for each case is 500 m. We assume the permeability of the low-k barrier has a constant value of $10^{-}15$ m^2.

Introduction of the low permeability shell partially prevents the rising high-temperature plume from mixing with seawater within layer 2A. As a results the plume temperature increases somewhat, but not to values as high as those obtained without layer 2A. The temperature of the discharging fluid then lies nearer to those observed in the central part of the MEF (Figure 2.1). Some part of the hot hydrothermal fluid travels around the low

permeability zone (Figure 9a), causing moderately warm temperature flow outside of the high temperature plume (10^0C - 20^0C). Such flow is analogous to diffuse flow common around vent fields. Such diffuse flow was not observed in previous simulations and seems to result from a more complex permeability structure where parts of the rising plume may find alternate paths and express themselves on the surface as a variety of mixtures with sea water. The diffuse-flow fluid is persistent in both cases with the anhydrite layer. When this layer is farther from the center of the plume the maximum temperature of the main plume on the surface is less than when the anhydrite shell is closer to the rising plume (Figure 9b, c). There is no significant difference in temperatures of diffuse fluids in either case.

As the anhydrite shell limits the mixing between seawater and hot hydrothermal fluids, AMS values in these models are lower than those obtained in models with layer 2A alone. These values correspond to the northern vents at the MEF (Figure 2.1).

2.6 Discussion

2.6.1 Role of bottom temperature

Han et al. [2013] use similar modeling techniques to investigate how permeability and maximum bottom temperature affect vent fluid temperature and salinity in sea-floor hydrothermal systems. While their simulations are for a different set of model parameters (depth = 1km, maximum BBT = 450^0C), they arrive at some general conclusions for high Rayleigh number convection models. Their results suggest that while hydrothermal heat output increases linearly with permeability, the BBT plays a more important role in determining surface temperature and salinity. This argument led to the reasonable assumption that for MEF, the gradients in surface temperature and salinity could be a reflection of a gradient in the bottom boundary temperatures. With the homogenous permeability models, our aim was to explore this possibility. However, surface temperatures and salinities obtained for our homogenous permeability models do not correlate as well to the BBTs in the system as those in Han et al. [2013].

This discrepancy between our results and those obtained by Han et al. [2013] may be due to the difference in the model parameters used for MEF and those used by Han et al. [2013]. We use a depth of 2 km as opposed to the 1 km depth used in their models. Han et al. [2011], shows a few simulations for models that are 2 km deep (BBT = 450^0C - 500^0C). In those models, the correlation between the BBT and surface temperature and salinity is not as strong as for systems with a depth of 1 km. This reiterates the importance of modeling individual vent fields rather than using generic models to explain vent-specific observations. The homogenous permeability models that were phase separating give rise to temperatures that were similar to the southernmost vent structures at the MEF, but could not explain the salinity of these structures nor the observed gradients in temperature and salinity. For MEF, one cannot use BBT alone to explain the observed gradients. This result calls for some other mechanism to control temperature and salinity of hydrothermal vent fluids.

2.6.2 Heterogeneous permeability

By assuming layer 2A has higher permeability than the sheeted dikes, we found that enhanced mixing and cooling of hydrothermal fluid before discharging at the surface can produce a significant difference in the surface temperature and salinity of the fluids. In particular, the results of the models with heterogeneous permeability suggest that higher permeability in layer 2A lowers the temperature of the venting fluid and brings the salinity closer to that of seawater due to greater mixing between seawater and hydrothermal fluids. By contrast low permeability barriers around the upflow zone can shield the rising fluid from mixing. For different thicknesses (250, 500 and 750 m), permeabilities (5 x 10-13 and 1012 m2) and configurations of layer 2A (e.g., with a low permeability shell resulting from anhydrite precipitation), focused and diffuse flow with a wide range of temperature and salinity values can be obtained. The lowest temperature values obtained for our model with a layer 2A (see results for P5e-13 and I0Pe-15) matches the temperature values at the northern vent fields. By using an appropriate combination of magnitude of the permeability in layer 2A together with the location and thicknesses of a locally lower permeability barrier such as might result from mineral precipitation, a variety of temperature and salinities can, in principle, be obtained for the vent fluids. Without evidence to support a certain distribution of permeability, we chose not to extend this discussion further.

A drawback of our modeling is that although the surface temperatures in our model corresponded, or could be made to correspond, with vent structures along the MEF, the surface salinity values were all higher than the observed values. At the deepest and hottest part of our model (initial temperature = 500^0C; initial pressure ≈375 Bar), the salinity of the vapor phase is 0.175 wt% NaCl [also see Bischoff and Pitzer, 1989]. Assuming that this value is close to the salinity of vapor formed deep in the system at MEF, and that surface fluids at MEF are a mixture of this vapor and seawater, the extent of mixing between the two fluids can be estimated by correlating the end member composition of vapor and seawater mixture with the surface salinity of vent fluids obtained at MEF from Butterfield et al. [1994]. Such a correlation indicates that the amount of vapor in the surface vent fluids varies from ∼7 wt % (surface salinity = 505 mmol/kg; at Hulk) to ∼56 wt % (surface salinity = 253 mmol/kg; at Peanut). Lower salinity values, especially at southern MEF, indicate that a greater percent of the venting fluid is vapor than that obtained in our simulations. This indicates minimal or little mixing of the rising hydrothermal fluid with seawater for the southern vents. Implications of low salinity fluids obtained at the MEF are discussed below.

2.6.3 Low surface salinity at the MEF

Johnson et al. [2010] suggest that high-temperature venting at MEF is controlled by high permeability local faults and that recharge and discharge occur along narrow cylinders that penetrate deep to the heat source. Given the complex nature of faulting at mid ocean ridges, the relative depths of recharge and discharge limbs may determine how much hot fluid mixes with seawater before venting. As seems with the southern MEF, venting occurs

with comparatively little mixing between the rising plume and sweater. This indicates that in addition to shallow heterogeneities in the oceanic crust, permeability barriers also exist deep in the system that inhibit mixing leading to low salinity values on the surface. Similar results are obtained by Crone et al. [2011] for 950 N on East Pacific Rise (EPR), where they argue that lateral variations in permeability could contribute to the pattern of seismicity at EPR, and influence the location of upflow and downflow zones of hydrothermal flow. Therefore, the range of surface temperature and salinity values at MEF are a likely result of both shallow heterogeneities in layer 2A and lateral permeability contrasts deep in the crust.

Heterogeneity in the oceanic crust may be present as a result of various factors such as magma supply, lava flow, faulting, mineral precipitation, diking etc. and may occur at all depths and scales. Rising fluids driven by buoyancy will find the least resistive path to the surface via higher permeability channels. This will determine the amount of mixing and cooling it undergoes before exiting on the seafloor. Overall, higher permeability will lead to more mixing and therefore more cooling of hydrothermal fluids and vice versa. Therefore, we find our study in agreement with previous studies [e.g., Fontaine et al., 2007, Driesner, 2010] that in order to accurately understand the temperature and salinity of vent fluids, and to accommodate the heat flow data from mid ocean hydrothermal systems, it is important to recognize the role played by permeability on the system output.

2.7 Conclusions

We have used a two-phase numerical modeling code and data from studies at the Main Endeavour Field to investigate the possible causes of the observed trend in vent temperature and salinity between 1984 and 1999. We ran several models to study different influences on hydrothermal fluid circulation in the region. We find that although bottom boundary temperature in a hydrothermal system influences the surface temperature of a hydrothermal plume in general, the latter is not directly proportional to the former. Hydrothermal fluids may mix locally while rising to the surface generating a variety of temperatures and salinities. Moreover, low surface salinity values at the Main Endeavour Field are likely a result of lateral permeability contrasts deep in the system which inhibits mixing of rising vapor rich fluids with seawater. Finally, we conclude that the trend of temperatures and salinities in vent fluids at the Main Endeavour Field results from a heterogeneous oceanic crust which has higher overall permeability in the northern part of the vent field than the southern part.

Table 2.1: Model specifications for generalized model shown in Figure 2.5b. Names of each simulation have been used as legend in Temperature and Salinity v/s Time plots.

S. No	Simulation Name	Permeability Of Layer 2A(m^2)	Thickness Of Layer 2A(m)	Anhydrite Layer k = $10^{-}15$	Location of anhydrite layer from starting node (m)
1	Pe-12	10-12	500	No	-
2	Pe-12t250	10-12	250	No	-
3	Pe-12t750	10-12	750	No	-
4	P5e-13	5x10-13	500	No	-
5	I0Pe-15	10-12	500	Yes	100
6	I200Pe-15	10-12	500	Yes	200

Acknowledgments We thank the Associate Editor Ed Baker and two anonymous reviewers for the helpful comments on the original draft of this paper. This research was supported in part by NSF grants OCE-0819084 and OCE-0926418 to R.P.L and OCE-0818783 to K.C.L.

2.8 References

Anderko, A. and K. Pitzer (1993). Equation-of-state representation of phase equilibria and volumetric properties of the system NaCl-H2O above 573K, Geochim. Cosmochim. Acta, 57, 1657-1680.

Archer, D.G. (1992), Thermodynamic properties of the NaCl+ H2O system: II. Thermodynamic properties of NaCl (aq), NaCl 2H2O (cr), and phase equilibria, J. Phys. Chem. Ref. Data,21, 793820.

Bai, W., W. Xu, and R.P. Lowell (2003), The dynamics of submarine geothermal heat pipes, Geophys. Res. Lett., 30, 1108, doi:10.1029/2002GL016176.

Baker, E.T. (2007), Hydrothermal cooling of mid ocean ridge axes: Do measured and modeled heat fluxes agree?, Earth Planet. Sci. Lett., 263, 140150.

Bichoff, J.L., and K.S Pitzer (1989), Liquid vapor relations for the system NaCl-H2O: Summary of the P-T-x surface from 300 to 500 C, Amer. J. Sci., 289 , 217-248.

Bemis, K.G., R.P. Von Herzen, and M.J. Mottl, (1993), Geothermal heat flux from hydrothermal plumes on the Juan de Fuca Ridge, J. Geophys. Res, 98, doi: 10.1029/92JB02273.

Berndt, M.E., W.E. Seyfried Jr, and D.R. Janecky (1989), Plageoclase and epidote buffering of cation ratios in mid-ocean ridge hydrothermal fluids; Experimental results in and near the supercritical region, Geochim. Cosmochim. Acta, 53, 2283-2300.

Butterfield, D.A., G.J. Massoth, R.E. McDuff, J.E. Lupton, and M.D. Lilley (1990),

Geochemistry of hydrothermal fluids from Axial Seamount Hydrothermal Emissions Study Vent Field, Juan de Fuca Ridge: Sub-seafloor boiling and subsequent fluid-rock interaction, J. Geophys. Res, 95, 12,895-12,921.

Butterfield, D.A. and G.J. Massoth, (1994), Geochemistry of north Cleft segment vent fluids: Temporal changes in chlorinity and their possible relation to recent volcanism, J. Geophys. Res., 99, 49514968.

Butterfield, D.A., R.E. McDuff, M. J. Mottl, M. D. Lilley, J. E. Lupton, and G. J. Massoth, (1994), Gradients in the composition of hydrothermal fluids from the Endeavour segment vent field: Phase separation and brine loss , J. Geophys. Res, 99, 9561-9583.

Carbotte, S.M., R.S. Detrick, A. Harding, J.P. Canales, J. Babcock, G. Kent, E. Van Ark, M. Nedimovi, and J. Diebold (2006), Rift topography linked to magmatism at the intermediate spreading Juan de Fuca Ridge, Geology, 34, 209212, http://dx.doi.org/10.1130/G21969.1.

Cherkaoui, A.S.M., W.S.D. Wilcock and E.T. Baker (1997), Thermal fluxes associated with the 1993 diking event on the CoAxial segment, Juan de Fuca Ridge: A model for the convective cooling of a dike. J. Geophys. Res., 102, 24887-24902.

Cherkaoui, A.S.M. and W.S.D. Wilcock, (1999), Characteristics of high Rayleigh number two-dimensional convection in an open-topporous layer heated from below, J. Fluid Mech., 394, 241-260.

Coumou, D., T. Driesner, S. Geiger, C.A. Heinrich, and I.S.K. Matthai (2006), The dynamics of mid ocean ridge hydrothermal systems: Splitting plumes and fluctuating vent temperatures, Earth Planet. Sci. Lett, 245, 218231.

Coumou, D., T. Driesner, P. Weisand, and A. Heinrich (2009), Phase separation, brine formation, and salinity variation at Black Smoker hydrothermal systems, J. Geophys. Res, 114, B03212, doi:10.1029/2008JB005764.

Crone, T.J., M. Tolstoy, and D.F. Stroup (2011), Permeability structure of young ocean crust from poroelastically triggered earthquakes, Geophys. Res. Lett., 38, L05305, doi:10.1029/2011GL046820.

Davis, E.E, K. Wang, R.E. Thompson, K. Becker, and J.F. Cassidy (2001), An episode of seafloor spreading and associated plate deformation inferred from crustal fluid pressure transients, J. Geophys. Res., 106, 21953-21963.

Delaney, J.R., V. Robigou, and R. McDuff (1992), Geology of a vigorous hydrothermal system on the Endeavour Segment, Juan de Fuca Ridge, J. Geophys. Res. 97, 19,663-19,682, doi/10.1029/92JB00174.

Driesner, T (2010), The interplay of permeability and fluid properties as a first order control of heat transport, venting temperature and venting salinities at mid-ocean ridge hydrothermal systems, Geofluids, 10, 132-141.

Elderfield, H. and A. Schultz (1996), Mid-Ocean Ridge hydrothermal fluxes and the chemical composition of the ocean, Ann. Rev. Earth Planet. Sci., 24, 191-224.

Faust, C.R., and J.W. Mercer (1979), Geothermal reservoir simulation: 1. Mathematical models for liquid- and vapor-dominated hydrothermal systems, Water Resour. Res., 15, 23-30.

Fontaine, F.J and W.S.D Wilcock (2006), Dynamics and storage of brine in mid ocean ridge

hydrothermal systems, J. Geophys. Res., 111, B06102, doi:10.1029/2005JB003866.
Fontaine, F.J., and W.S.D Wilcock (2007), Two-dimesional numerical models of open top hydrothermal convection at high Rayleigh and Nusselt numbers: Implications for mid-ocean ridge hydrothermal circulation. Geochem. Geophys. Geosyst., 8, Q07010, doi:10.1029/2007GC001601, 1-17.
Fontaine, F. J., W.S. Wilcock, D.A. Butterfield (2007), Physical controls on the salinity of mid-ocean ridge hydrothermal vent fluids, Earth Planet. Sci. Lett., 257, 132145.
Fontaine, F.J., W.S.D. Wilcock, D.E. Foustoukos, D.A. Butterfield (2009), A Si-Cl geothermobarometer for the reaction zone of the high-temperature, basaltic-hosted mid ocean ridge hydrothermal systems, Geochem. Geophys. Geosyst., 10, Q05009, doi:10.1029/2009GC002407. Foustoukos I. D., N.J. Pester, K. Ding and W.E. Seyfried Jr. (2009), Dissolved carbon species in associated diffuse and focused flow hydrothermal vents at the Main Endeavour Field, Juan de Fuca Ridge: Phase equilibria and kinetic constraints, Geochem. Geophys. Geosyst., 10, Q10003, doi:10.1029/2009GC002472.
Ginster, U., M.J. Mottl, and R.P. Von Herzen (1994), Heat flux from black smokers on the Endeavour and Cleft segments, Juan de Fuca Ridge, J. Geophys. Res, 99, doi: 10.1029/93JB02800.
Han, L., R.P. Lowell, and K.C. Lewis (2013), Dynamics of two-phase hydrothermal systems at a surface pressure of 25 MPa, J. Geophys. Res., 118, 2635-2647, doi: 10.1002/jgrb.50158.
Han, L., (2011), Exploring two-phase hydrothermal circulation at a seafloor pressure of 25 MPa: Application for EPR 950 N, M.S. Thesis, 86 p., Virginia Tech, Blacksburg.
Johnson, H.P., M. Hutnak, R.P. Dziak, C.G. Fox, I. Urcuyo, J.P. Cowen, J. Nabelek, and C. Fisher (2000), Earthquake-induced changes in a hydrothermal system on the Juan de Fuca mid-ocean ridge, Nature, 407:174177, http://dx.doi.org/10.1038/35025040.
Johnson, H.P., M.A. Tivey, T.A. Bjorklund, and M.S. Salmi (2010), Hydrothermal circulation within the Endeavour Segment, Juan de Fuca Ridge. Geochem., Geophys. Geosyst., 11, Q05002, http://dx.doi.org/10.1029/2009GC002957.
Jupp, T.E. and A. Schultz (2004), The physical balances in subseafloor hydrothermal convection cells, J. Geophys. Res., 109, doi: 10.1029/2003JB002697.
Kelley, D.S., J. Baross, and J. Delaney (2002), Volcanoes, fluids and life at mid-ocean ridge spreading centers. Annl Rev. Earth Planet. Sci., 30, 385-491.
Kelley, D.S. et al. (2012), Endeavour Segment of the Juan de Fuca Ridge: One of the most remarkable places on Earth. Oceanography,25(1),4461, doi/10.5670/oceanog.2012.03.
Kochinsky, A., D. Garbe-Schnberg and S. Sander et al. (2008), Hydrothermal venting at pressuretemperature conditions above the critical point of seawater, 5^0 S on the Mid-Atlantic Ridge, Geology, 36, 615618.
Lewis, K.C., and R.P. Lowell (2009a), Numerical modeling of two-phase flow in the NaCl-H2O system: Introduction of a numerical method and benchmarking, J. Geophys. Res., 114, B05202, doi:10.1029/2008JB006029. Lewis, K.C., and R.P. Lowell (2009b), Numerical modeling of two-phase flow in the NaCl-H2O system: 2. Examples, J. Geophys. Res., 114, B08204, doi:10.1029/2008JB006030.
Lilley, M.D., J.E. Lupton, D.A. Butterfield, and E. Olson (2003), Magmatic events produce

rapid changes in hydrothermal vent chemistry, Nature, 422, 878-881.
Lowell, R.P., and L.N. Germanovich (1997), Evolution of a brine layer at the base of a ridge-crest hydrothermal system, J. Geophys. Res., 102, 10,245-10,255.
Lowell, R.P. and W. Xu (2000), Subcritical twophase seawater convection near a dike, Earth Planet. Sci. Lett., 174, 385396, doi:10.1016/S0012-821X(99)00275-7.
Lowell, R.P. and L.N. Germanovich (2004), Hydrothermal processes at mid-ocean ridges: Results from scale analysis and single-pass models, in Mid-Ocean Ridges: Hydrothermal Interaction Between the Lithosphere and Oceans, Geophys. Monogr. Ser., vol. 148, ed. by C.R. German, J. Lin, and L.M. Parson, pp. 219-244, AGU, Washington, D. C.
Lowell, R.P., and P.A. Rona (2004), Hydrothermal Activity. Hydrothermal Activity, Encycl. Geology, Elsevier, 5, 362-372. Lowell, R.P., S. Gosnell and Y. Yang (2007), Numerical simulations of single-pass hydrothermal convection at mid-ocean ridges: Effects of the extrusive layer and temperature-dependent permeability, Geochem. Geophys. Geosys., 8, Q10011, doi:10.1029/2007GC001653.
Lowell, R.P., A. Farough, J. Hoover, and K.C. Cummings (2013), Characteristics of magma-driven hydrothermal systems at oceanic spreading centers, Geochem. Geophys. Geosyst., 14, doi:10.1002/ggge.20109.
Nield, D. (1968), Onset of thermohaline convection in a porous medium, Water Resour. Res., 4, 553-560, doi:10.1029/WR004i003p00553. Patankar, S. (1980), Numerical Heat Transfer and Heat Flow, 197 p., Taylor and Francis, London.
Palliser, C., and R. Mckibbin (1998), A model for deep geothermal brines, I: T-p-X state-space description, Transp. Porous Media, 33, 65-80.
Rosenberg, N.D., F.J. Spera, and R.M. Haymon (1993), The relationship between flow and permeability field in seafloor hydrothermal systems, Earth Planet. Sci. Lett, 116, 135-153.
Spiess, F. N., et al (1980), East Pacific Rise: hot springs and geophysical experiments, Science, 207, 1421-1433. Stein, C. and S. Stein, (1994), Constraints on hydrothermal heat flux through theoceanic lithosphere from global heat flow, J. Geophys. Res, 99, 3081-3095.
Tanger, J., and K. Pitzer (1989), Thermodynamics of NaCl-H2O: A new equation of state for the near-critical region and comparisons with other equations for adjoining regions, Geochim. Cosmochim. Acta, 53, 973-987.
Tivey, M.A. and H.P. Johnson, (2002) Crustal magnetization reveals subsurface structure of Juan de Fuca Ridge hydrothermal fields, Geology, 30, 979-982, doi:10.1130/0091-7613(2002).
Van Ark, E.M., R.S. Detrick, J.P. Canales, S.M. Carbotte, A.J. Haring, G.M. Kent, M.R. Nedimovi, W.S.D. Wilcock, J.B. Diebold and J.M Babcock (2007), Seismic structure of the Endeavour Segment, Juan de Fuca Ridge: Correlations with seismicity and hydrothermal activity, J. Geophys. Res, 112, B02401, doi: 10.1029/2005JB004210.
Veirs, S.R., R.E. McDuff, and F.R. Stahr (2006), Magnitude and variance of near-bottom horizontal heat flux at the Main Endeavour hydrothermal vent field, Geochem., Geophys., Geosys., 7, Q02004, doi/10.1029/2005GC000952.
Von Damm, K.L. (1990), Seafloor hydrothermal activity; black smoker chemistry and chimneys, Annual Review, Earth Planet. Sci. 18, 173-204. Von Damm, K.L. (1995), Controls on the chemistry and temporal variability of seafloor hydrothermal fluids, in

Seafloor Hydrothermal Systems: Physical, Chemical, Biological, and Geological Interactions, Geophys. Monogr. Ser., vol. 91, edited by S.E. Humphris et al., 222247, AGU, Washington, D. C., doi:10.1029/GM091p0222.

Wilcock, W.S.D. and J.R. Delaney (1996), The size of mid-ocean ridge sulfide deposits: Evidence for heat extraction from magma chambers or cracking fronts, Earth Planet Sci. Lett., 145, 49-64.

Wilcock, W.S.D. (1997), A model for the formation of transient plumes above mid-ocean ridge hydrothermal systems, J. Geophys. Res., 102, 12,109-12,121.

Wolery, T., and N. Sleep, (1976). Hydrothermal circulation and geochemical flux at mid ocean ridges. J. Geology, 84, 249-275.

Chapter 3

Thermal Response of Mid-Ocean Ridge Hydrothermal Systems to Perturbations

Accepted for publication in Deep Sea Research vol. II in 2015, with Dr. R.P. Lowell as coauthor.

Abstract

Mid-ocean ridges are subject to episodic disturbances in the form of magmatic intrusions and earthquakes. Following these events, the temperature of associated hydrothermal vent fluids is observed to increase within a few days. In this paper, we aim to understand the rapid thermal response of hydrothermal systems to such disturbances. We construct a classic single-pass numerical model and use the examples of the 1995 and 1999 non-eruptive events at East Pacific Rise $9^0$50' N and Main Endeavour Field, respectively. We model both the thermal effects of dikes and permeability changes that might be attributed to diking and/or earthquake swarms. We find that the rapid response of vent temperatures results from steep thermal gradients close to the surface. When the perturbations are accompanied by an increase in permeability, the response on the surface is enhanced further. For East Pacific Rise $9^0$50' N, the observed $\approx 7^0$C rise can be obtained for $\approx 50\%$ increase in permeability in the diking zone. The mass flow rate increases as a result of change in permeability deeper in the system, and, therefore, the amount of hot fluid in the diffused flow also increases. Using a thermal energy balance, we show that the $\approx 10^0$C increase in diffuse flow temperatures recorded for MEF after the 1999 event may result from a 3-4 times increase in permeability. The rapid thermal response of the system resulting from a change in permeability also occurs for cases in which there is no additional heat input, indicating that hydrothermal systems may respond similarly to purely seismic and non-eruptive magmatic events.

3.1 Introduction

Hydrothermal systems essentially consist of a heat source and a fluid circulation system. For high-temperature hydrothermal systems at oceanic spreading centers, the heat comes primarily from the emplacement of magma bodies in the shallow crust. The circulating fluid is mainly seawater, with some input of magmatic volatiles. In the simplest scenario, seawater enters the crust through faults and fractures and descends along permeable pathways to near the top of the magma body where it reaches temperatures exceeding 400^0C [Kelley et al., 2012]. The heated fluid then ascends through other permeable faults or fracture zones and emerges at the seafloor as mineral-rich "black smoker" vents. The temperature and composition of fluids collected at some of these vents may remain quasi-steady over months or even years (e.g. Bio 9 vent, East Pacific Rise $9^0$50' N [Von Damm., 2004], Main Endeavour Field, [Lilley et al., 2003].

Hydrothermal venting is intimately linked to the dynamic process of crustal accretion and therefore, from time to time, the output of such systems is affected by perturbations. Crustal accretion at mid-ocean ridges is a complex process which, in the simplest scenario, is a diking event [e.g., Delaney et al., 1998], where magma is emplaced as a longitudinal intrusion into the overlying oceanic crust. Dikes are often detected due to an increase in seismicity in their vicinity. Such intrusions add localized heat to the system and the changes in the near-field stress distribution may result in permeability changes that affect the circulation of the hydrothermal fluids [Craft et al., 2014]. Both these factors lead to an increase in the output of the hydrothermal system resulting in changes to the temperature and salinity of the vent fluids. For small non-eruptive diking events, the hydrothermal system may return to its original or slightly altered pre-event state [e.g. East Pacific Rise (EPR) $9^0$50' N, Fornari et al., 1998 a]; however, in some cases such perturbations may indicate a complete change in the thermal-fluid regime of the vent field and lead to permanent changes [e.g. Main Endeavour Field, Kelley et al., 2012]. Additionally such events result in change in seafloor fauna and vent chemistry [Shank et al., 1998 , Lilley et al., 2003, Seyfried et al., 2004].

Since new oceanic crust is formed by episodic magmatic activity, mid-ocean ridge hydrothermal systems are often subject to these disturbances. However, due to the scarcity of in-situ data at vent fields, very few of these events have been monitored in real time. As these events provide us special insight into the physical, chemical and biological processes at vent fields, it is important to utilize the available data to better understand how hydrothermal systems respond to magmatic and tectonic perturbations. In this paper, we construct relatively simple yet effective numerical models of a vent field for the purpose of understanding its response to small-scale disturbances. We construct quasi-one-dimensional single-pass numerical model and use the examples of East Pacific Rise (EPR) $9^0$50' N and Main Endeavour Field $47^0$57' N (MEF), two vent field that experienced non-eruptive diking in years 1995 and 1999 respectively to test the model.

Section 3.2 and 3.3 briefly describe the nature of non-eruptive events at EPR $9^0$50'

N and MEF and the previous attempts made in order to understand the propagation of perturbations. Section 3.4 and 3.5 entail out choice of model and parameterization chosen to represent the EPR and MEF vent fields. The model is tested for various scenarios for both fields and the results are reported in Section 3.6 Section 3.7 contains the interpretation of the results, implications of using a simplified model and limitations of the model.

3.2 Response of Hydrothermal Systems to Perturbations at Mid-Ocean Ridges

In March 1995, an array of nine ocean-bottom seismometers deployed on the EPR detected a total of 283 microearthquakes situated north of the $9^0$50' N area and close to Bio9 and P vents [Sohn et al. 1999]. Based on the hypocentral pattern, Sohn et al. [1999] considered a diking event unlikely and attributed the microearthquake activity to the release of thermal stresses at the base of the hydrothermal system. However, Ramondenc et al. [2008] and Germanovich et al. [2011] argue that the March 1995 seismic activity at $9^0$50'N could have resulted from a non-eruptive diking event. Germanovich et al. [2011] use numerical models to show that the dike is likely to propagate sub-vertically from the margins of the thin, lenslike magma chamber, which is characteristic of the magma chamber present below EPR. Using their model for dike propagation and hydrothermal circulation, they provide mechanical as well as hydrothermal evidence to suggest that the 1995 event was a diking event that was caused due to magma replenishment between major eruption episodes in 1991/1992 [Sohn et al., 1998] and 2005/2006 at EPR $9^0$50' N [Fornari et al., 2012].

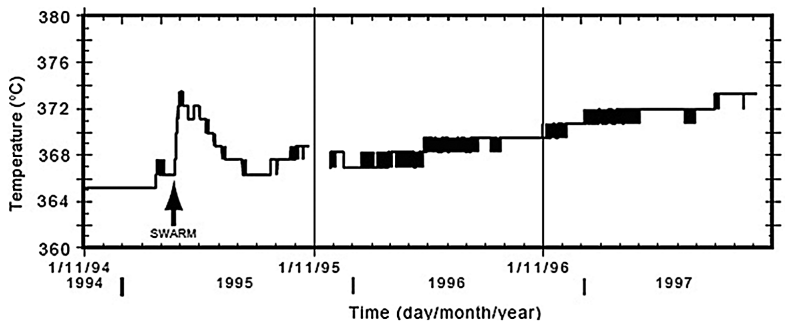

Figure 3.1: Thermal response of the Bio9 vent at East Pacific Rise $9^0$50′ N [from Sohn et al., 1998], Nature, 396, 159161, 1998.

A similar period of elevated seismic activity was observed in June 1999 for the Endeavour Segment [Johnson et al., 2000; Lilley et al., 2003] in which the Main Endeavour Field was affected most strongly [Kelley et al. 2012]. The activity lasted 5-11 days and spanned the along-axis region above the magma chamber [Johnson et al., 2000]. Initially, this event was thought to be of tectonic origin [Johnson et al. 2000]; however, the 1999 event also caused dramatic increases in CO^2 and H^2 concentrations in the vent fluids [Lilley et al., 2003].

As these observations indicated high-temperature water/rock reactions, Lilley et al. [2003] argued that the chemical data from the hydrothermal fluids collected in September 1999 and June 2000 was more consistent with a magmatic event. Bohnenstiehl et al. [2004] showed
655 that the seismic activity migrated southward 12 km along-axis at a rate of 1.1 km/hour, thus indicating that the seismicity was the result of a lateral dike injection.

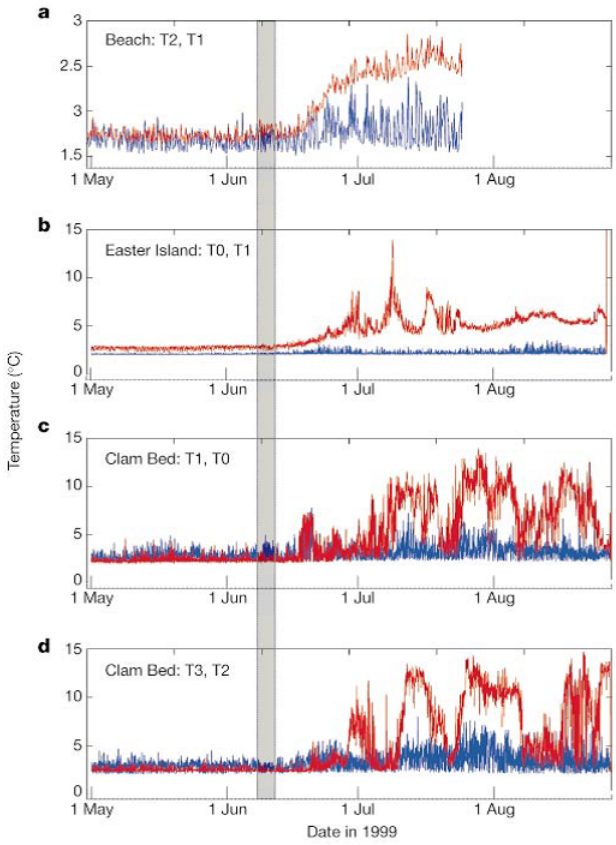

Figure 3.2: Temperature data from the three Endeavour axial valley sites. Red traces, data from thermistors located within hydrothermal fluids from vents; blue traces, data from thermistors deployed in the adjacent (non-vent) bottom water at each site. (a). Data from the bio-column thermistors at the Beach site, located in a diffuse vent within a sediment pond 200m south of the MEF. The earthquake activity (815 June 1999) is marked by the vertical shaded bar. Note that the temperature scale for this site is different from the other three sites shown. (b). Temperatures from the EI/MEF site, showing the slow temperature rise after the 8 June event. (c). Data from one of the Clam Bed thermistor pairs, near the High Rise vent field. (d). Temperature data from the Clam Bed site, located only a few tens of meters from those in c.

At EPR, the temperature data collected by Sohn et al. [1998] for the Bio9 vent showed

that vent temperature was stable for approximately 15 months prior to the March 1995 event at $\sim 365^0$ C. After the March 22 event, the vent temperature increased by 7^0 C over 8 days (Figure 3.1), and gradually returned to normal after several months. Similarly at the MEF, temperatures had remained stable for nearly 10 months prior to the earthquakes after which Johnson et al. [2000] observed a temperature rise up to $\sim 10^0$C in the diffuse flow sites approximately 4-11 days after the first event on June 8, 1999 (Figure 3.2). Many high temperature vents within the MEF increased by 15^0C and some vents emitted fluids that were nearly fresh [Lilley et al., 2003; Kelley et al., 2012].

The examples listed above illustrate that seafloor hydrothermal systems are sensitive to diking events and that the temperature response is quite rapid. This is in sharp contrast with numerical models of two-phase flow in porous media subject to changes in basal heat flux [Singh et al. 2013; Choi and Lowell, 2014], in which the temperature response is strongly damped and may not be manifest for months or years after the event. Hence, the nature of the response of these vent fields to diking events might provide new insights into magma-hydrothermal processes on the seafloor.

In both cases, the time delay between the start of seismicity and the first response of the hydrothermal system was hypothesized to reflect the time needed for the hydrothermal fluids to traverse the system [Fornari et al., 1998 and Sohn et al., 1998; Johnson et al., 2000]. Because the events were considered to be thermal cracking events taking place at the magma-hydrothermal boundary layer [Fornari et al., 1998 and Sohn et al., 1998], this would imply that fluids travel several thousands of meters in the crust in a few days or hours. Germanovich et al. [2011] and Lowell et al. [2013] show, however, that a typical mass flow rate for high temperature hydrothermal systems of ~ 100 kg/s would yield a hydrothermal fluid speed $\sim 10^5 - 10^6$ m/s over the area of the hydrothermal discharge zone. To traverse ~ 1000 m at these speeds would require several weeks if not months, even if the speed is increased by an order of magnitude as a result of the event.

Given that the observed thermal response to non-eruptive dikes is too fast to reflect fluid transit times from deep in the hydrothermal system, the question remains as to the response mechanisms. This question has been addressed by a number of different approaches, as we outline in the next section, but important questions remain regarding the relative roles of heat input and permeability changes.

3.3 Previous Modeling Work

3.3.1 Thermal and pressure perturbation mechanisms

Wilcock [2004] investigated two mechanisms that could potentially account for the hydrothermal response to the March 1995 seismic swarm at EPR $9^0$50' N. One mechanism assumed a thermal perturbation at the base of the discharge channel that was carried by fluid ascending a vertical fracture of constant width or a cylindrical pipe of constant radius.

His results showed that the observed temperature increase could be achieved by a temperature perturbation of 50^0C at a depth of 1 km if fluid flowed in single vertical crack of width d = 0.7 mm. This would correspond to an effective crack permeability of approximately 5 x 10^-8 m^2, assuming the relation k = $d^2/12$ [e.g., Bear, 1972]. To fit the temperature record, the temperature perturbation was assumed to decay linearly with time and was followed by a second, smaller thermal pulse associated with a second seismic swarm that occurred 24 days following the initial one. For this to be correct, the fluid flow in the crack would have to be 1 m/s and the travel time would be $\sim 10^3$ s. Wilcock proposed that the delayed thermal response results from the disequilibrium between the temperature of the fluid in the crack and the wall rock.

The second mechanism attributed the thermal response to pressure perturbations that could arise from decrease in porosity. However, this could be made to fit the observed thermal response only when the permeability value of the discharge zone was < 10-14 m^2. He noted that such permeability value was considerably less than typically thought for high temperature hydrothermal systems [e.g., Wilcock and McNabb, 1996; Lowell and Germanovich, 1994, 2004] and hence, favored the thermal perturbation mechanism. Wilcocks [2004] analysis was done before heat flow data were available to constrain the flow rate, permeability, and other parameters related to the EPR hydrothermal system [Ramondenc et al., 2006; Lowell et al., 2013].

Following the data published in Ramondenc et al. [2006], Germanovich et al. [2011] used a planar parallel crack calculation to show that, with reasonable values of permeability, flow rate and other parameters, using Wilcocks [2004] thermal perturbation model would yield a response time ∼4 x 10^8 s or ∼12 years, which is much too long. Alternatively, to obtain a response time given by Wilcock [2004], the permeability would have to be much greater than appears reasonable based on the observed temperature and heat flux at EPR EPR $9^0$50' N. Therefore the rapid response observed at EPR $9^0$50' N could not be attributed to a thermal perturbation deep in the system with fluid traversing ∼1000 m through a crack system.

3.3.2 Effect of a thermal boundary layer and permeability changes associated with diking

In order to address the rapid response time of the thermal perturbation at EPR $9^0$50'N, Ramondenc et al. [2008] suggested that the thermal response had a shallow origin in the crust. To test this idea, they constructed a 2-limb single-pass model to take into account both deep and shallow recharge and the resulting focused and diffused flow at the surface. In their model, mixing between cold seawater and hot hydrothermal fluid formed a thermal boundary layer in the mixing zone which they placed within the top 100 m of the crust, to represent layer 2A extrusives. At an arbitrary point within this zone, they measured the temperature of the high-temperature fluid they consider to represent focused flow, taking into account some small amount of mixing between seawater and the rising hot hydrothermal fluid. They also assumed that diffuse flow resulted from additional mixing between seawater

and high-temperature fluid and that another boundary layer existed near the seafloor where this mixed fluid exited at a temperature corresponding to diffuse flow. The result of this model was that a change in the temperature in the mixing zone would result in a rapid response at the surface, as the perturbed fluid only had to traverse a relatively short distance within the extrusives. Ramondenc et al. [2008] argued that modest increases in permeability occurring near the dike were sufficient to generate observable thermal perturbations to the boundary layer in the mixing zone. The increased temperature in the black smoker fluid induced additional mixing with seawater that led to a subsequent decrease in the perturbed temperature at EPR $9^0$50' N (Figure 3.1).

In Ramondenc et al. [2008], however, the mass flow rate for EPR $9^0$50' N was assumed to be between 14-26 kg/s, which is much lower than the value of ∼80 kg/s estimated by Germanovich et al. [2011] and Lowell et al. [2013]. These values resulted in a lower heat flux and permeability than estimated for EPR. Germanovich et al. [2011] further addressed the magmatic origin of the EPR thermal perturbation by modeling dike propagation from the magma lens and using values of mass flux based on heat output data in Ramondenc et al. [2006] to estimate flow resistances in the recharge and discharge limb. Germanovich et al. [2011] emphasized that it was the change in permeability associated with diking that caused the observed rapid perturbations and not the presence of the thermal boundary layer in the mixing zone, as they did not observe a rapid response when cracking was not included. Additionally, their model used geometrical parameters of EPR $9^0$50' N and the diking event of 1995, and therefore was constrained by observational parameters (dike width and height) associated with that particular event.

3.3.3 Motivation

Although we agree with the basic premise of Ramondenc et al. [2008] and Germanovich et al. [2011] that changes in permeability in the diking zone can produce a rapid thermal response on the surface, we believe that the rapid response results from both the increase in permeability and presence of a thermal boundary layers close to the surface associated with both high-temperature and diffuse venting. These boundary layers result in steep gradients in temperature close to the seafloor. As a result of the increase in permeability due to diking, the flow rate changes quickly, which causes hotter fluids within the near-surface boundary layers to emerge on the seafloor. The treatment of the boundary layer here is different from that in Ramondenc et al. [2008] and Germanovich et al. [2011] in which the thin, shallow mixing zone serves as the boundary layer for high temperature flow. Above this zone, the mixed fluid cools to the diffused flow temperature in a near-surface boundary layer. Here, we use a classical single-limb single pass model and assume the boundary layer for high-temperature discharge results by applying a mixed or radiative boundary condition at the seafloor [Carslaw and Jaeger, 1986]. The diffuse flow component of the flow is not considered in the model. The details of the single pass model and equations are provided in Appendix A.

In the single pass model, high-temperature hydrothermal fluid rises nearly isothermally until it is affected by the radiative boundary condition which cools the fluid to observed black smoker temperatures. This allows the fluid to cool both conductively and advectively, depending upon its velocity and has been used previously in hydrothermal models of the seafloor [Germanovich et al., 2000, 2001]. As high temperature hydrothermal fluid comprises nearly 80-90% of the hydrothermal heat output from mid-ocean ridge systems [Lowell et al., 2013], we feel that the model presented here provides us with a good understanding of such flows and their response to perturbations. We discuss the limitations of this approach in Section 3.7.

In the model developed here, we use acceptable values of permeability and mass flow rate, along with values of other vent field parameters (where available) for EPR and MEF and determine the response of the vent field to a diking event. In addition to modeling these particular events, by using the observational constraints available for EPR and MEF both before and after the diking events of 1995 and 1999 respectively (Table S1), we investigate a range of parameter space for the width and height of the dike and potential increases in permeability resulting from dike injection in order to understand the effects of these parameters on the thermal response. For both the EPR and MEF vent fields, we also consider the case in which there is no diking but only an increase in permeability resulting from earthquakes deep in the system.

3.4 The Classic Single-pass Model

In the classical single-pass model of a hydrothermal circulation system, conservation of mass, momentum and energy are expressed in terms of total mass flow Q (kg/s) , mean fluid discharge temperature T_d, and advective heat output H at the vent field scale as fluid circulation occurs through discrete pathways [e.g., Elder 1981; Lowell et al., 2013]. For a magma-driven seafloor hydrothermal system, these pathways generally consist of a deep recharge zone, a cross-flow zone that transfers heat by conduction across a thermal boundary layer from a subjacent axial magma chamber (AMC), and a deep discharge zone through which the hydrothermal fluid vents to the seafloor [e.g., Lowell and Burnell, 1991; Lowell and Germanovich, 1994, 2004; Lowell et al., 2013]. The observed values of T_d and H are used to determined Q, and the observations of the vent field area Ad and planform area of the AMC A_m can be used to determine the conductive boundary layer thickness d and the bulk permeability of the discharge zone k_d. The single pass model therefore provides important constraints on hydrothermal parameters at the vent-field scale. Figure 3.3 is a cartoon showing the assumed flow path in the single-pass model and associated symbols. The definitions of all symbols are given in Table 3.1. We use these estimates of parameters for MEF and EPR $9^0 50'$ [Lowell et al., 2013] to construct a fully numerical 1-D code. The details of the model construction, mathematical formulation, boundary conditions and solution method for their model are provided in Appendix A.

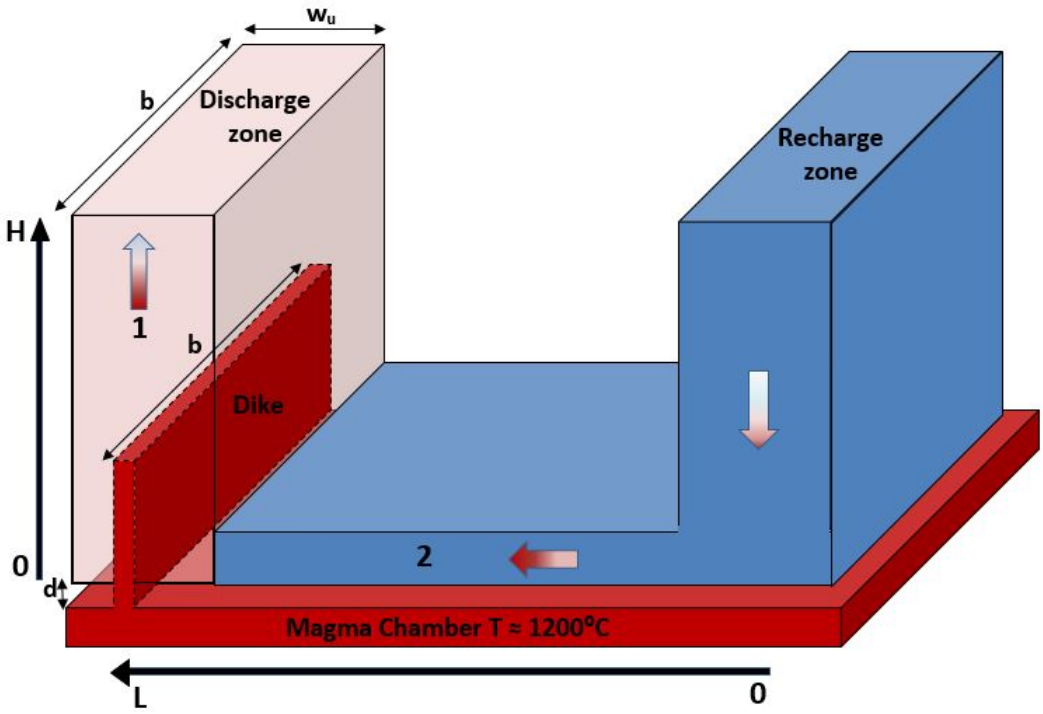

Figure 3.3: Cartoon of the single-pass model showing key features. For meaning of legends please see Table 2.1.

3.5 Parametrization

For both the EPR and MEF vent fields, the values of discharge temperature Td and mass flow rate Q are obtained from Lowell et al., 2013. Far field surface temperature is assumed to be 0^0C and increasing 0.05^0C/m with depth. This thermal gradient is used to calculate recharge temperature Trech for the vent field. The values of T_d, Q and T_{rech} along with other thermodynamic parameters are used to estimate the permeability k for the model. For EPR, the steady state recharge temperature $T_{rech} = 75^0$C. The discharge temperature $T_d = 371^0$C is obtained for mass flow rate $Q = 86$ kg/s and permeability $k = 5\text{x}10^{-}13$ m^2. For MEF, the steady state recharge temperature $T_{rech} = 100^0$C, corresponding to a deeper circulation system than EPR (Table 3.1). The discharge temperature Td = 365^0C is obtained for $Q = 246$ kg/s and permeability $k_d = 4\text{x}10^{13}$ m^2. These values are used to obtain the steady state solutions for EPR (Figure 3.4) and MEF (Figure 3.5) respectively, using equation (14) of Appendix A and parameters shown in Table 3.1. The steady state is used as a starting solution for the time dependent equation (Equation (9) in Appendix A). The time dependent simulation runs until the solution stabilizes (∼5 days), and then the perturbation is introduced in the model. The dimensions of the dike are parameterized as dike width w

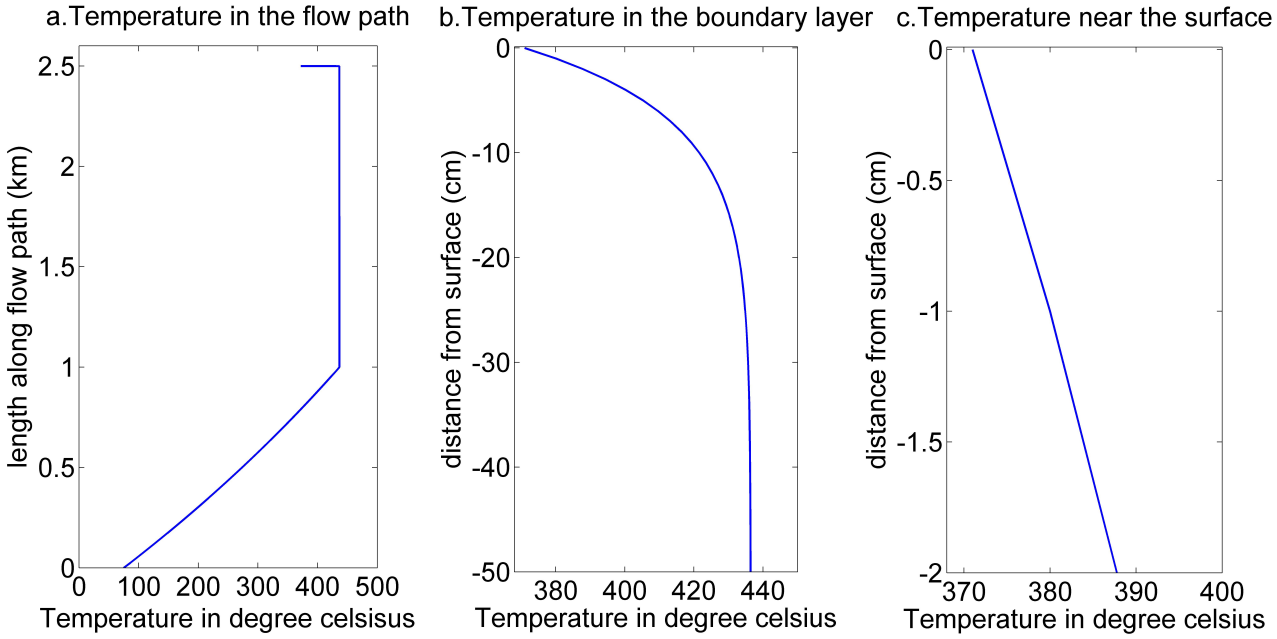

Figure 3.4: Temperature distribution for East Pacific Rise in steady state (a) for the whole system for (b) for the boundary layer (c) near the surface.

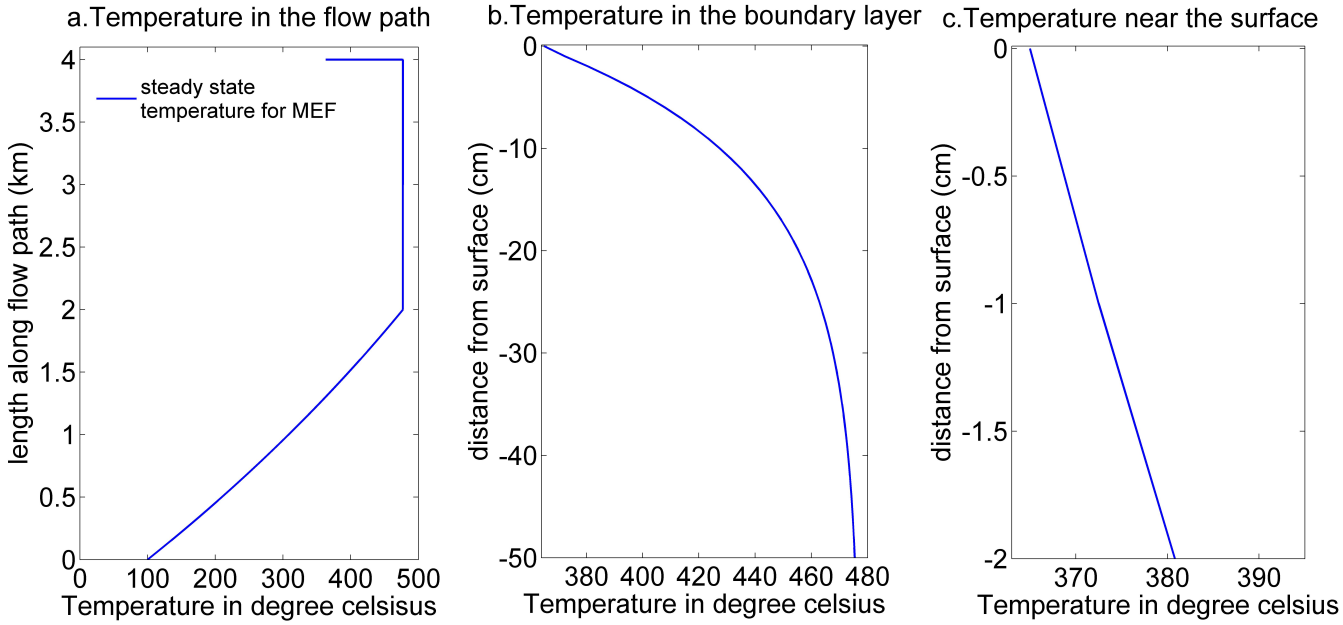

Figure 3.5: Temperature distribution for Main Endeavour Field in steady state (a) for the whole system for (b) for the boundary layer (c) near the surface.

and dike height h to quantify the quantity of magma emplaced and its location with respect to the surface. To take into account the cracking of surrounding rock caused by diking, k is increased in the diking region. This also enables us to simulate a purely tectonic event in which case there is no magmatic intrusion ($w = 0$, $h = 0$). All simulations run for a total of 30 days. Following sections describe the parameterization of variables for EPR and MEF respectively.

3.5.1 East Pacific Rise

Germanovich et al. [2011] apply a 2-D model to study the 1995 diking event at EPR $9^0$50' N. They use the distribution of earthquake hypocenters observed by the OBS array [Sohn et al., 1998] to visualize a sub-vertical dike with a height h of 600 m above the magma chamber lens and width w of 1m. As this dike geometry is quantified in their work from both mechanical and hydrothermal standpoints, we use the same values of h and w for the models of EPR $9^0$50' N presented here. The main parameter which is varied for the model of EPR $9^0$50' N is the permeability in the diking zone which is increased by 10% - 1000% from the permeability prior to dike input. As mentioned previously, the case in which there is no dike emplacement is also considered with the same range of permeability increase in the deep discharge zone. These scenarios are compared with dike emplacement that is not accompanied by increase in permeability in the diking zone. The goal is to obtain the $\sim 7^0$C rise in temperature which was observed at Bio9 approximately 4 days after the event.

3.5.2 Main Endeavour Field

Constraints for the modeling of the June 1999 event can be obtained from the various studies conducted at the MEF following the event. In-situ data collected by Johnson et al. [2000] showed that diffused-flow temperatures in the Easter Island site (located within the MEF), as at some sites outside the MEF (Figure 3.2) increased within 4-11 days of the start of seismicity. Kelley et al. [2012] report that many chimneys within the MEF recorded temperature hikes 15^0C. Additionally, Davis et al. [2001] use pressure transient data from Integrated Ocean Drilling Program (IODP) boreholes to suggest that the lateral dike injection at MEF spanned 40 km in length and 3 km in depth.

Although the thermal perturbation at MEF in 1999 appears to be associated with dike emplacement, the details of the diking event are not well-constrained. Consequently, we investigate potential temperature perturbations to the MEF for a range of possible diking scenarios. We consider dike widths $w = 1$, 2, 10, 20 m (for $h = 500$ m) to compare the effects of various amounts of magma emplacement in the crust and dike heights $h = 250$, 500, 750, 1000 m (for $w = 2$ m) to study the effect of dike penetration closer to the surface. We also consider increases in permeability in the diking zone ranging between 10 and 1000 % ($w =$ 2 m, h = 500 m) of the initial permeability. Similar to the EPR case, we have modeled the MEF for increase in permeability with no dike emplacement.

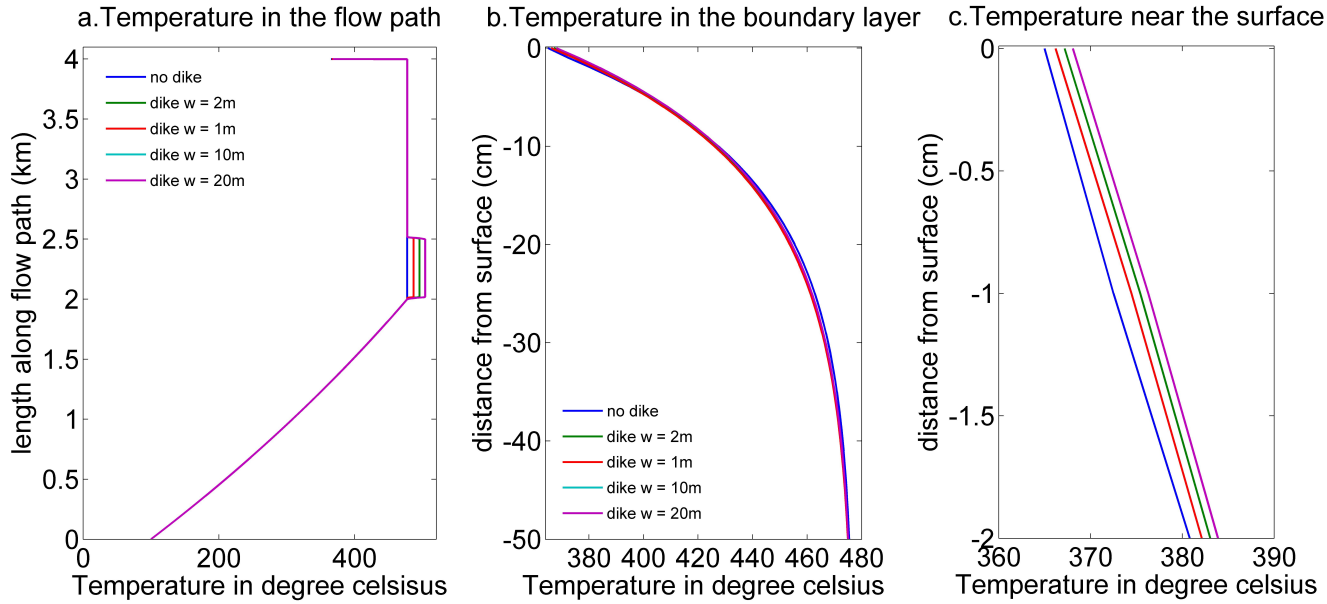

Figure 3.6: Temperature distribution for Main Endeavour Field in steady state (blue) and perturbed state for dike w = 1, 2, 10 and 20 m (a) for the whole system for (b) for the boundary layer (c) near the surface. Values were plotted $\sim$ 25 days after dike emplacement.

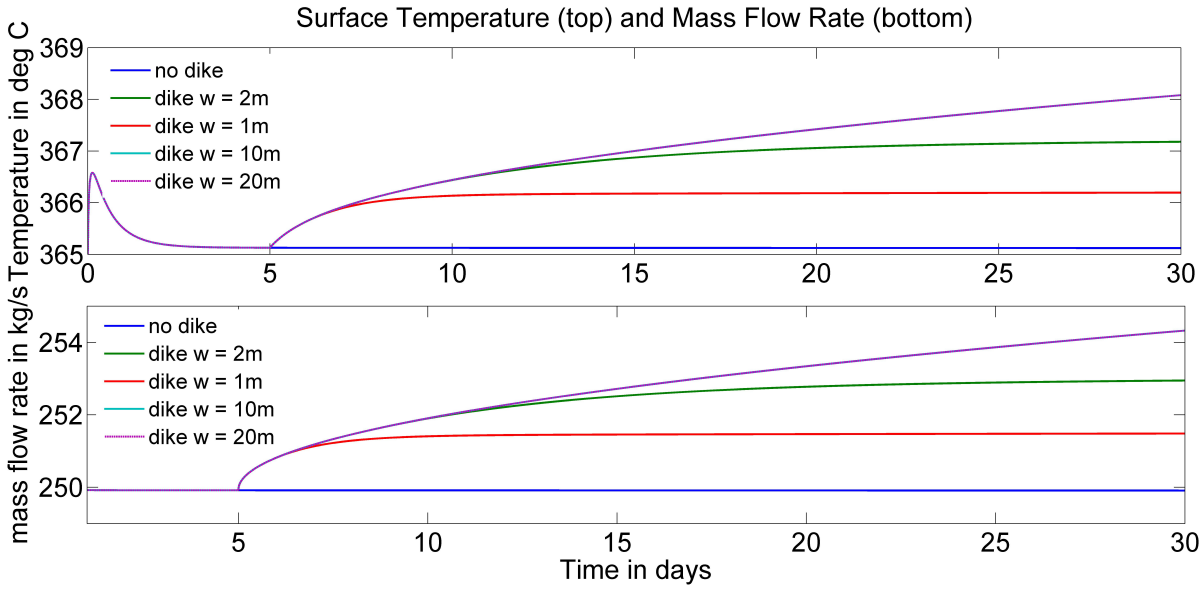

Figure 3.7: Temperature at the surface (top) and mass flow rate (bottom) for Main Endeavour Field in steady state (blue) and perturbed state (other colors) for dike w = 1, 2, 10 and 20 m, $\sim$ 25 days after diking event.

We aim at obtaining a response ∼4-11 days after the event that is at least half (7^0C) of the total 15^0C response.

3.6 Numerical Results

Sections 3.6.1 and 3.6.2 present results obtained for various dike widths and heights for MEF as 'w' and 'h' are constant in all models for EPR. The results for increasing local permeability in the perturbation zone for both EPR and MEF are presented in section 3.6.3.

3.6.1 Effect of dike width 'w'

Emplacing a thicker dike in the model for MEF adds more heat to the system. As the width of the dike is increased, the temperature in the diking zone, as well as the temperature on the surface increases (Figures 3.6 and 3.7). It may be noted that the temperature both deep within the system and near the surface are for dike $w = 10$ m and $w = 20$ m are overlapping. This is because the time for dissipation of latent heat of cooling for thinner dikes is ~ 1 day ($w = 1$ m) and 4 days ($w = 4$ m) respectively, whereas for thicker dikes, this time is ~ 100 days. Note that temperature profiles in Figure 3.7 overlap when time elapsed after the diking is ~ 4 days. Therefore in cases where the injected dike is ~ 10 m thick, the temperature in the diking zone as well as on the surface will continue to rise steadily for months.

Although emplacement of such a large quantity of magma ($w = 10$, 20 m) in the crust is improbable, the model allows us to calibrate the nature of the response of a hydrothermal system to both thin and thick dikes which are emplaced without an increase in permeability. For such dikes, bottom temperature increases as the dike cools which creates a pressure gradient causing a gradual increase in the Q of the system. This gradual change in Q is reflected in a small change in temperature on the surface. While the surface temperatures for thicker dikes are still increasing after ~ 25 days, the temperature profiles for thinner dikes have reached their peak showing that for $h = 500$ m and for moderate w, the maximum rapid perturbation on the surface is $\sim$ 2degC. It should also be noted that this change is observed nearly 25 days after dike emplacement and not in the observed 4-11 day time-window. Therefore, emplacement of a larger amount of magmatic material in the crust alone cannot produce a rapid and pronounced response on the surface in a short time period. It can, however, contribute to gradual rise in temperatures over longer periods of time.

3.6.2 Effect of dike height 'h'

Figure 3.8 shows that placing the dike higher in the crust in the model for MEF causes the temperature in the upflow zone to be higher closer to the surface (Figures 3.8 and 3.9). 5 days after the input of the dike, the temperature increases by 0.5^0C - 2^0C while the mass flow rates increases by 2-4 kg/s. Similar to when w is increased, the mass flow rate and the

900 temperature on the surface increase gradually as the dike cools. Predictably, the closer the

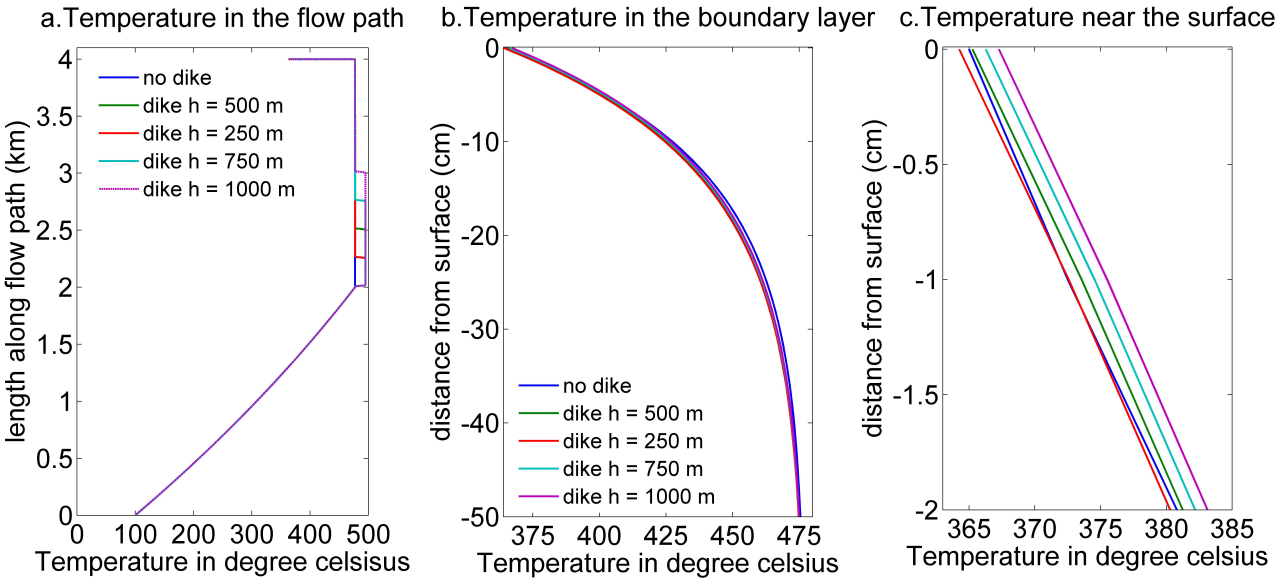

Figure 3.8: Temperature distribution for Main Endeavour Field in steady state (blue) and perturbed state for dike h = 250, 500, 750 and 1000 m (a) for the whole system for (b) for the boundary layer (c) near the surface. Values were plotted $\sim$ 25 days after dike emplacement.

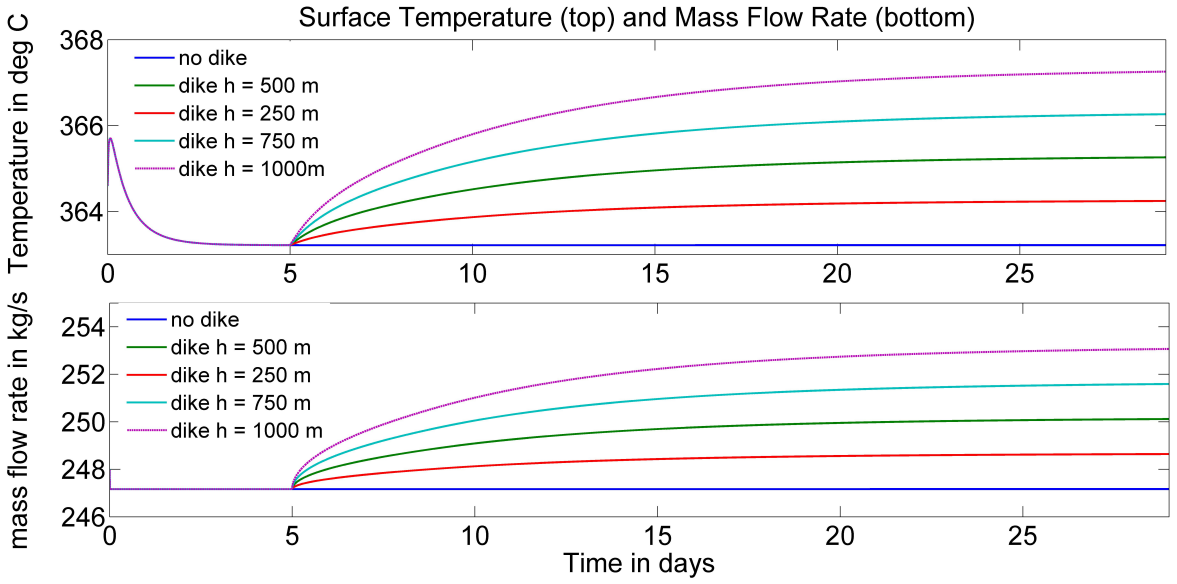

Figure 3.9: Temperature at the surface (top) and mass flow rate (bottom) for Main Endeavour Field in steady state (blue) and perturbed state (other colors) for dike h = 250, 500, 750 and 1000 m, $\sim$ 25 days after diking event.

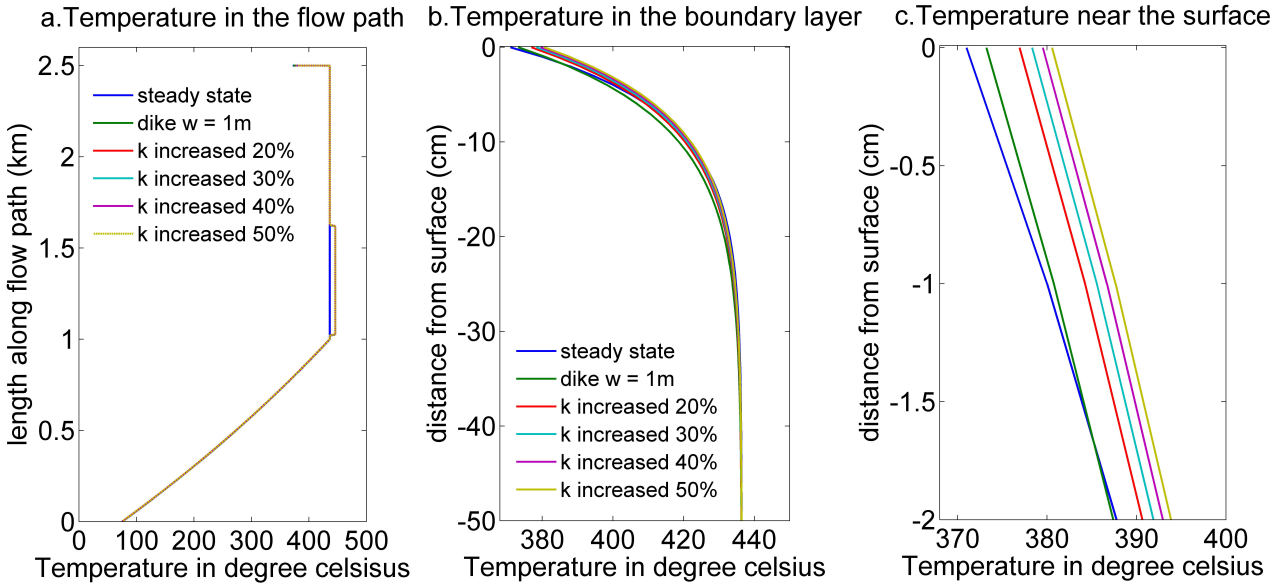

Figure 3.10: Temperature distribution for EPR $9^0$50' N in steady state (blue) and perturbed state when k in the diking zone is increased by 10%, 20%, 50% and 2 times (a) for the whole system for (b) for the boundary layer (c) near the surface. Values were plotted $\sim$ 25 days after dike emplacement.

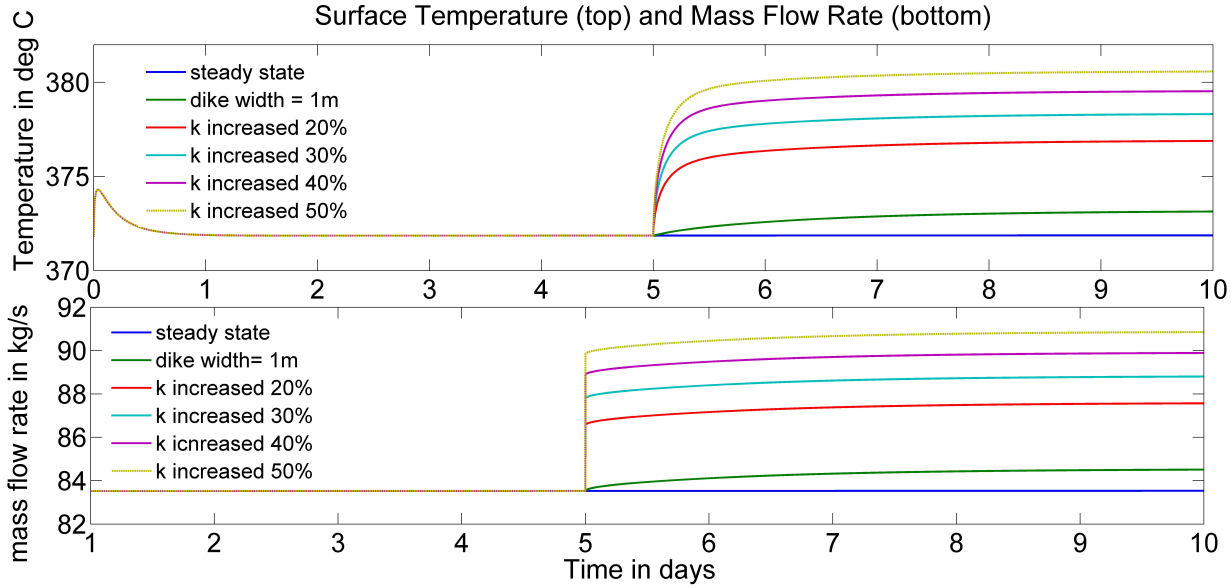

Figure 3.11: Temperature at the surface (top) and mass flow rate (bottom) for EPR $9^0$50' N in steady state (blue) and perturbed state (other colors) when k in the diking zone is increased by 10%, 20%, 50% and 2 times, $\sim$ 25 days after diking event.

dike is to the surface, the higher the temperature is (Figure 3.9). However, the time frame of the response to the dike remains the same.

3.6.3 Effect of increase in permeability 'k'

3.6.3.1 In case of diking: For both EPR and MEF, increasing the k does not increase the temperature in the diking zone (Figures 3.10 and 3.12) beyond what was calculated for the effect of heat loss from the dike, unlike the two previous cases. However, it has a significant impact on the Q (Figures 3.11 and 3.13) of the system and consequently, on the surface temperature. For EPR, the Q increases by ∼7-10 kg/s (Figure 3.11) almost instantaneously with the dike emplacement for 50% increase in permeability. Within 1 day of diking, temperature on the surface increases by $\sim 7^0$C. Similarly for MEF, increasing k by 50% causes Q to increase by ∼15 kg/s and surface temperature to increase by $\sim 10^0$C. The increase in temperature in both cases can also be observed in Figures 3.10 (c) and 3.12 (c) where there is a clear jump in temperature close to the surface.

3.6.3.2 In case of no dike intrusion: Figures 14-17 show that even with no additional heat input from a dike, the temperatures on the surface increase rapidly when the permeability of the discharge zone increases. In such cases, temperature in the 'perturbed' zone does not increase (Figures 3.14(a) and 3.16(a)) but the temperature at the surface increases due to the increase in the mass flow rate of the system (Figures 3.15 and 3.17). While this can be treated as a purely tectonic or a 'cracking' event, the response on the surface is not due to the exposure of the fluid to hotter rock but due to the increased rate of heat extraction from this system. This eventually leads the temperature in the 'cracking' zone to decrease.

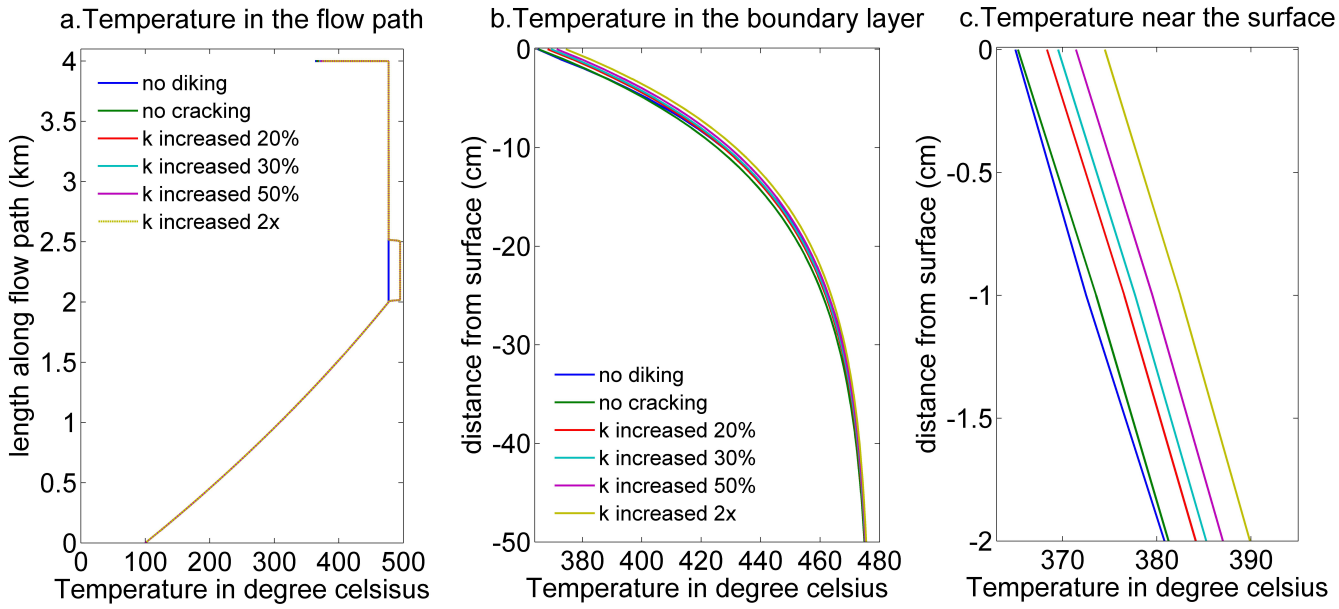

Figure 3.12: Temperature distribution for Main Endeavour Field in steady state (blue) and perturbed state when k in the diking zone is increased by 10%, 20%, 50% and 2 times (a) for the whole system for (b) for the boundary layer (c) near the surface. Values were plotted $\sim$ 25 days after dike emplacement. Dike w = 2 m, and h = 500 m.

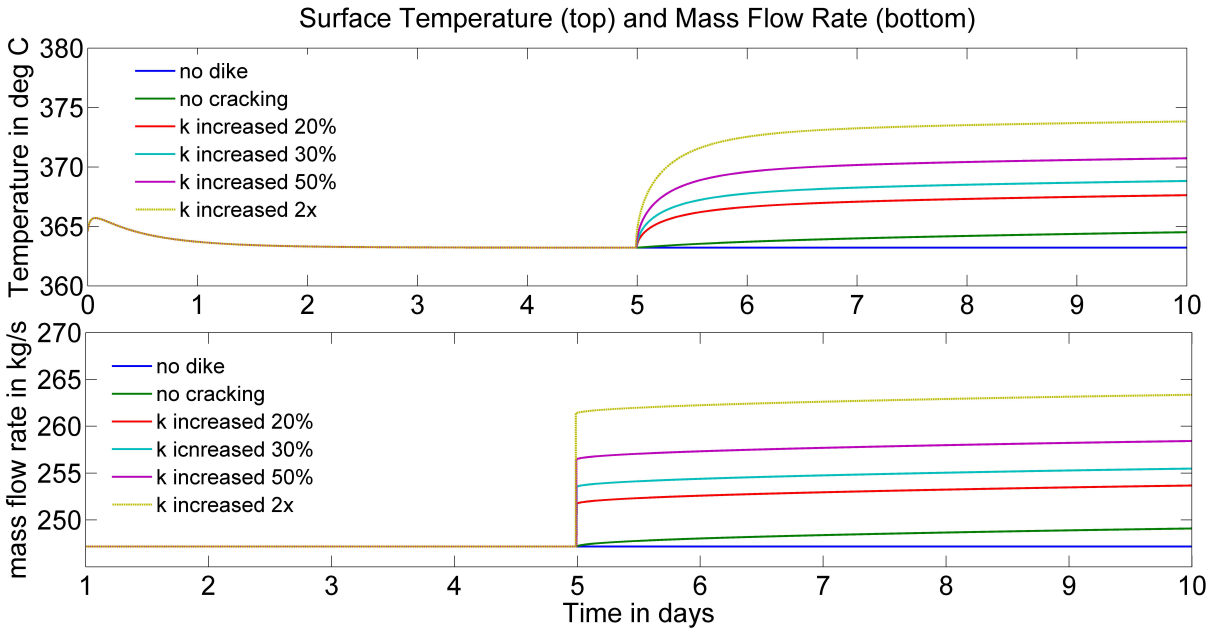

Figure 3.13: Temperature at the surface (top) and mass flow rate (bottom) for Main Endeavour Field in steady state (blue) and perturbed state (other colors) when k in the diking zone is increased by 10%, 20%, 50% and 2 times, 25 days after diking event.

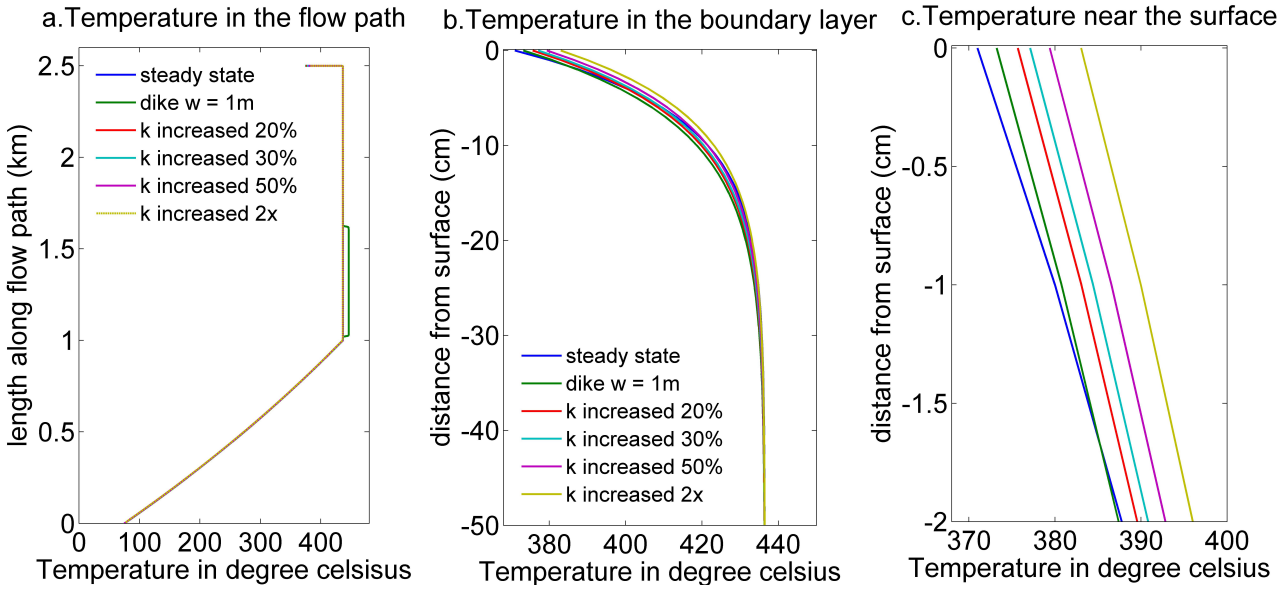

Figure 3.14: Temperature distribution for EPR $9^0$50' N in steady state (blue) and perturbed state for no diking scenario when k in the diking zone is increased by 10%, 20%, 50% and 2 times (a) for the whole system for (b) for the boundary layer (c) near the surface. Values were plotted $\sim$ 25 days after the event.

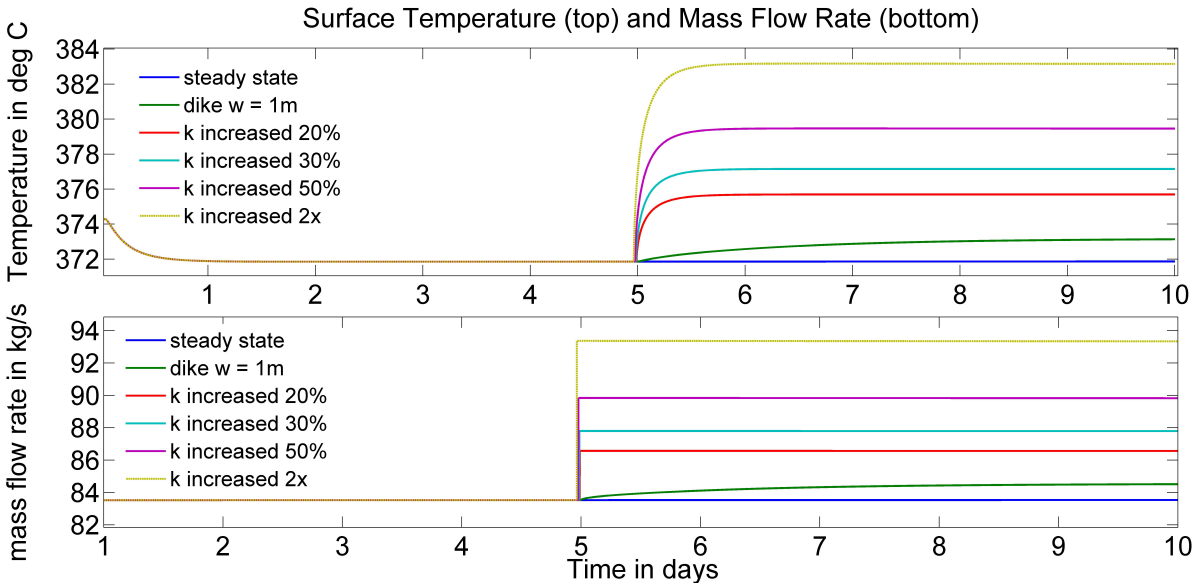

Figure 3.15: Temperature at the surface (top) and mass flow rate (bottom) for EPR $9^0$50' N in steady state (blue) and perturbed state (other colors) for no diking scenario when k in the diking zone is increased by 10%, 20%, 50% and 2 times, $\sim$ 25 days after the event.

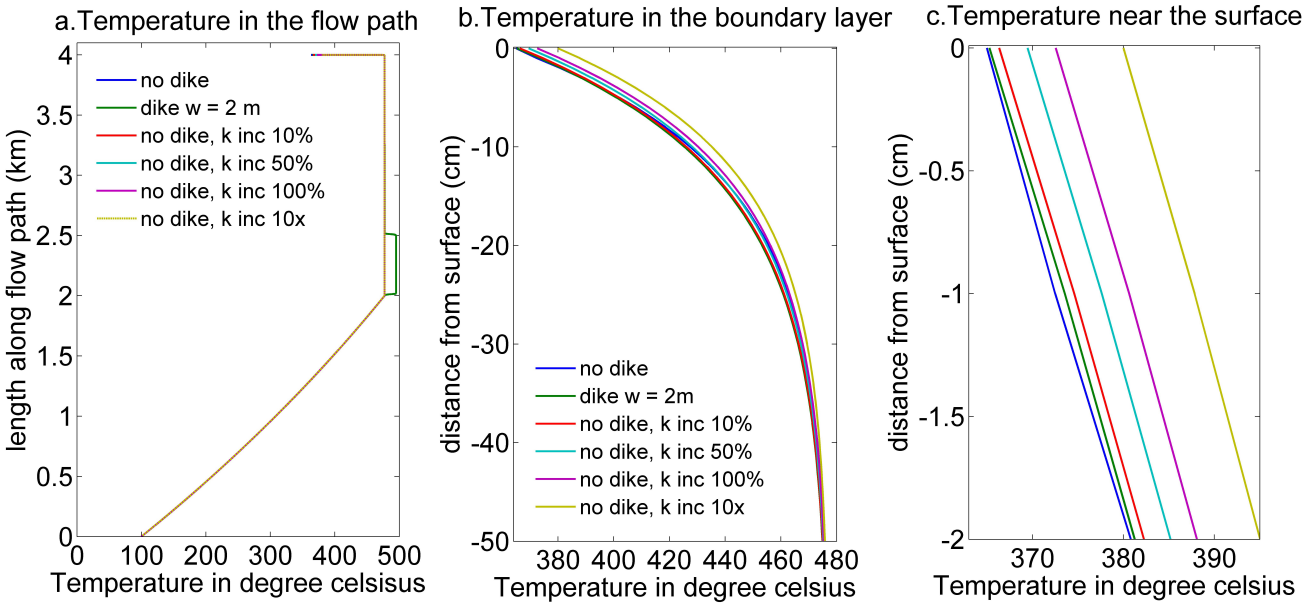

Figure 3.16: Temperature distribution for Main Endeavour Field in steady state (blue) and perturbed state for no diking scenario when k in the diking zone is increased by 10%, 20%, 50% and 2 times (a) for the whole system for (b) for the boundary layer (c) near the surface. Values were plotted $\sim$ 25 days after the event.

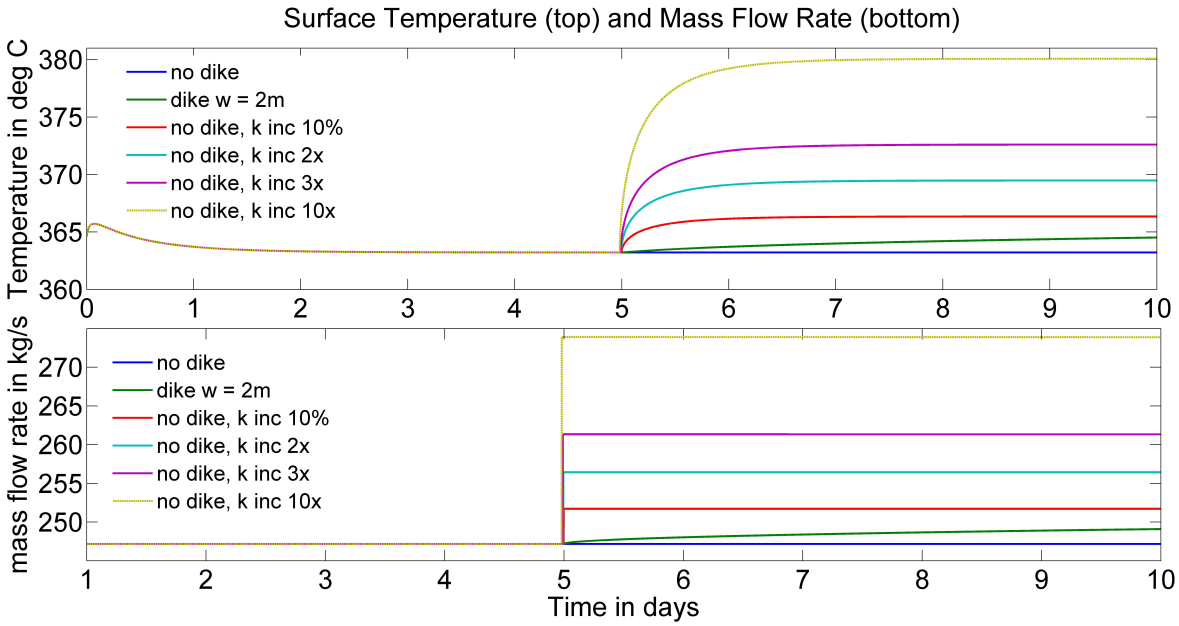

Figure 3.17: Temperature at the surface (top) and mass flow rate (bottom) for Main Endeavour Field in steady state (blue) and perturbed state (other colors) for no diking scenario when k in the diking zone is increased by 10%, 20%, 50% and 2 times, $\sim$ 25 days after the event.

3.7 Discussion

3.7.1 Vent-Field Scale Single Pass Model

Constructing a single-pass model for a hydrothermal vent field is quantitative, though simplified, approach to modeling at the vent-field scale. The discharging fluid flow Q represents the mass flow rate of high temperature hydrothermally derived vent fluid for the entire vent field and not for individual vent structures (e.g. for EPR, Bio9 and P vents; for MEF, Hulk, Dante, etc.). As the supply of this hot fluid to each of the vent structures is dependent on local factors such as distribution of permeability, mineral precipitation, and partial mixing with cold surface recharge, the thermal response of individual vent structures is hard to determine. Lowell et al. [2013] show, however, that 80-90% of the emerging fluid has a high-temperature component driven by heat transfer from the underlying magma chamber. Therefore studying the entire vent field and its response to perturbations provides a broad understanding of the parameters controlling the behavior of the vent field.

Another artifact of using a single-pass model is that the fluid rises to the surface essentially isothermally before it cools just underneath the surface. Therefore, although temperatures of $\approx 500^0$C are reasonable for the deep discharge zone, it is unlikely that fluids retain

this temperature as close to the surface ($\sim$ 50 m) as indicated in these models. Numerical models suggest a significant degree of mixing between the high-temperature phase-separated fluid ascending form the base of the hydrothermal system and cooler single-phase seawater. In light of this, one might think that the effect of the boundary layer is somewhat overstated in these models due to the sharp temperature gradients close to the surface. In order to test this idea, we construct a generic model (in Appendix A) with fluid discharge temperature $\approx 400^0$C which is reasonable for both deep discharge [Jupp and Schultz, 2002] and surface high temperature discharge [Delaney et al., 1998; Kelley et al., 2012]. In this case the hydrothermal fluid cools by $\sim 30^0$C close to the surface. With this relatively smaller change in temperature too, the surface temperature responds in a way similar to that presented in this paper (Figures A1 and A2, Appendix A).

3.7.1.1 Decay of vent temperatures after the event: Shallow sub-surface circulation of seawater is likely to accompany deep hydrothermal circulation. This occurs because the high-temperature plume produces lateral thermal gradients in the higher permeability of the extrusives [e.g.; Craft and Lowell, 2009]. Ramondenc et al. [2008] use their model to argue that this shallow circulation plays the role of regulating the surface temperature of the fluids. Any additional heat in the system causes the buoyancy driving the shallow circulation to increase and the resultant enhanced flow of cold water cools the initial temperature pulse. The single-limb model presented here does not take into account the shallow sub-surface mixing and cannot explain the subsequent decay of temperatures. Therefore our focus is on the initial response of the system only.

3.7.1.2 Rapid response of diffused flow temperatures: For MEF, the in-situ data is only available for the diffuse flow vent sites [Johnson et al., 2000]. Diffuse flow vent fluids are derived from the sub-surface mixing of the hot vent fluids and cold seawater circulating through the shallow crust. According to Lowell et al [2013], the heat flux for MEF is nearly equally divided among the focused and diffused flow, and the rising hot fluid constitutes $\approx$ 8% of the total diffused discharge. If there is no change in permeability and temperature distribution in the extrusives associated with the event, this percentage is unlikely to change; but if Q increases as a result of change in permeability deeper in the system, then the amount of hot fluid in the diffuse flow may also increase. Additionally, Lowell et al. [2013] argue that the diffuse flow fluids at MEF undergo conductive cooling before they emerge on the seafloor. This would create boundary layer conditions similar to that in our model for the focused flow. Therefore, although we model only hot hydrothermal fluids, the model can be used to explain rapid changes in diffuse flow temperatures if the necessary data are available.

Using the thermal energy balance in Lowell et al. [2013] and using an increased value of Q $\approx$ 264 kg/s, resulting from a doubling of k as obtained from our models, the temperature of the diffused flow increases by 5-6 ^{0}C. The 10^0C increase in diffused flow temperatures recorded by Johnson et al. [2000] suggests that Q may have increased to $\sim$ 288 kg/s, which indicates that the permeability may have increased $\sim$ 3 times in the vicinity of the dike.

3.7.2 Single phase modeling

For the models presented here, the density of the fluid is calculated by assuming that the density of the fluid varies linearly with the temperature of the fluid. The mass balance equation considers this density as the bulk density of the fluid in the model. Although this simplifying assumption does not hold in the deep discharge zone where phase separation is known to occur [Butterfield et al., 1994; Von Damm, 2004], it does not change the nature of the behavior of the hydrothermal system to perturbations. This can be better understood by looking at the expression for Darcys Law.

$$v = -\frac{k(T)}{\eta(T)}\left[\frac{\partial P}{\partial s} - \rho_w(T)g\right] \tag{3.1}$$

Where v = Darcy flow velocity, k = permeability, T = temperature, η = viscosity, P = pressure, s = curvilinear coordinate, ρ = density of the fluid, and g = acceleration due to gravity.

Suppose that in the steady state, circulation is already established in the hydrothermal system with phase-separated fluid. Any temperature change deep in the system is a result of heat added to the system from the dike or change in permeability or heat extraction from the axial magma chamber. As additional heat is taken up by the hydrothermal fluid, on the time scale of conductive cooling of the dike, the buoyancy of the fluids will gradually increase by decreasing the $\rho(T)g$ term in the equation above. This effect is analogous to increasing the dike width was the temperature, and hence buoyancy, of the deep discharge fluid increases with increasing w. As the buoyancy term changes gradually, the velocity and the resultant mass flow rate increases gradually and by a small amount. This does not cause a sudden response on the surface (Figure 7). Additionally, the phase separated region in a hydrothermal system is only ~ 10 cm thick [Lewis and Lowell, 2009] and therefore we neglect it in this model.

3.7.3 Rapid Response of Hydrothermal Systems to Perturbations

The rapid response of hydrothermal systems to perturbations obtained here does not indicate that the fluid has travelled to the surface from deep within the system in a matter of days but that deep perturbations in the system can cause shallow disturbances in the boundary layer, which are observed on the surface shortly after the event. The shallow disturbances can be attributed to the presence of the thermal boundary layer close to the surface. However, it is not only the rapidity of the response that we are interested in, the nature of this rapid response is closely dependent on the nature of the event itself.

Even when deep perturbations to a hydrothermal system are not accompanied by an increase in permeability, the temperature on the surface and Q increase within a matter of

days (Figures 6-9). However, the magnitude of this change is only a few degrees (∼1-2^{0}C). Larger changes may require a longer time (∼ months) to show on the surface. This does not match the observations at the two vent fields in question where not only was the perturbation response rapid, but it was also expressed as a 'spike' or rapid increase in temperature. Such sudden changes are observed when diking is accompanied by a sudden increase in k (Figures 10-17), which causes the fluid velocity to 'jump' to a higher value. While the increase in temperature in our models seems instantaneous, during the seismic event at any vent field, the increase in permeability may also occur over a period of time, in which case it may take longer for the system to achieve its higher temperature.

In general, Figures 6-17 show that the nature of response of Q is reflected in the response of the surface temperature to the perturbation. From a mathematical standpoint, this is understandable because the boundary layer is sensitive to the velocity (or Q) of the venting fluid. From a physical standpoint, the mass flow rate Q is a cumulative expression of the heat supply to the system and its geometrical configuration. This again, can be understood by looking at the expression for Darcy's Law (equation 1). As additional heat is gradually picked up by the hydrothermal fluid, an increase in 'w' or 'h' results in a gradual change in the buoyancy of the fluids, or in other words, the $\frac{\partial P}{\partial s} - \rho_w(T)g$ term in the equation. However, when diking is accompanied by an increase in k, the response in fluid velocity is rapid due to its direct relationship with k as well as a gradual increase in the buoyancy term. This change in velocity leads to a rapid change in Q. In the event of an actual diking, the resultant response on the surface will be some combination of the geometric details and placing of the dike, as well as the conditions under which the hydrothermal fluid cools. In the absence of dike emplacement, increase in k association with earthquakes will still cause a rapid response on the surface which will result in a drop in the temperature of the system eventually.

Therefore, the presence of a thermal boundary layer close the surface can enable the system to show a rapid response to a deep-seated disturbance; however, it is the rapid increase in the permeability of the system that results in a spike in discharge temperature in hydrothermal systems.

3.8 Conclusion

The models for EPR 9^{0}50' N and MEF use reasonable values of vent-field permeability and flow rates to map the "vent-field"-scale response of a hydrothermal system to non-eruptive events. We conclude that steep gradients in temperature close to the surface allow for quick perturbations to hydrothermal systems. When these perturbations are accompanied by increase in permeability due to release of seismic energy, the response on the surface is sudden and sharp in nature. As hotter fluids lie close to the surface, the increase in the velocity of the fluid (and hence the mass flow rate) causes these hotter fluids to erupt rapidly, therefore showing a rapid temperature increase on the surface. We find this to be

true for both EPR $9^0$50' N and MEF.

We note that the model presented here does not include the subsequent decay in temperatures as were observed at both EPR $9^0$50' N and MEF. For this characteristic we defer to Ramondenc et al. [2008] and Germanovich et al. [2011] who argue that the temperature increase close to the surface drives cold fluid into the system via the shallow recharge. This cold recharge "regulates" the temperature at hydrothermal vent fields and cause the subsequent decay in the temperature spike observed. Additionally, permanent changes to a hydrothermal regime, such as decay in magma supply or continuous replenishment, are expressed on the surface over longer time periods.

Table 3.1: Table of Symbols

Symbol	Definition	Value (MEF)	Value (EPR)	Value (Generic)	unit
a^*	effective thermal diffusivity	$\sim 10^{-6}$	$\sim 10^{-6}$	$\sim 10^{-6}$	m^2/s
a_r	thermal diffusivity of rock	$\sim 10^{-6}$	$\sim 10^{-6}$	$\sim 10^{-6}$	m^2/s
$A1$	cross-sectional area of horizontal limb	5 x 10^4	10^4	5 x 10^4	m^2
$A2$	cross-sectional area of horizontal limb	5 x 10^4	10^4	5 x 10^4	m^2
b	length of vent field along strike	600	10^3	-	m
c_f	specific heat of water	5 x 10^3	5 x 10^3	5 x 10^3	J/kg^0C
c_r	specific heat of rock	10^3	10^3	10^3	J/kg^0C
d	basal thermal boundary layer thickness	6	12	12	m
g	acceleration due to gravity	9.8	9.8	9.8	m/s^2
H	length of the upflow zone	2000	2000	2000	m
h_d	height of dike emplacement	250-1500	600	600	m
k	permeability (initial)	0.5x10^{-13}	5x10^{-13}	5x10^{-13}	m^2
L	length of the horizontal limb	10^3	10^3	10^3	m
L_m	latent heat of crystallization	4x10^5	4x10^5	4x10^5	J/kg
l	length scale for mixing				m
P	pressure				bars
P_0	pressure at seafloor	220	250	250	bars
P_H	pressure at depth H below seafloor				
Q	mass flux				
q_d	heat source density/ time/volume				
q_m	basal heat flux				
q_w	lateral heat transfer density/ time/ volume				
r_i	resistance in the i^th limb				
s	curvilinear distance along flow path				
t	time				
t_c	time of dike crystallization				
T	temperature in the upflow zone				
T_{in}	initial temperature distribution				
T_{rech}	recharge temperature	0	0	0	^0C

Table 3.2: Table of Symbols

Symbol	Definition	Value (MEF)	Value (EPR)	Value (Generic)	unit
ν	Darcian flow velocity				m/s
w	dike width	2-20	1	1	m
w_u	width of the upflow zone				m
z	depth				m
α_r	linear thermal expansion coefficient of rock	$2x10^{-5}$	$2x10^{-5}$	$2x10^{-5}$	$/^0C$
α_f	coefficient of thermal expansion of water	10^{-3}	10^{-3}	10^{-3}	$/^0C$
ϕ_0	initial porosity of the upflow zone	10 %	10 %	10 %	
γ	ratio α_r/ϕ_0				
η	dynamic viscosity of water				
ν	kinematic viscosity of water				
λ_r	coefficient of thermal conductivity of rock	2.5	2.5	2.5	$W/(m^0C)$
ρ_f	density of water				kg/m^3
ρ_r	density of rock	3 x 10^3	3 x 10^3	3 x 10^3	kg/m^3
rho_0	initial density of water at the ocean floor	10^3	10^3	10^3	kg/m^3

Acknowledgments. This work was supported in part by NSF Grant OCE 0926418 to RPL.

3.9 References

Bear, J. (1972), Dynamics of Fluids in Porous Media, 764 pp., Elsevier, New York.

Bohnenstiehl, D. R., Dziak, R. P., Tolstoy, M., Fox, C. G., and Fowler M., (2004), Temporal and spatial history of the 19992000 Endeavour Segment seismic series, Juan de Fuca Ridge, Geochem. Geophys. Geosyst., 5, Q09003, doi:10.1029/2004GC000735.

Butterfield, D.A., R.E. McDuff, M. J. Mottl, M. D. Lilley, J. E. Lupton, and G. J. Massoth, (1994), Gradients in the composition of hydrothermal fluids from the Endeavour segment vent field: Phase separation and brine loss , J. Geophys. Res, 99, 9561-9583.

Carslaw, H.S., and Jaeger, J.C., (1959), Conduction of Heat in Solids, 2nd ed., 510 pp., Clarendon, Oxford, U.K. Choi, J. and R.P. Lowell (2014), Numerical models of phase separation in seafloor hydrothermal systems linked to heat flux from a convecting replenished magma chamber. (this issue)

Craft, K.L., R.P. Lowell, and L. Germanovich (2014), Is sudden permeability change from dike emplacement the cause of flood outbursts at Athabascs Valles, Mars? 45st Lunar and Planetary Science Conference, The Woodlands, TX March 17-21, Abstr. 2915.

Davis, E. E., K. Wang, R. E. Thomson, K. Becker, and J. F. Cassidy (2001), An episode of seafloor spreading and associated plate deformation inferred from crustal fluid pressure transients, J. Geophys. Res., 106(B10), 2195321963, doi:10.1029/2000JB000040.

Delaney, J.R., Kelley, D.S., Lilley, M.D., Butterfield, D.A., Baross, J.A., Wilcock, W.S.D., Embley, R.W., and Summit, M., The quantum event of oceanic crustal accretion: Impacts of diking at mid-ocean ridges, Science, 281, 222-230, doi:10.1126/science.281.5374.222

Fornari, D. J., Shank T., Von Damm, K. L., Gregg, T. K. P., Lilley, M., Levai, G., Bray, A., Laymon, R. M., Perfit, M. R., and Lutz, R., (1998), Time-series temperature measurements at high-temperature hydrothermal vents, East Pacific Rise 94951N: Evidence for monitoring a crustal cracking event, Earth Planet. Sci. Lett., 160, 419431.

Fornari, D.J., K.L. Von Damm, J.G. Bryce, J.P. Cowen, V. Ferrini, A. Fundis, M.D. Lilley, G.W. Luther III, L.S. Mullineaux, M.R. Perfit, M.F. Meana-Prado, K.H. Rubin, W.E. Seyfried Jr., T.M. Shank, S.A. Soule, M. Tolstoy, and S.M. White. 2012. The East Pacific Rise between 9N and 10N: Twenty-five years of integrated, multidisciplinary oceanic spreading center studies. Oceanography 25(1):1843, http://dx.doi.org/10.5670/oceanog.2012.02.

Germanovich, L. N., Lowell, R. P., and Astakhov, D. K., (2001), Temperature-dependent permeability and bifurcations in hydrothermal flow, J. Geophys. Res., 106(B1), 473495, doi:10.1029/2000JB900293.

Germanovich, L. N., Lowell, R. P., and Ramondenc, P., (2011), Magmatic origin of hydrothermal response to earthquake swarms: Constraints from heat flow and geochemical data, J. Geophys. Res., 116, B05103, doi:10.1029/2009JB006588.

Johnson, H. P., M. Hutnak, R. P. Dziak, C. G. Fox, I. Urcuyo, J. P. Cowen, J. Nabelek, and C. Fisher (2000), Earthquake-induced changes in a hydrothermal system on the Juan de Fuca mid-ocean ridge, Nature, 407, 174177.

Kelley, D.S., S.M. Carbotte, D.W. Caress, D.A. Clague, J.R. Delaney, J.B. Gill, H. Hadaway, J.F. Holden, E.E.E. Hooft, J.P. Kellogg, M.D. Lilley, M. Stoermer, D. Toomey, R. Weekly, and W.S.D. Wilcock. 2012. Endeavour Segment of the Juan de Fuca Ridge: One of the most remarkable places on Earth. Oceanography 25(1):4461, http://dx.doi.org/10.5670/oceanog.2012.03. Lilley, M. D., D. A. Butterfield, J. E. Lupton, and E. J. Olson (2003), Magmatic events can produce rapid changes in hydrothermal vent chemistry, Nature, 422, 878881, doi:10.1038/nature01569.

Lowell, R.P., and D.K. Burnell (1991), Mathematical modeling of conductive heat transfer from a freezing, convecting magma chamber to a single pass hydrothermal system: Implications for seafloor black smokers, Earth and Planet. Sci., 104, 59 69. Lowell, R. P., and L. N. Germanovich (1994), On the temporal evolution of hightemperature hydrothermal systems at ocean ridge crests, J. Geophys. Res., 99, 565575, doi:10.1029/93JB02568.

Lowell, R. P., and L. N. Germanovich (2004), Hydrothermal processes at midocean ridges: Results from scale analysis and singlepass models, in MidOcean Ridges: Hydrothermal Interactions Between the Lithosphere and Oceans, Geophys. Monogr. Ser., vol. 148, edited

by C. R. German et al., pp. 219244, AGU, Washington, D. C.

Lowell, R. P., A. Farough, J. Hoover, and K. Cummings (2013), Characteristics of magma-driven hydrothermal systems at oceanic spreading centers, Geochem. Geophys. Geosyst., 14, 17561770, doi:10.1002/ggge.20109. Ramondenc, P., L. N. Germanovich, and R. P. Lowell (2006a), Effect of magma degassing on diking processes at midocean ridges, Eos Trans. AGU, 87(52), Fall Meet. Suppl., Abstract B31B1103.

Ramondenc, P., L.N. Germanovich and R. P. Lowell (2008), Modeling the hydrothermal response to earthquakes with application to the 1995 event at 950N, East Pacific Rise, in Magma to Microbe: Modeling Hydrothermal Processes at Oceanic Spreading Centers, Geophys. Monogr. Ser., vol. 178, edited by R.P. Lowel et al., pp. 97-122, AGU, Washington, D.C. Singh, S., R. P.Lowell, and K. C. Lewis (2013), Numerical modeling of phase separation at Main Endeavour Field, Juan de Fuca Ridge. Geochem. Geophys. Geosyst., 14, 40214034, doi:10.1002/ggge.20249.

Sohn, R. A., D. J. Fornari, K. L. Von Damm, J. A. Hildebrand, and S. C. Webb (1998), Seismic and hydrothermal evidence for a cracking event on the East Pacific Rise crest at 950N, Nature, 396, 159161.

Sohn, R. A., J. A. Hildebrand, and S. C. Webb (1999), A microearthquake survey of the high-temperature vent fields on the volcanically active East Pacific Rise (950N), J. Geophys. Res., 104(B11), 25,36725,377.

Von Damm, K. L. (2004), Evolution of the hydrothermal system at East Pacific Rise 950N: Geochemical evidence for changes in the upper oceanic crust, in Mid Ocean Ridges: Hydrothermal Interactions Between the Lithosphere and Oceans, Geophys. Monogr. Ser., vol. 148, edited by C. R. German et al., pp. 285304, AGU, Washington, D. C.

Wilcock, W.S.D., and McNabb, A., (1996), Estimates of crustal permeability on the Endeavour segment of the Juan de Fuca mid-ocean ridge, Earth Planet. Sci. Lett., 138, 83-91, doi:10.1016/0012-821X(95)00225-2.

Wilcock, W. S. D. (2004), Physical response of mid-ocean ridge hydrothermal systems to local earthquakes, Geochem. Geophys. Geosyst., 5, Q11009, doi:10.1029/2004GC000701.

Chapter 4

A Particle in Cell Algorithm for Tracing Fluid Trajectories in Seafloor Hydrothermal Systems

Abstract

Areas of the seafloor at mid-ocean ridges where hydrothermal vents discharge are easily recognized by the biological, physical, and chemical processes that characterize such sites. Locations where seawater flows into the seafloor to recharge hydrothermal cells within the crustal reservoir are, by contrast, almost invisible. In this paper, we introduce a new method of visualizing fluid flow in the subsurface, namely, the Particle in Cell method. We have developed a kinematic model to work in conjunction with thermodynamic models of hydrothermal systems at mid-ocean ridges. While simple in its concept, the PIC model helps us discern recharge zones for hydrothermal systems. We find that for systems with homogenous permeability, hydrothermal recharge occurs in narrow zones in close vicinity of discharge zone and that fluid recharge extends deep into the system. For systems with higher permeability layer 2A, recharge occurs both at shallow and deep locations in the system. Using the ability of this model to track fluid flow in the subsurface, we are able to estimate the discharge and residence time of fluids.

4.1 Introduction

Hydrothermal systems associated with oceanic spreading centers account for a quarter of Earths total heat ux and one third of the heat ux through the ocean oor [Stein and Stein, 1994; Eldereld and Schultz, 1996]. Circulation of seawater through such systems alters both the crust and the circulating fluid, impacting global geochemical cycles [e.g., Wolery and Sleep, 1976, Kadko et al., 1995; Kump 2008]. The warm vent uids rich in nutrients support a wide variety of unique biological communities [e.g., Kelley et al., 2002, Baross et al., 2004,

Childress and Fischer, 1992]. Thus, a thorough understanding of hydrothermal processes at oceanic spreading centers is needed in order to gain insight into thermal and biogeochemical processes associated with young oceanic crust. In this paper, we introduce a new method for mapping fluid trajectories in the oceanic crust during hydrothermal circulation. The aim is to understand the circulation pattern of hydrothermal fluids in the subsurface and to better constrain recharge paths and residence time of fluids in the crust.

Several numerical schemes are now available for general porous flows and for mid-ocean ridge hydrothermal systems (MORHS) specifically. These schemes are designed to simulate the temporal evolution of MORHS and provide 2-D or 3-D visualization of these systems. These models are often constructed using the traditional Eulerian technique, which solves the mass, momentum and energy conservation equations over a finite number of stationary grid-units (elements/nodes). This method requires one to equate ow structures to the shape of the isotherms formed on the grid/mesh (Figure 4.1). Although this methodology is well-developed, it does not provide information about the movement of fluids within the system and fluid trajectories with time. For example, Figure 4.1(a) shows that the upflow zone can be recognized as the high-temperature discharge zone (red and yellow) and that the colder region surrounding it (blue) constitutes the recharge zone. However, outside of the hot zone, it is difficult to discern the details of the circulation pathways. For the 3-D model depicted in Figure 4.1(b) [Coumou et al., 2008], the white arrows represent the velocity vectors, indicating the direction of fluid flow at a particular time but not providing information about the evolution of fluid trajectories.

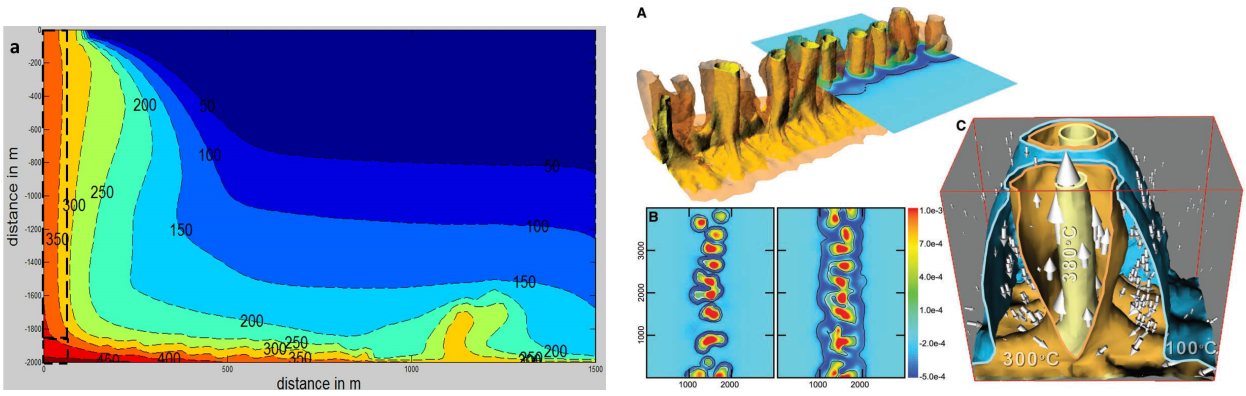

(a) (b)

Figure 4.1: Simulation results depicting hydrothermal plume from (a) 2-D model [Singh et al., 2013] and (b) 3-D model of hydrothermal system at mid-ocean ridges [from Coumou et al., 2008, Reprinted with permission from AAAS].

Another way of modeling uid flow is to use a 'Lagrangian' technique in which, instead of measuring parameter values on fixed grid points, the flow domain is broken down into particles that physically represent the flow material. One such technique is the Particle-in-Cell (PIC) technique [Johnson et al., 1996]. This method combines Eulerian and Lagrangian

methods by treating the fluid system as a continuum while also incorporating a collection of discrete markers to track the flow paths. The thermodynamic properties for the system are obtained from the traditional 'Eulerian' simulation and the movement of particles is obtained from PIC code. Such a hybrid model can provide greater detail for processes such as circulation patterns.

In this paper, we have used MATLAB 2010b [The MathWorks, Inc., Natick, Massachusetts, United States.] to develop a prototype of a PIC model that can be coupled with the numerical results obtained from the 2-D NaCl-H_2O code FISHES [Lewis and Lowell, 2009 a,b] for marine hydrothermal systems. While this work focuses on illuminating path-lines for MORHS, this method can be applied to any existing models of porous flows for obtaining better understanding of fluid trajectories. Knowledge of fluid trajectories can provide us important information such as residence time for fluids, regions of likely mineral deposition, equilibration zones for fluid, and possible sites for tracer injection experiments. In this chapter, we focus on recognizing recharge zones for seafloor hydrothermal systems and estimating residence time of fluids in the subsurface.

4.2 Recharge Zones and Residence Time in MORHS

Areas of the seafloor at mid-ocean ridges where hydrothermal vents discharge are easily recognized by the dramatic biological, physical, and chemical processes that characterize such sites [Kelley et al., 2002]. Locations where seawater flows into the seafloor, and the details of circulation pathways beneath the seafloor are, by contrast, much harder to determine. Over the past years, several studies have employed different techniques to reveal recharge zones for hydrothermal vent systems. Owing to the dip in the magma chamber imaged at Main Endeavour Field (MEF) [Van Ark et al., 2007], Tivey and Johnson [2002] suggested that the east-west thermal gradient dictated the overall fluid flow (and recharge) to occur in the east-west direction, across the axis of the ridge. Tolstoy et al. [2008] used ocean bottom seismometer data at East Pacific Rise (EPR) to argue that the across-axis recharge model was not applicable to EPR and that the along axis faults and deep seated seismicity dictated that the recharge be occurring along axis. They also indicated that recharge may be occurring surrounding zones of discharge based on the seismicity pattern. Coumou et al. [2008] used 3-D models for pure water simulations to show that convection cells in MORHS self-organize into pipe-like upflow zones surrounded by narrow zones of focused and relatively warm downflow. This was supported by Johnson et al., [2010] who used heat flow measurements at MEF to identify recharge zones as located within an annular ring of very cold seawater around the large Main Endeavour Hydrothermal Field, with seawater inflow occurring within faults that surround the fluid discharge sites. Singh et al., [2013] used 2-D numerical models of MEF to argue that venting occurs with relatively little mixing between the rising plume and seawater. This supported the idea of deep seated recharge as proposed in Johnson et al., [2010].

In spite of the above-mentioned efforts, our knowledge of recharge zones remains limited.

While Tivey and Johnson [2002] and Johnson et al., [2010] support the idea of cylindrical pipe-like flow, with recharge and discharge occurring in vicinity of each other, these studies do not fully address the depth of the recharge zones or circulation pathways in the subsurface. Coumou et al., [2008] equate upwelling plumes to isotherms and use fluid velocity vectors in one snapshot of the simulation to depict fluid motion, thereby not providing any information on the trajectory of fluids. Tolstoy et al. [2008] state that their study is specific to EPR and do not comment on a general pattern of subsurface fluid flow or provide any constraints on fluid pathways.

Due to the limited knowledge of subsurface circulation, the estimation of residence time for fluids in the subsurface is also subject to debate. The estimated values vary from several years to a few hours depending upon the method. Foustoukos et al., [2009] used chemical disequilibrium data to show that for shallow circulation, the residence time of fluid may be as small as 10 hours. Based on the response of hydrothermal systems to diking events, Fornari et al., [1998], Sohn et al., [1998], Johnson et al., [2000] estimate the characteristic residence time of the fluid to be $\sim$ 7- 10 days. This idea was challenged by Ramondenc et al.,[2008], Germanovich et al., [2011] and Singh and Lowell [2015] who argued that the rapid response of hydrothermal systems occurs close to the surface and that using realistic values of heat flow and permeability estimates [Lowell et al., 2013], the residence time of fluids should be several weeks if not months. This idea was also proposed by Kadko and Moore [1987] who used radiochemical constraints to estimate fluid residence time to be $\approx$ 3 years.

The distinct advantage of the model developed here is that it helps to visualize fluid trajectories. With this information, one can estimate the residence time for a particular flow path, study permeability-based fluid trajectories, interpret the pressure-temperature regions in which fluid resides, and estimate the locations of mineral deposition. In this paper, we focus on delineating regions of fluid downflow and visualizing subsurface fluid pathlines. We will then estimate residence times for different hydrothermal scenarios. In subsequent work, we plan to study anhydrite precipitation zones in the subsurface and how it affects local permeability. This model can also shed light on the circulation, motility and availability of nutrients for subsurface microbial communities present at MORHS. We believe that this model provides a new perspective to fluid motion in the oceanic crust.

4.3 The Particle in Cell Method

4.3.1 Introduction

The PIC method was developed at the Los Alamos National Laboratory in the late 1950's to solve complex computational fluid dynamic problems including reactive flows, multi-material flows, multi-phase flows, and flows with spatial discontinuities [Johnson, 1996]. The motivation was to invent a new approach that could effectively avoid the disadvantages of traditional mesh-based methods [Harlow, 1957; Evans and Harlow, 1957] where Lagrangian particles are used to carry material mass, position and other information on a uniform Eu-

lerian mesh. Due to its advantages, it has been extensively applied to free-surface flows and magneto-hydrodynamic problems such as plasma modeling.

The motivation for introducing this method for modeling hydrothermal systems is to introduce a new technique to monitor and understand the motion of fluids in the subsurface. This method has not yet been adopted to study hydrothermal fluids or fluid flow in porous media. In essence, this technique is similar to the classical method of calculating pathlines for fluid movement as described by Norton [1978] but is significantly advanced. With the available computational ability and better estimates of fluid properties, we have improved numerical codes that can model hydrothermal systems with greater speed and accuracy. Additionally, we can visualize several particles at the same time for multiple stages in the simulation, and can therefore draw inferences about field-scale fluid circulation patterns far more effectively.

The model presented in this paper is modified from the standard PIC technique in which the mass of the fluid is divided among the particles. The standard approach is difficult to implement for hydrothermal fluids because they vary greatly in density over the range of temperatures and pressures encountered at MORHS. We therefore solve the dynamics of the model is using the numerical code FISHES, and the kinematic part is solved with the PIC code. Both parts of the model are briefly explained in the next section. The details of the numerical code FISHES can be obtained from Lewis and Lowell [2009 a,b] and the PIC model is provided as appendix to this paper. The PIC model can be applied to other existing software for hydrothermal modeling or computational fluid modeling. The model for this paper is developed for 2-D flows but can easily be expanded to work with a reliable 3-D code. The 'particles' in this work are to be considered tracers or weightless GPS trackers attached to the fluids and therefore for the rest of the paper, we use the terms particles and fluids interchangeably.

4.3.2 Algorithm

Fully Implicit Seaoor Hydrothermal Event Simulator or FISHES is a numerical scheme capable of simulating two-phase flow in a permeable medium containing a NaCl-H_2O fluid [Lewis and Lowell, 2009a, 2009b]. It provides solutions to the conservation equations governing fluid ow together with an equation of state that calculates thermodynamic properties of the fluid as functions of temperature, pressure and salinity at each time step. Using the values of temperature, pressure, salinity, density, viscosity and permeability, velocity is computed at each time-step. The velocity for each cell in both x- and y-directions (u and v, respectively) are read from FISHES at fixed time intervals (Δt) and these values of u, v and Δt form the input to the PIC model. The initial set up in FISHES is allowed to run for $\sim$ 100 years for the simulation to achieve quasi-steady state. The values of u, v and Δt are exported after this time to the PIC code.

The PIC code is developed in MATLAB [2010b] using the 'interpn' functionality on the discrete velocity values to obtain a piece-wise continuous velocity function (U_f and V_f) for

both u and v for the entire domain. After this step, u and v are known for all locations in the model. Particles are then initiated in the system as an array of coordinates at the desired location. For each time step, U_f and V_f are used to calculate the velocity for each particle. The particles are then translated in space using the simple relationship

$$\vec{x} = \vec{u} \times \Delta t \tag{4.1}$$

$$\vec{y} = \vec{v} \times \Delta t \tag{4.2}$$

At this point, u and v values are obtained for the next time interval and the above stated steps are repeated. The algorithm is roughly summarized in Figure 4.2 where the dotted box represents the PIC algorithm. This algorithm generates animations of particle motion in the domain. For the sake of reproduction in this paper, the output in Figures 4.4 - 4.11 is presented as snapshots in time. The animations of the results can be obtained by running the codes provided in the appendix.

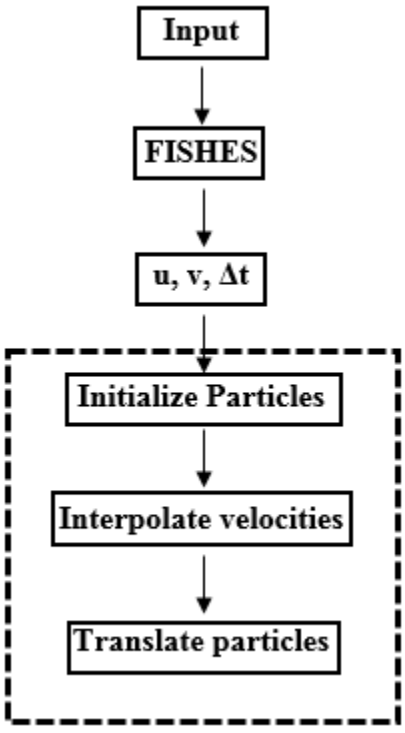

Figure 4.2: Schematic flowchart of algorithm adopted in the paper. The dashed box represents the iterative part of PIC model.

4.4 Model Setup

For this study, we construct general models with parameters that are representative of those observed at MORHS. The physical parameters that are described in this section represent the setup of the model in FISHES. Same geometrical setup is used in the PIC models.

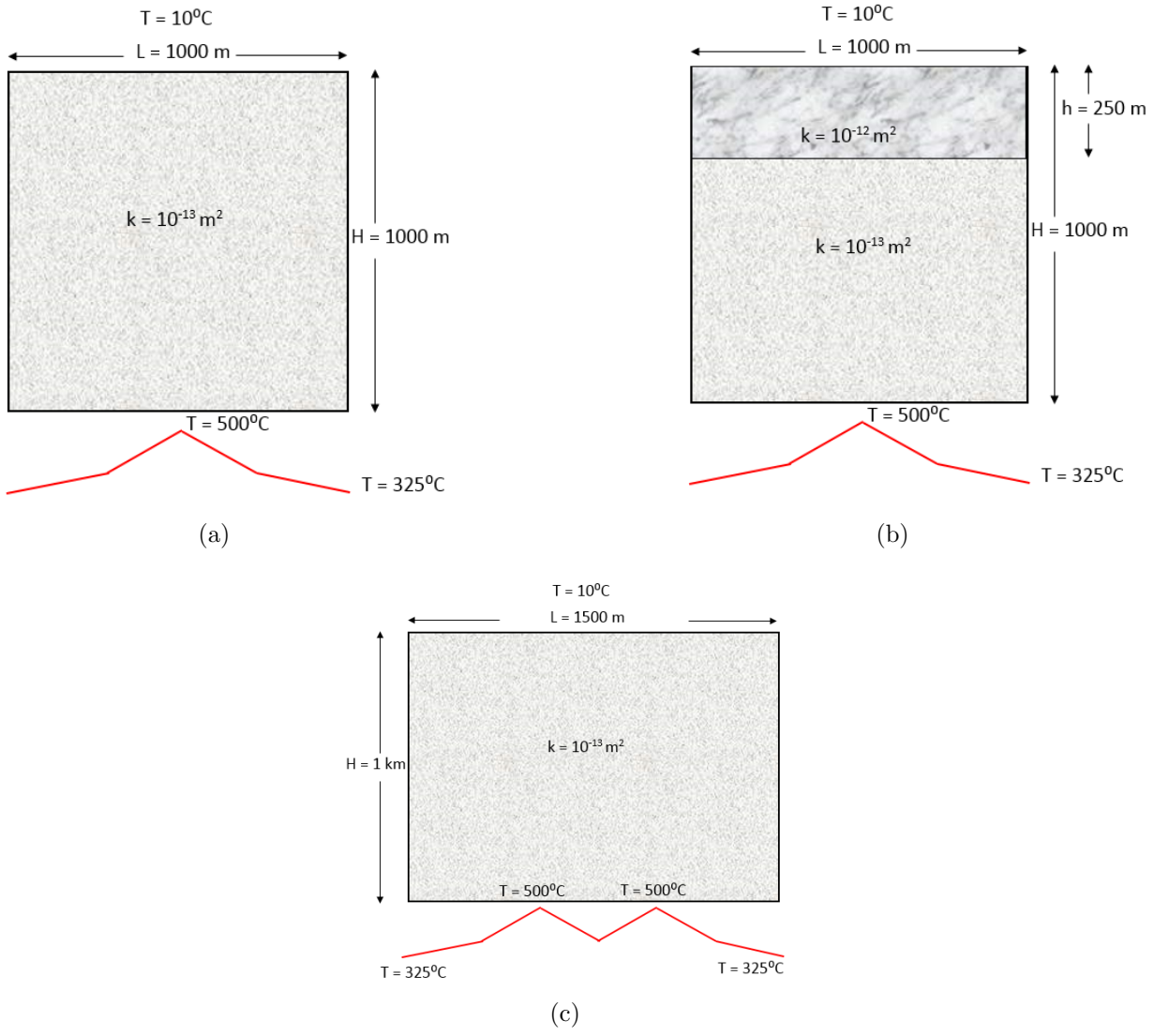

Figure 4.3: Schematic representation of the geometrical setup of the models for (a) across-axis model with homogenous permeability, (b) across-axis model with heterogeneous permeability (c) along-axis model

The across-axis models (Figure 4.3a and 4.3b) are assigned a depth of 1 km beneath the seafloor and a width of 1 km. Side walls of the system are impermeable and insulated.

The top boundary of the system is permeable and maintained at constant seaoor pressure of 25 MPa, corresponding to the depth of 2500 m. The bottom boundary of the system is impermeable and maintained at a constant temperature. The center of the bottom boundary is hotter than the eastern (right) and western (left) boundaries to simulate the effect of the model being centered over the magma chamber. The highest bottom boundary temperature (BBT) is 500^0C (Figure 4.3c). We consider a maximum BBT of 500^0C to be a reasonable assumption based on Fontaine et al. [2009]. They have used geothermobarometry to infer that, for several mid-ocean ridge hydrothermal systems, the temperature at the bottom of the hydrothermal system lies between 415^0C and 445^0C. Additionally, Jupp and Schultz [2004] argue that that water in hydrothermal convection cells upwells at $\approx 400^0$C when driven by a heat source above$\approx 500^0$C. Temperature at the seaoor is set to 10^0C and initially increases linearly from top to bottom of the system. The initial pressure distribution is hydrostatic and salinity is set to 3.2 wt % everywhere. Two permeability (k) models were used for the across-axis models: homogenous ($k = 10^{-13}$ m^2) and heterogeneous with layer 2A ($k = 0.5$ x 10^{-13} m^2, Figure 4.3b). The cell size in the models is 25 m x 25 m.

For the along axis models (Figure 4.3c), the depth of the model remains 1 km and the width is 1.5 km. The central zone is the hottest and is 0.5 km long simulating an axial magma chamber. The center of the axial magma chamber is made slightly cooler to obtain two distinct hydrothermal plumes. The boundary conditions and values of parameters at the seafloor remain identical to the across axis models. We use a uniform permeability of 10^{-13} m^2 for these models.

In the sections below, we first show the results to provide a visualization for the models. The results of the uniform permeability across and along axis models are used to interpret the pattern of subsurface fluid flow and are discussed in the section 4.5. Once we display fluid pathways using the PIC model, we discuss residence time of fluids in the oceanic crust. The results for the heterogeneous permeability model are also used in the determination of fluid residence time and are discussed in section 4.6.

4.5 Results

The across axis and along axis models with homogenous permeability are run in FISHES for a total of 200 years, within the first 100 years of which, it attains quasi-steady state (Figure 4.4). After $\sim$ 100 years the isotherms stabilize and this stage is used as a starting point for the PIC simulations. We introduce a few terms in Figure (4.4) that will facilitate easy discussion of the results.

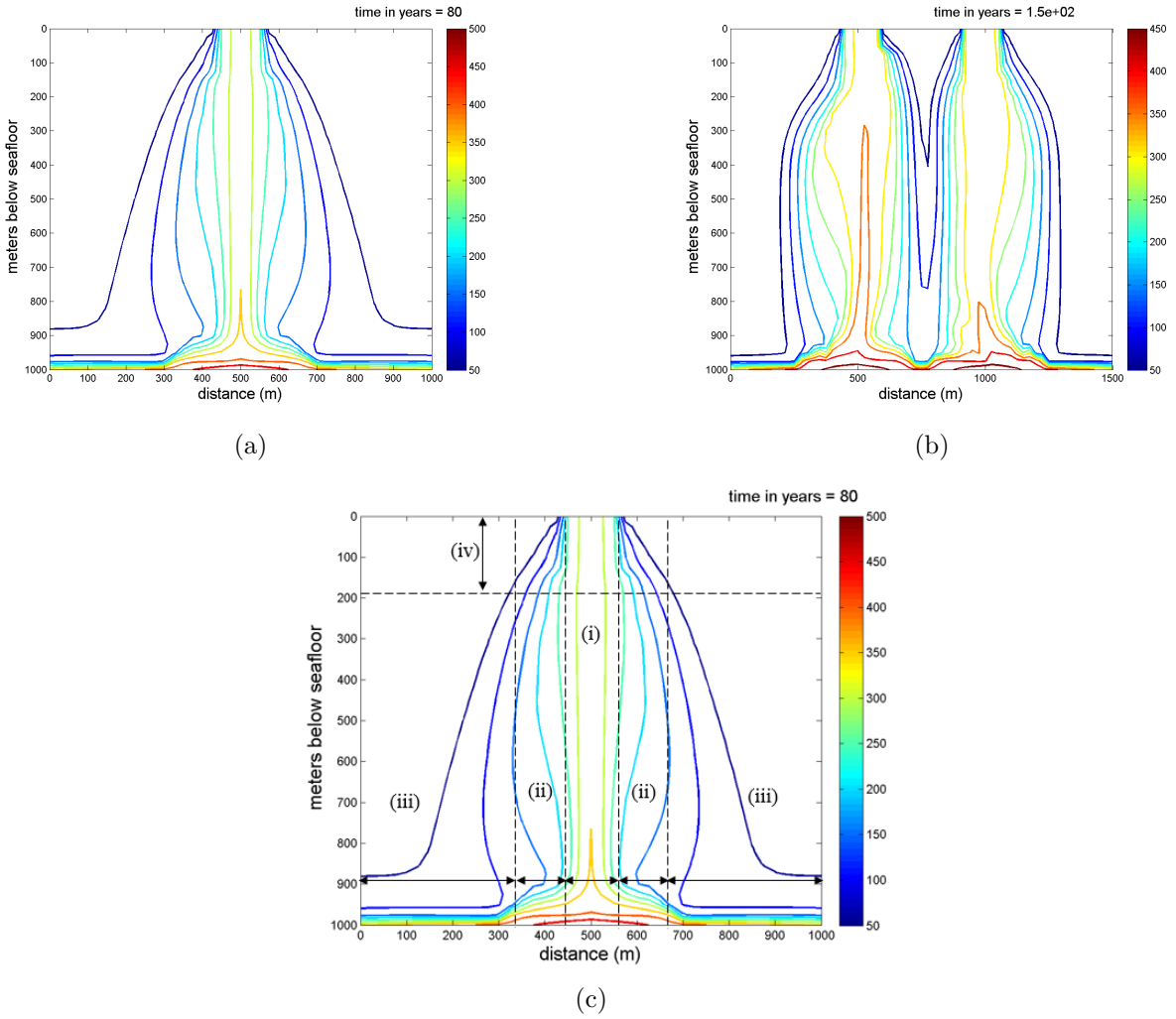

Figure 4.4: Plot of temperature contours for simulation results from FISHES showing the hydrothermal plumes structure for (a) homogeneous permeability across-axis model (b) along axis model. (c) Temperature contours of simulation results where dashed lines mark the zones as discussed in the paper (i) discharge zone (ii) near recharge zone (iii) far recharge zone (iv) top recharge zone.

4.5.1 Recharge Zones

4.5.1.1 Across-axis models

To test the model, we follow the steps outlined in Section 4.4 to obtain results for a uniform particle distribution in the entire domain. In Figure 4.5, fluids in the discharge zone are moving upwards and out of the system and all particles outside of the discharge zone are moving downward towards the bottom of the system. Between the upward and downward

moving fluid streams, there is a narrow transition zone either side of the discharge zone in which fluids move first upward and then downward. In the following sub-sections, we choose specific parts of the domain (Figure 4.4) to observe fluid movement in those regions.

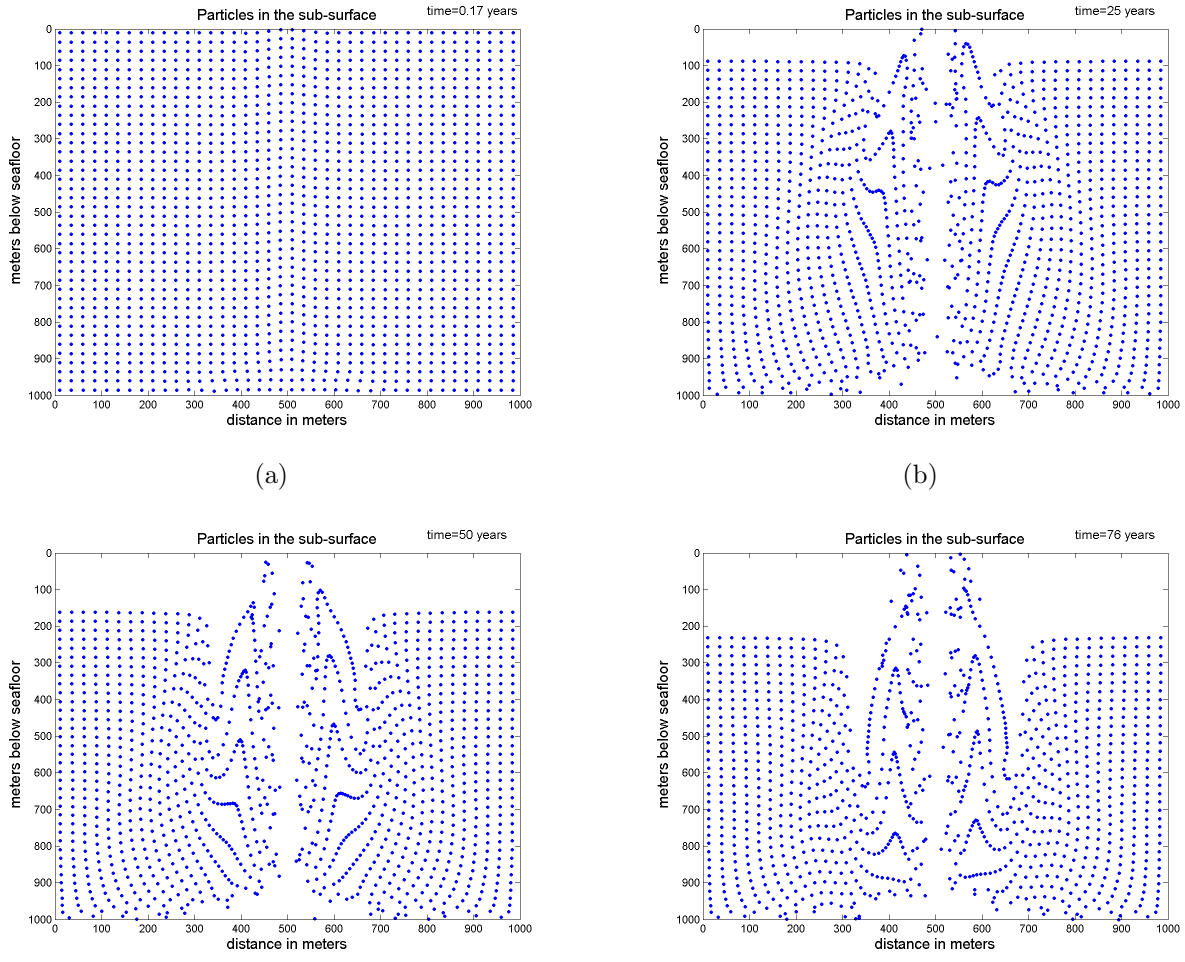

Figure 4.5: Simulation results of the PIC model for across axis model with homogeneous permeability and uniform distribution of particles in the entire domain for different snapshots in time.

4.5.1.2 Top Recharge Zone

An intuitive way of visualizing recharge zones is to look at the fluids that are seeping into the crust from the seafloor. Figure 4.6, depicts the movement of particles from the top recharge zone. After a few years (Figure 4.6c), it is evident that the fluid in the near recharge zone (ii) is traveling faster and deeper into the system. By contrast, the fluid in the far recharge zone (iii) is moving slowly almost maintaining the initial linear profile, indicating

that particles in the far recharge zone are moving with velocities comparable to each other.

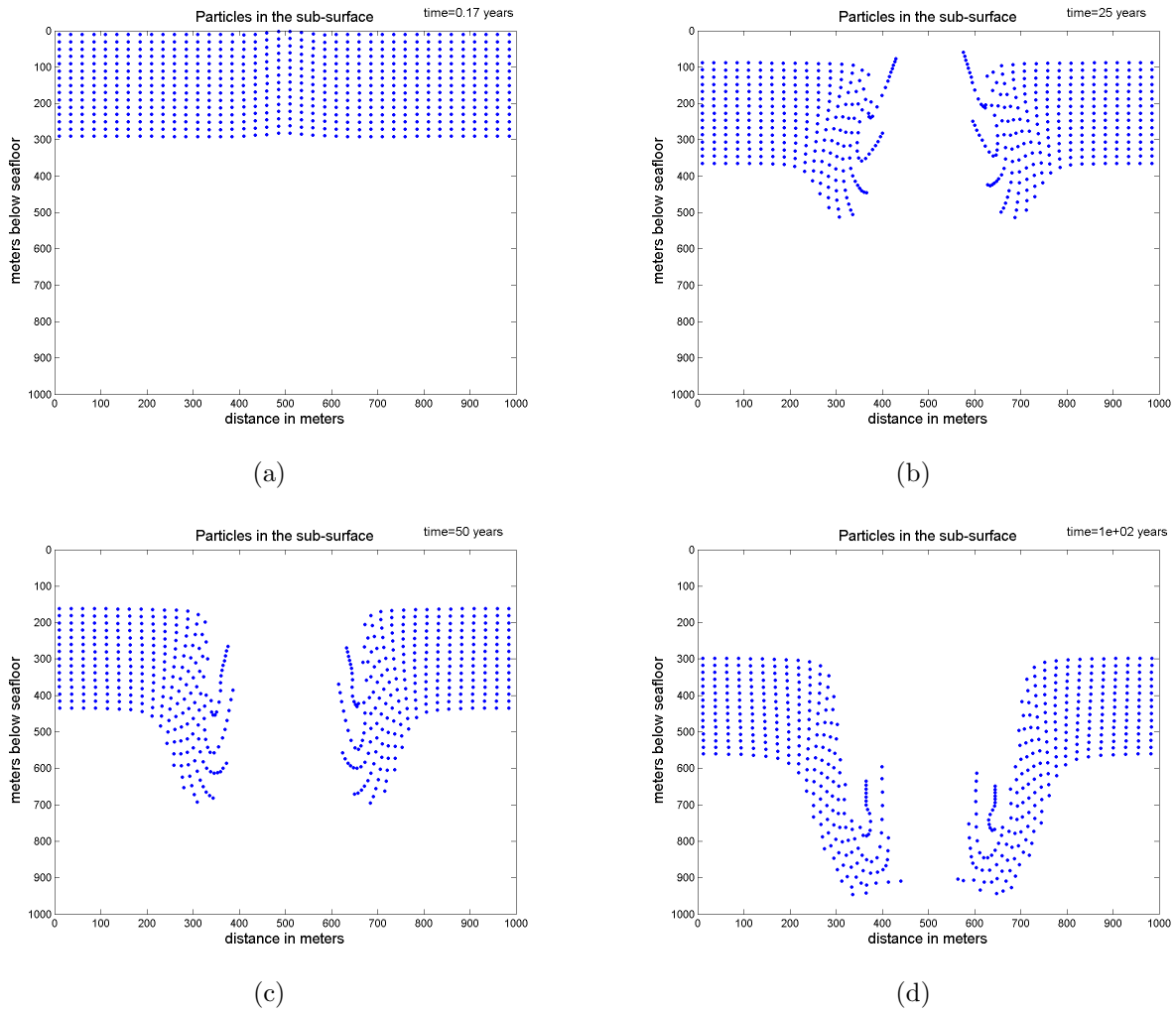

Figure 4.6: Simulation results of the PIC model for across axis model with homogeneous permeability and top recharge zone for different snapshots in time.

In later stages of the simulation (Figure 4.6c and 4.6d) the discharge zone does not contain any particles. This is because the particles travel deep into the system before joining the discharge stream. This indicates that fluid particles that are already deep in the system enter the discharge zone before particles recharging from the surface. It may also be noted that fluids are traveling nearly vertically downward into the system. As the fluids in the near recharge zone are moving faster than the fluids in the rest of the system, we take a close look at near recharge zones next.

4.5.1.3 Near recharge zone

Figure 4.7 shows the particle distribution and movement in the near recharge zones. The fluid discharge stream is now being supplied with particles from the surrounding recharge streams as particles in the near recharge zone travel deep into the system before joining the discharge. These particles do not entrain the discharge zone in the distance between the top and the bottom of the systems. This result indicates that recharge is occurring close to the discharge zone and that the recharge fluids are penetrating deep into the system before being discharged. Although this simulation is 2D, the near vertical movement of fluids observed in Figure 4.7 support previous claims of concentric pipe-like recharge and discharge occurring in close vicinity of each other [Coumou et al., 2008; Johnson et al., 2010].

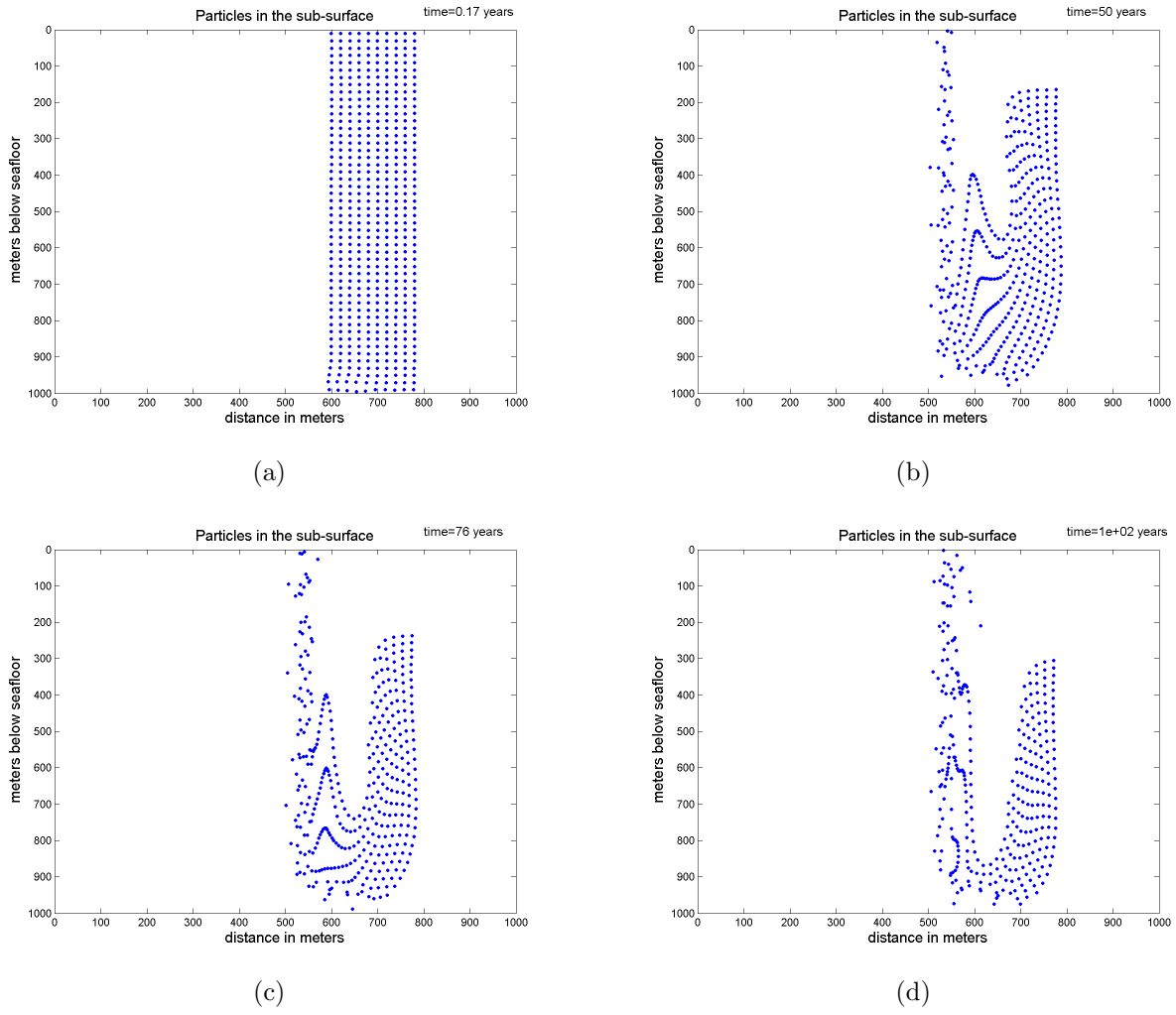

Figure 4.7: Simulation results of the PIC model for across axis model with homogeneous permeability and near recharge zone for different snapshots in time.

4.5.2 Along axis models

In the contour plot of the along-axis model (Figure 4.4a), the cold (50^0C) isotherm extends deep into the system between the hot hydrothermal plumes. This is indicative of cold water recharging deep into the MORHS close to the discharge zones. A PIC model (Figure 4.8) shows patterns of recharge similar to those seen in Section 4.5.1 indicating pipelike recharge and discharge.

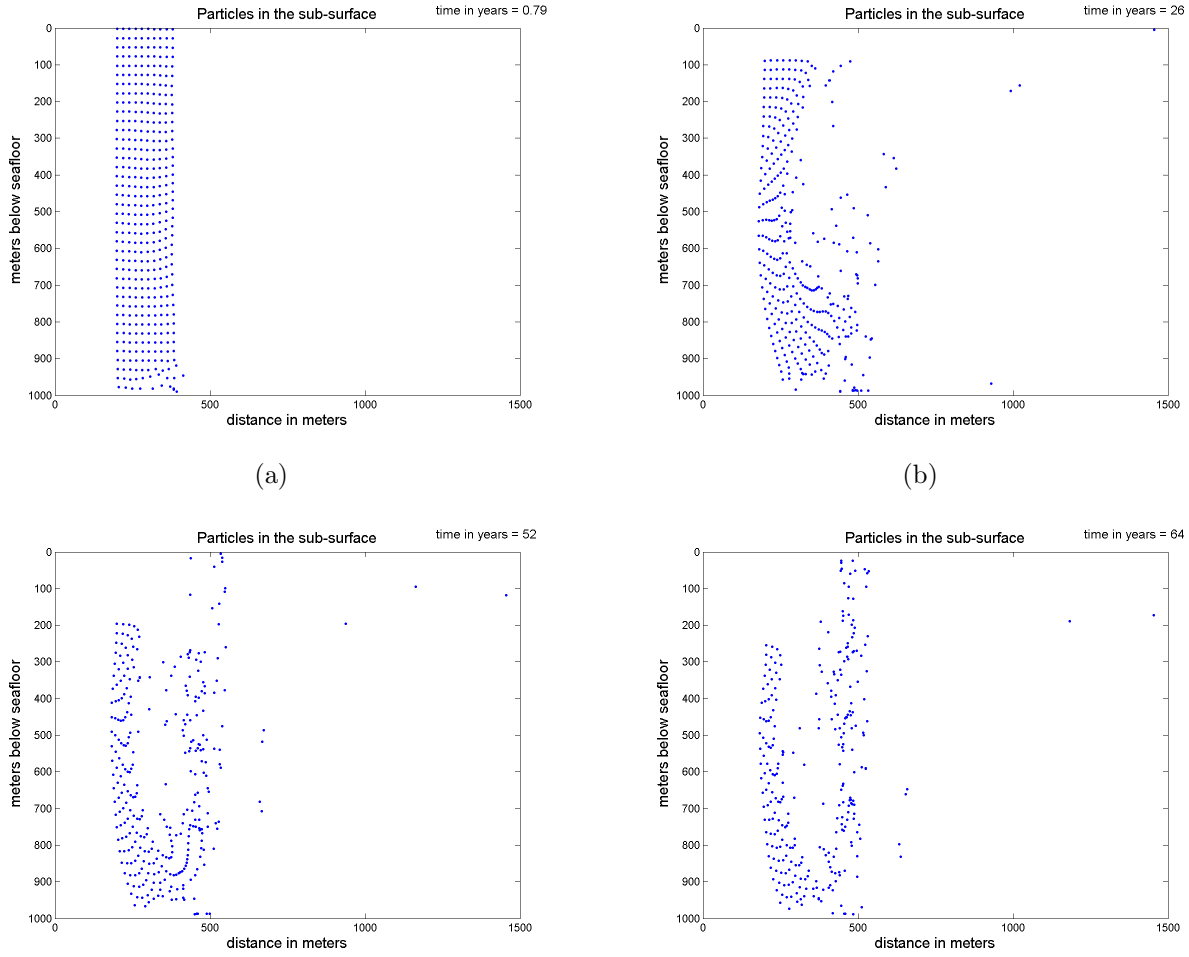

Figure 4.8: Simulation results of the PIC model for along axis model with homogeneous permeability and near recharge zone for different snapshots in time.

4.5.3 Summary: Recharge zones

Results of the PIC model for a generalized 2D hydrothermal system show that recharge occurs close to high temperature discharge in both along and across axis scenarios. For

actual 3-dimensional hydrothermal flow, this would indicate that the recharge and discharge are arranged in narrow column-like structures surrounding the recharge zone. Although this had previously been implied by other studies, no prior study was able to delineate the fluid paths with such clarity. With this better visualization of fluid movement in the crust, we now further the discussion about residence time.

4.6 Residence Time

The discussion of residence time of fluids in the subsurface requires a concrete definition and mathematical formulation of the term. Transit time for fluid can be simply described by the kinematic relationship

$$\mathbf{t = distance/speed}$$

It is important, however, to understand the implied meaning of distance and velocity with regards to residence time. For a few previous studies, the 'residence distance' is described as the distance traveled by the fluid after entering the discharge zone [Kadko and Moore, 1987]. For others [Coumou et al., 2008; Foustoukous, 2009] , the distance travelled by the fluid between entering and leaving the crust is considered. For sake of simplicity, we define two terms, namely, discharge time, which measures the time taken by the fluid to travel from the bottom of the system to the top (red line in Figure 4.9); and residence time, which is the total time a fluid particle spends in the subsurface (blue line in Figure 4.9).

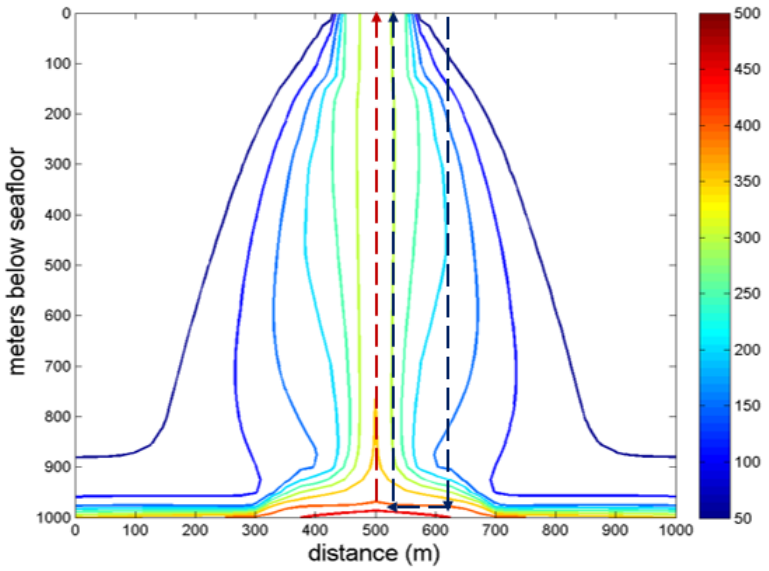

Figure 4.9: Contour plot of the across axis model showing approximate paths for discharge (red dashed line) and residence (blue dashed line) times for the fluid.

Fluid velocity in these simulations is calculated using the Darcy's law for flow in porous media. This Darcy velocity is a volume flow rate/unit area, which has the dimensions of velocity (m/s) and not the pore velocity of the fluid. In porous medium the volume of the solid rock (V_r) and the volume of the space available for fluid flow (V_f) are related by porosity (ϕ), which is a fraction of the volume of voids over the total volume, between 0 and 1, or a percentage between 0 and 100%. Assuming interconnected pore space and saturation, the volume of the fluid in the rock is held entirely in the pore spaces. Therefore, the actual pore velocity of fluid is related to the Darcy velocity by the relationship,

$$\vec{u_p} = \vec{u}/\phi \tag{4.3}$$

Where u_p and v_p are pore velocities and ϕ is the porosity. Porosity in these simulations is fixed at 10 %. Therefore, the pore velocity of fluids is 10 times faster that Darcy velocity. We use this velocity to calculate the discharge and residence times of the fluid, as shown in Figures 4.10 and 4.11. The discharge time for the across axis homogeneous permeability models calculated with the PIC model is $\sim$ 1 year and the residence time is $\sim$18 years.

Coumou et al. [2008] use pore velocities to calculate the residence time of fluid and estimate a time of $\sim$ 3 years for the whole circulation path. The estimates of residence time in this paper are greater than their estimates because, despite considering the non-linear properties of pure water at high temperatures in their model, they double the discharge time for doubled path length to obtain residence time. This, however, is an inaccurate assumption because the high temperature and reduced viscosity of fluids in the discharge zone cause the recharge and discharge times to be different from each other (Figures 4.10 and 4.11). So, even if the path length for residence time is equal to twice of the discharge length, the variation in fluid velocity over the temperature and pressure range for these systems causes the residence time to be much greater than the discharge time.

While the estimates of discharge and residence times presented in this paper are in reasonable agreement with other studies [Kadko and Moore., 1987; Germanovich et al., 2009], we do not obtain a residence time as short as a few days or hours, as calculated by Foustoukos et al. [2009]. One way of explaining smaller residence times would be to either reduce the travel distance of fluid or increase the fluid velocity. The fluid velocity in the subsurface may increase locally due to an increase in permeability. We, therefore, construct a PIC model with a higher permeability layer 2A to observe its effect on fluid path or residence time. For model with layer 2A (Figure 4.12) the particle does not travel all the way to the bottom of the system, but instead joins the discharge plume in the shallow subsurface. Therefore, introducing a higher permeability layer 2A not only increases the velocity of the fluid but also reduces the path length for it . With a permeability difference of only half an order of magnitude, the residence time of the fluid is reduced by an order of magnitude (from $\sim$18 years to 0.5 years). As Figure 4.12 only depicts one particular trajectory, the variability in short residence times is hard to constrain. For local zones of

higher permeability, the combined effect of increased velocity and reduced path length may result in residence time much shorter than obtained here.

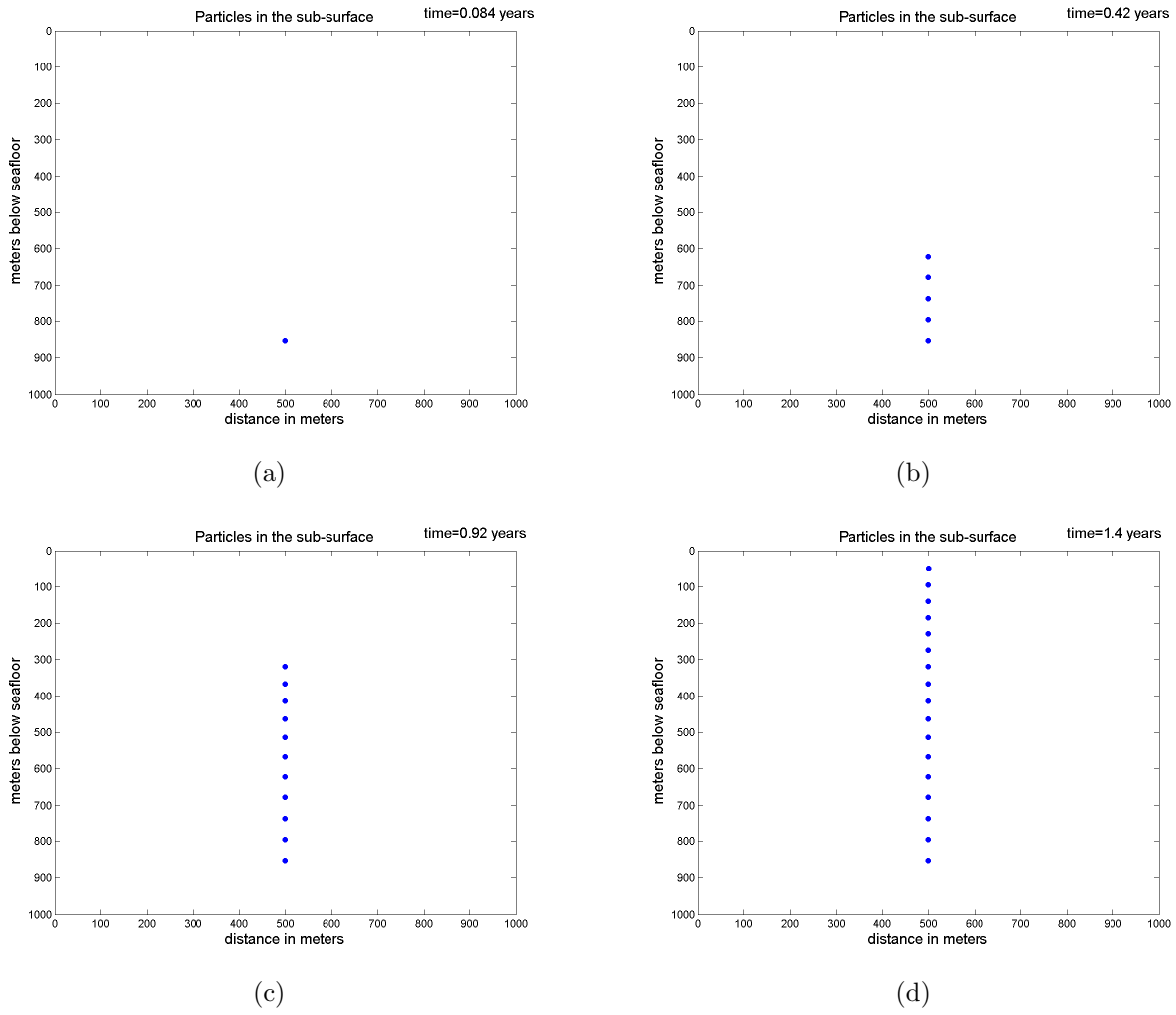

Figure 4.10: Determination of discharge time for across axis model for one particle. The blue dots represent the trajectory taken by the particle.

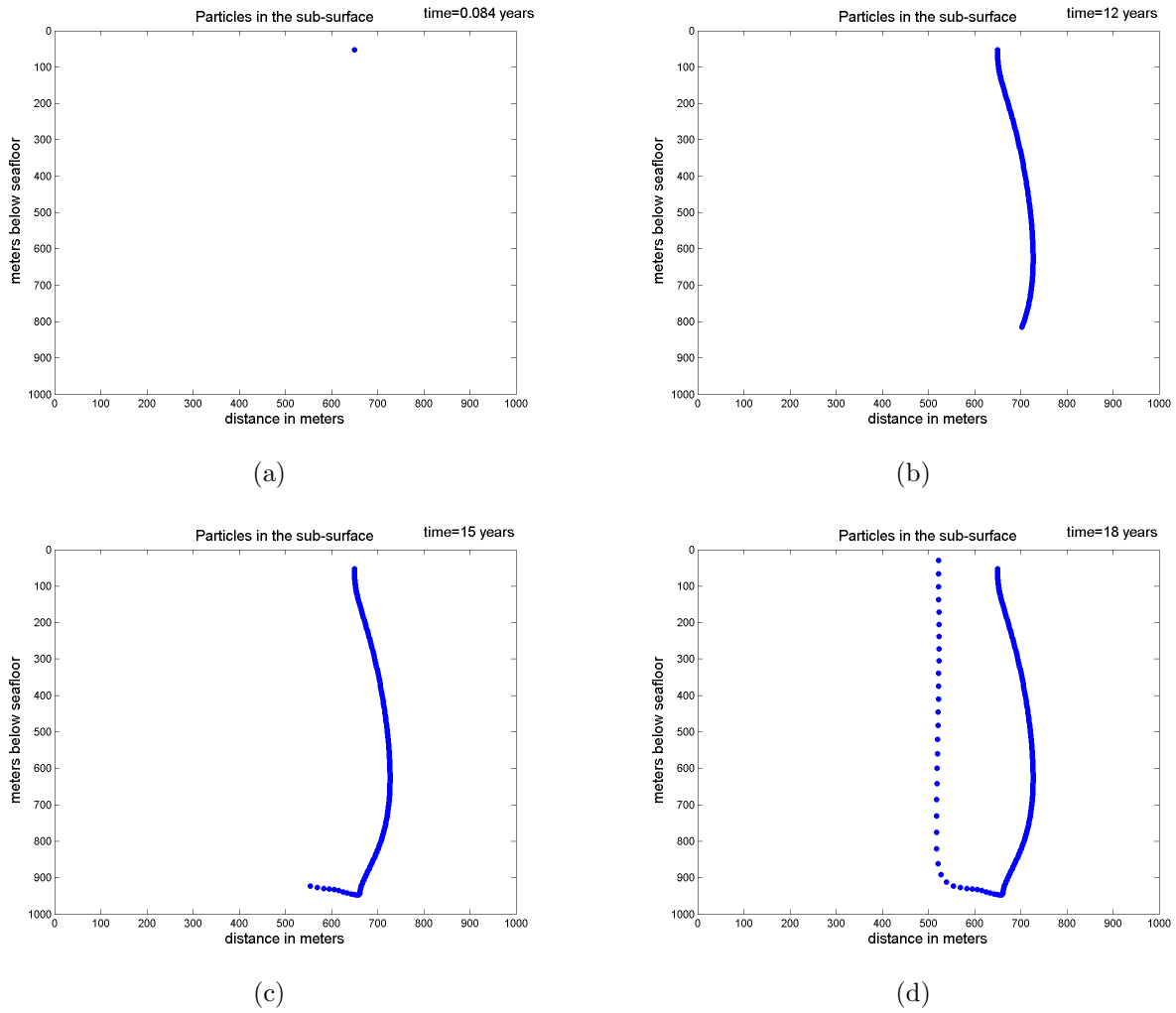

Figure 4.11: Determination of residence time for across axis model for one particle. The blue dots represent the trajectory taken by the particle.

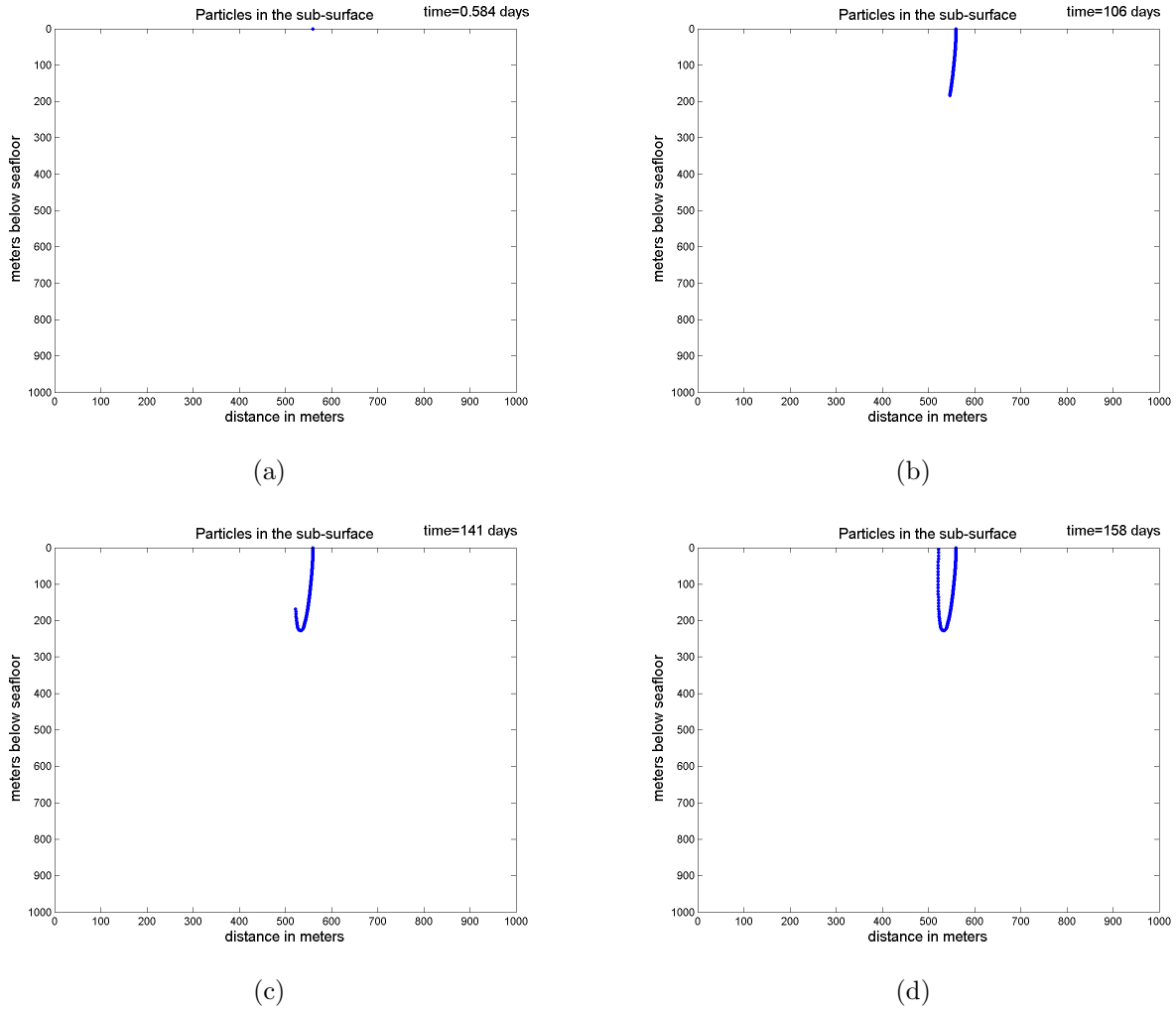

Figure 4.12: Determination of residence time for across axis model with layer 2A for one particle. The blue dots represent the trajectory taken by the particle.

4.7 Discussion

This work is focused on introducing the methodology of PIC modeling and its basic application for delineating fluid trajectories in the subsurface. The model, however, can be developed further for application to other processes at mid-ocean ridges. One particular topic of interest is studying subsurface anhydrite precipitation.

Anhydrite has retrograde solubility in seawater and its solubility decreases sharply in the 150-250^0 C temperature range. This temperature range is frequently reached in the subsurface for MORHS, especially in the region surrounding the discharge zone, and therefore anhydrite precipitation may be a contributing factor to hydrothermal flow. As a result of

precipitation, porosity, and therefore permeability, may decrease altering the trajectory of the fluids. Although traditional models can provide information on temperature zones that are most likely to have mineral precipitation, the PIC model is capable to visualizing fluid movement relative to these zones. In future work, we plan to combine mineral precipitation rates with FISHES and the PIC model. The rate of change of porosity and permeability after anhydrite precipitation can be compared to the residence time of the fluid to draw inferences about the impact of mineral precipitation on fluid circulation.

4.8 Conclusion

We have shown in this work that applying a particle-tracking methodology to study porous flows can help us understand fluid flow patterns. The results of generic along and across axis models tend to substantiate the idea of pipe-like recharge and discharge zones for MORHS. We further this idea by including the effect of homogenous and heterogeneous permeability. For uniform permeability systems after establishment of hydrothermal circulation, we find that fluid recharge extends deep into the system and the fluid particles that start at the surface do not entrain the discharge plume. This gives the discharge time of fluid ~ 1 year and the total residence time of fluids ~ 18 years. The total residence time of the fluid is not simply twice the discharge time because of non-linear velocity of the hydrothermal fluid in the subsurface.

This work is a starting point for other studies. The aim is to combine fluid flow information obtain from the PIC model with mineral precipitation data to understand potential zones of mineral precipitation and subsequent evolution of permeability. This model can also be applied for higher resolution modeling of the shallow subsurface to study the impact of fluid flow on subsurface microbial communities.

4.9 References

Baross, J.A., W.S.D. Wilcock, D.S. Kelley, E.F. DeLong and C. Cary (2004), The Subsurface Biosphere at Mid-Ocean Ridges: Issues and Challenges, The Subseafloor Biosphere at Mid-Ocean Ridges, Volume 144, Pg. 1.

Childress J.J., C.R. Fischer (1992), The biology of hydrothermal vent animals: Physiology, biochemistry and autotrophic symbioses. Oceanogr Mar Biol Annu Rev. 1992;30:337341.

Coumou, D., T. Driesner, P. Weisand, and A. Heinrich (2008), The Structure and Dynamics of Mid-Ocean Ridge Hydrothermal Systems , Science, 321, DOI: 10.1126/science.1159582.

Elderfield, H., and A. Schultz (1996), Mid-Ocean Ridge hydrothermal fluxes and the chemical composition of the ocean, Annu. Rev. Earth Planet. Sci., 24, 191224. Evans, M. W. and F. H. Harlow (1957), "The Particle-in-Cell Method for Hydrodynamic Calculations," Los Alamos Scientific Laboratory report LA-2139.

Fontaine, F. J., W. S. D. Wilcock, D. E. Foustoukos, and D. A. Butterfield (2009), A Si-Cl geothermobarometer for the reaction zone of the high-temperature, basaltic-hosted

mid-ocean ridge hydrothermal systems, Geochem. Geophys. Geosyst., 10, Q05009, doi:10.1029/2009GC002407.

Fornari, D. J., Shank T., Von Damm, K. L., Gregg, T. K. P., Lilley, M., Levai, G., Bray, A., Laymon, R. M., Perfit, M. R., and Lutz, R., (1998), Time-series temperature measurements at high-temperature hydrothermal vents, East Pacific Rise 94951N: Evidence for monitoring a crustal cracking event, Earth Planet. Sci. Lett., 160, 419431.

Foustoukos, I. D., N. J. Pester, K. Ding, and W. E. Seyfried Jr. (2009), Dissolved carbon species in associated diffuse and focused flow hydrothermal vents at the Main Endeavour Field, Juan de Fuca Ridge: Phase equilibria and kinetic constraints, Geochem. Geophys. Geosyst., 10, Q10003, doi:10.1029/2009GC002472.

Germanovich, L. N., Lowell, R. P., and Ramondenc, P., (2011), Magmatic origin of hydrothermal response to earthquake swarms: Constraints from heat flow and geochemical data, J. Geophys. Res., 116, B05103, doi:10.1029/2009JB006588.

Harlow, F. H. (1957), "Hydrodynamic Problems Involving Large Fluid Distortions," J. Assoc. Comput. Mach. 4,137. Johnson, N. L. (1996), The legacy and future of CFD at Los Alamos, Proceedings of the 1996 Canadian CFD Conference, Ottawa, Canada June 3-4.

Johnson, H. P., M. Hutnak, R. P. Dziak, C. G. Fox, I. Urcuyo, J. P. Cowen, J. Nabelek, and C. Fisher (2000), Earthquake-induced changes in a hydrothermal system on the Juan de Fuca mid-ocean ridge, Nature, 407, 174177.

Johnson, H. P., M. A. Tivey, T. A. Bjorklund, and M. S. Salmi (2010), Hydrothermal circulation within the Endeavour Segment, Juan de Fuca Ridge, Geochem. Geophys. Geosyst., 11, Q05002, doi:10.1029/2009GC002957.

Kadko, D. and Moore, W. (1987), Radiochemical constraints on the crustal residence time of submarine hydrothermal fluids: Endeavour Ridge, Geochimica et Cosmochimica Acta, Vol. 52, pp. 659-668.

Kadko, D., J. Baross, and J. Alt (1995), Hydrothermal fluxes and global change, Physical, chemical, biological and geological itneractions within hydrothermal systems, AGU Mono, edited by Humphris, S., L. Mullineaux, R. Zierenberg and R. Thomson, Am. Geophys. Un., Washington, D.C.

Kelley, D. S., J. Baross, and J. Delaney (2002), Volcanoes, fluids and life at mid-ocean ridge spreading centers, Annu Rev. Earth Planet. Sci., 30, 385491.

Kump,L.R (2008), The Role of Seafloor Hydrothermal Systems in the Evolution of Seawater Composition During the Phanerozoic, Magma to Microbe: Modeling Hydrothermal Processes at Ocean Spreading Centers, Geophysical Monograph Series, 178, 0.1029/178GM14.

Lewis, K. C., and R. P. Lowell (2009a), Numerical modeling of two-phase flow in the NaCl-H2O system: Introduction of a numerical method and benchmarking, J. Geophys. Res., 114, B05202, doi:10.1029/2008JB006029.

Lewis, K. C., and R. P. Lowell (2009b), Numerical modeling of two-phase flow in the NaCl-H2O system: 2. Examples, J.Geophys. Res., 114, B08204, doi:10.1029/2008JB006030.

Lowell, R. P., A. Farough, J. Hoover, and K. Cummings (2013), Characteristics of magma-driven hydrothermal systems at oceanic spreading centers, Geochem. Geophys. Geosyst., 14, 17561770, doi:10.1002/ggge.20109.

MATLAB 2010b, The MathWorks, Inc., Natick, Massachusetts, United States.

Norton, D. (1978), Sourcelines, Sourceregions, and Pathlines for Fluids in Hydrothermal Systems Related to Cooling Plutons, *Economic Geology*, Vol. 73, pp. 21-28.

Ramondenc, P., L.N. Germanovich and R. P. Lowell (2008), Modeling the hydrothermal response to earthquakes with application to the 1995 event at 950N, East Pacific Rise, in Magma to Microbe: Modeling Hydrothermal Processes at Oceanic Spreading Centers, Geophys. Monogr. Ser., vol. 178, edited by R.P. Lowell et al., pp. 97-122, AGU, Washington, D.C.

Singh, S., R. P. Lowell, and K. C. Lewis (2013), Numerical modeling of phase separation at Main Endeavour Field, Juan de Fuca Ridge. Geochem. Geophys. Geosyst., 14, 40214034, doi:10.1002/ggge.20249.

Singh, S., R.P. Lowell (2015), The thermal response of mid-ocean ridges to perturbations, submitted to Deep Sea Res. II, Ref. no. DSR2-D-14-00089 (submitted).

Van Ark, E. M., R. S. Detrick, J. P. Canales, S. M. Carbotte, A. J. Haring, G. M. Kent, M. R. Nedimovic, W. S. D. Wilcock, J. B. Diebold, and J. M. Babcock (2007), Seismic structure of the Endeavour Segment, Juan de Fuca Ridge: Correlations with seismicity and hydrothermal activity, J. Geophys. Res., 112, B02401, doi:10.1029/2005JB004210.

Wolery, T., and N. Sleep (1976), Hydrothermal circulation and geochemical flux at mid ocean ridges, J. Geol., 84, 249275.

Appendix A

Formulation of the Single-Pass Model

The single-pass model shown in Figure 3.2 is considered one-dimensional because we only consider the distance between the deep recharge and the discharge point at the seafloor. The z- and x-axes in our model are directed along the fluid flow, that is, upward in the upflow zone and from right to left in the bottom horizontal limb following the convention of the cartoon shown in Figure 31. To write all the subsequent equations with respect to a unique coordinate along the fluid path in the deep horizontal limb and the upflow zone, we use a "curvilinear" coordinate s which is similar to that used in Ramondenc et al. [2008], where,

$$s = z, \qquad \text{if } s \leq H \tag{A.1}$$

$$s = z + x \quad \text{if } H < s \leq H + L \tag{A.2}$$

Meanings for all symbols can be found in Table S1.

For an easier formulation, we divide the fluid path into two main limbs, represented hereafter by the index i, where i takes values A.1 and A.2 representing the limbs as shown in Figure 3.2. Darcy's law in the vertical limb 1 can then be written as

$$v = -\frac{k(T)}{\eta(T)} \left[\frac{\partial P}{\partial s} - \rho_w(T) g \right] \tag{A.3}$$

For the horizontal limb 2, the same expression can be used without the gravity term $\rho(T)g$. The temperature T is a function of time t and coordinate s. Hereafter, we use the subscript when a physical value refers to a specific limb. Moreover, we consider that at any time step, the velocity v_i is constant in the i^{th} limb. This implies that the mass fluxes $Q_i = \rho A_i v$ are also constant in each limb at any time step. As ours is a single pass model, the value of Q remains constant for the entire flow path for one time step. Rewriting Darcy's law in terms of Q and using the kinematic viscosity, $\nu(T) = \nu(T)/\rho(T)$, we obtain

$$\frac{\partial P}{\partial s} = \frac{Q_i}{A_i}\frac{\nu(T)}{k(T)} + \rho(T)g \tag{A.4}$$

where the last term on the right-hand side is omitted for limb 2. The hydrostatic pressure at the bottom of the deep recharge zone can be written as

$$P(H+L) = P_0 + g\int_0^H \rho(T_{rech})ds \tag{A.5}$$

where and Trech is the far-field temperature in the deep recharge zone. Also, because pressure is continuous at s = H, we have:

$$P(H+L) - P_0 = \int_0^{H+L} \frac{\partial P}{\partial s}ds \tag{A.6}$$

We further take the hydrodynamic resistance as defined in Ramondenc et al. [2008]

$$r_1 = \int_0^H \frac{v(T)}{k(T)}\frac{ds}{A1} \tag{A.7}$$

$$r_2 = \int_0^L \frac{v(T)}{k(T)}\frac{ds}{A2} \tag{A.8}$$

where r_i is the resistance of the i^{th} limb. Combining (3), (4), and (5), and using conservation of mass, we finally obtain

$$Q1 = Q2 \tag{A.9}$$

$$Q1 = -\frac{g}{r_1 + r_2}\int_0^H [\rho_f(T_{rech}) - \rho_f(T)] \tag{A.10}$$

The temperature dependence of fluid viscosity η is approximated as [Germanovich et al., 2000]

$$\eta(T) = \frac{C_1}{T + C_2} \tag{A.11}$$

where $C_1 = 0.032$ Pa-s^{0}C, and $C_2 = 15.4^0$C. Finally, the dependence of fluid density on temperature is given by

$$\rho_f = \rho_0[1 - \rho_f(T - T_0)] \tag{A.12}$$

We now modify the formulation of Germanovich et al. [2000, 2001] and Ramondenc et al. [2008] to take into account the heat transfer from the magma body at the base of the hydrothermal system and to ignore the shallow recharge. Then, conservation of energy along the flow path 1-2 (Figure 3.2) can be written as

$$c_r\rho_r A\frac{\partial T}{\partial t} - c_f Q\frac{\partial T}{\partial s} = \lambda_r A\frac{\partial^2 T}{\partial s^2} - 2b(q_w + q_d) + bq_m \tag{A.13}$$

where q_m represents basal heat transfer from the magma body to the base of the hydrothermal system, q_w represents lateral heat transfer through the walls of the upflow zone, and q_d the heat from the freezing and cooling of a dike (when dike emplacement is modeled). Their asymptotic approximations are discussed by Germanovich et al. [2000] and can be written as follows:

$$q_w = -\frac{2}{\sqrt{\pi}}\frac{\lambda_r(T - T_{in})}{\sqrt{a_r t}} \tag{A.14}$$

$$q_d = \begin{cases} -\dfrac{\lambda_r}{\sqrt{\pi}erf(\lambda)}\dfrac{T_m - T}{\sqrt{a_r t}}, & \text{if } t < t_c \\ -\dfrac{\lambda_r(T_m - T)}{\sqrt{\pi}erf(\lambda)\sqrt{a_r t_c}}\exp(\dfrac{\pi^2 a_r(t - t_c)}{w^2}) & \text{if } t \geq t_c \end{cases} \tag{A.15}$$

The upper and lower expressions in equation A.15 correspond to the freezing and cooling stages after dike emplacement, t_c is the time for dike solidification, w is the dike width, and T_m is the temperature of the basalt melt emplaced by the dike. In equation A.15, λ is the root of equation $\lambda\exp(\lambda^2)erf(\lambda) = c_r(T_m - T)(L_m\pi^{0.5}))^{-1}$ [Carlsaw and Jaeger, 1986]. For typical parameter values (Table S1) and $T_m - T \sim 103^0C, \lambda \approx 1$ [Germanovich et al., 2000]. Then, for $a_r = 106$ m^2/s and $w = 1$ m, $t_c \sim 1$ day [Ramondenc et al., 2008]. When a dike is suddenly emplaced in fluid-saturated country rock, local boiling and phase separation may occur. However, the width of the two-phase zone is only ~ 10 cm [Lewis and Lowell, 2004], and hence we neglect it. In equation A.13, $q_m = 0$ everywhere except along the horizontal limb 2, where heat is conducted without heat loss through an impermeable

thermal boundary layer of thickness d. If T_m is the temperature of the magma body, then asymptotically [Germanovich et al., 2001; Lowell and Germanovich, 2004]

$$q_m = \frac{\lambda_r (T_m - T)}{d} \tag{A.16}$$

A.1 Boundary Conditions

At the deep recharge zone, we have the following boundary condition:

$$T = T_{rech}(H) \quad \text{if } s = H + L, t \geq 0 \tag{A.17}$$

The bottom boundary condition corresponds to the temperature at the bottom of the deep recharge. For our models, we assumed a linear gradient in the recharge zone with 0^0C at the seafloor, increasing 0.5^0C per m depth. We employ the radiative upper boundary condition on the seafloor derived by Germanovich et al. [2000]. This condition is written as

$$\frac{\partial T}{\partial s} = \frac{a_r}{v l^2}(T - T_0) \quad \text{at} \quad z = 0 \tag{A.18}$$

Where l represent the length scale for mixing between hydrothermal and cold seawater and a_r/v is the thermal boundary layer thickness for the continuum problem of heat transfer resulting from uniform upflow. Equation A.18 relates the heat transfer coefficient to the fluid velocity, so that at high velocity the temperature does not change much across the mixing zone, whereas at low velocity the fluid exits the seafloor near the ambient seawater temperature $T_0 \approx 0^0 C$. The parameter l is not well constrained but probably ranges from a few cm to m but not exceeding the thickness of the pillow lavas. The results depend only weakly on l for this range (see also examples given by Germanovich et al. [2000]). The examples presented in the paper generally correspond to $l \approx 20 - 30$ cm.

A.2 Initial Conditions

We define the initial conditions as the steady-state of the system prior to any perturbation. In steady-state, equation (A.13) becomes

$$-c_f Q \frac{dT}{ds} = \lambda_r A \frac{d^2 T}{ds^2} + b q_m \tag{A.19}$$

Since this equation does not include the permeability k, the k for our model is calibrated using the time dependent model. We use a reasonable value of permeability to start the simulation and then adjust it so that the value of Q obtained is within a reasonable range for the vent field in question. This value of initial permeability used in the model for further simulations.

A.3 Numerical Results

For solving the steady state equation, a finite difference scheme with a second order approximation is used. The Thomas algorithm is used to calculate the temperature in limbs 1 and 2 while imposing boundary conditions as discussed earlier. The steady state solution is used as a starting solution for the time dependent equations to minimize the time for reaching stability.

For solving the time-dependent equation, we chose an explicit numerical scheme that uses a finite difference discretization with a second-order approximation with respect to time. At each time step, the mass fluxes (and velocities) are considered to be constant. This takes into account that Darcy's law is a steady law and the time required for the flow to adjust to the new temperature and density are shown to be small. After each time step, the mass fluxes and velocities are recalculated, along with values of density and viscosity before the next step.

In all the calculations, we chose a uniform grid density with a grid spacing of 1 cm. We checked the accuracy of the computations by comparing the results with different grid spacing and time steps. The difference between the grids with a 10- and a 1-cm spacing did not exceed 1%. The time step was calculated using the Courant number in the simulations and set to 0.9 times of the calculated courant number. The program was implemented as a MATLAB 2010b [The MathWorks, Inc., Natick, Massachusetts, United States.] script. Our typical simulation for the 3-4 km-long spatial domain (upflow zone plus deep horizontal limb) required $\sim$ 30 min for 50000 time steps on a personal computer running with 2 GB RAM and Intel Celeron processor.

A.4 Generic Model of a Hydrothermal System

Following the steps listed above, we construct a generic model to demonstrate how the simulation was done step-wise. After setting the geometric parameters for the model (Table 3.1), the steady state equation is solved for Q $\approx$ 115 kg/s with an aim of obtaining surface temperature $\approx 370^0$C and temperature at depth $\approx 400^0$C. This results in d = 13 m (Equation A.13). These temperatures were chosen commensurate to surface temperature observations at mid ocean ridge sites and estimates of temperature at depth for mid ocean ridge systems [Jupp and Schultz, 2002].

The time dependent model is then run with no dike to calibrate the permeability (Equa-

tion A.13, $w = 0$). This makes the heat added by the dike (equation A.13) equal zero. We use the starting permeability $k = 3\text{x}10^{-13}m^2$ and after a few time steps Q stabilizes (Equations A.4 - A.10) for $k = 3.5\text{x}10^{-13}m^2$. After this step, we run the time dependent model for 50000 time steps to obtain a base line for the results. Subsequently, we run the simulation for dike width $w = 2$ m, dike height $h = 250$ m, and increase in permeability by 50 (Figure A.1 and A.2).

Like our models for EPR $9^0$50' N and MEF, the generic model shows a sharp increase in mass flow rate as well as surface temperature when permeability is increased.

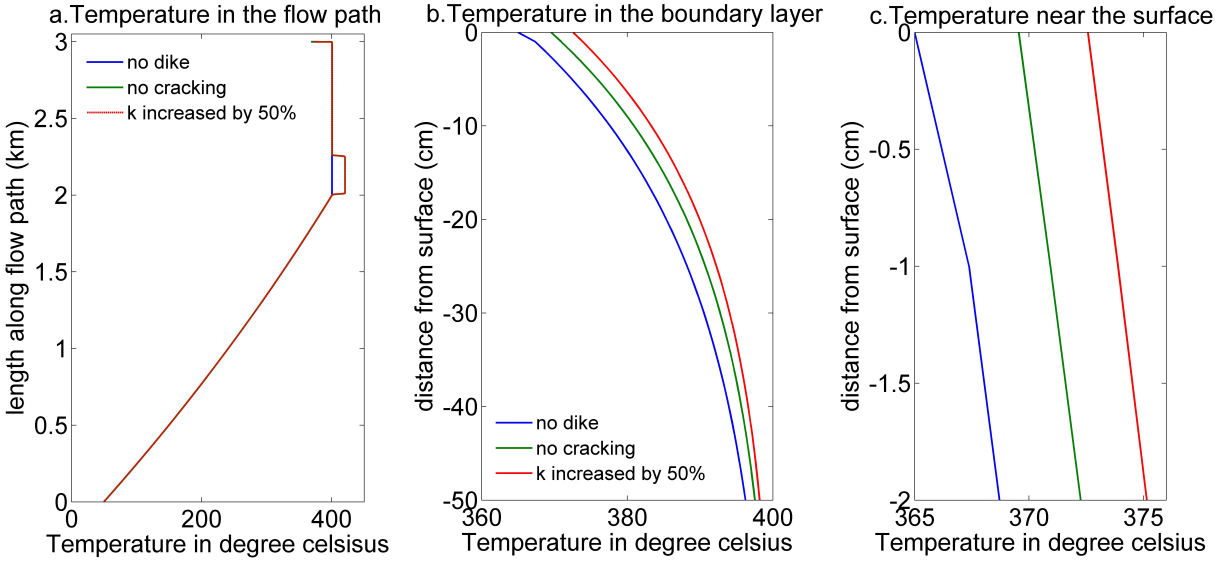

(a)

Figure A.1: Temperature distribution for the generic model in steady state (blue) and perturbed state for no diking scenario when k in the diking zone is increased by 50% (a) for the whole system for (b) for the boundary layer (c) near the surface. Values were plotted 25 days after the event.

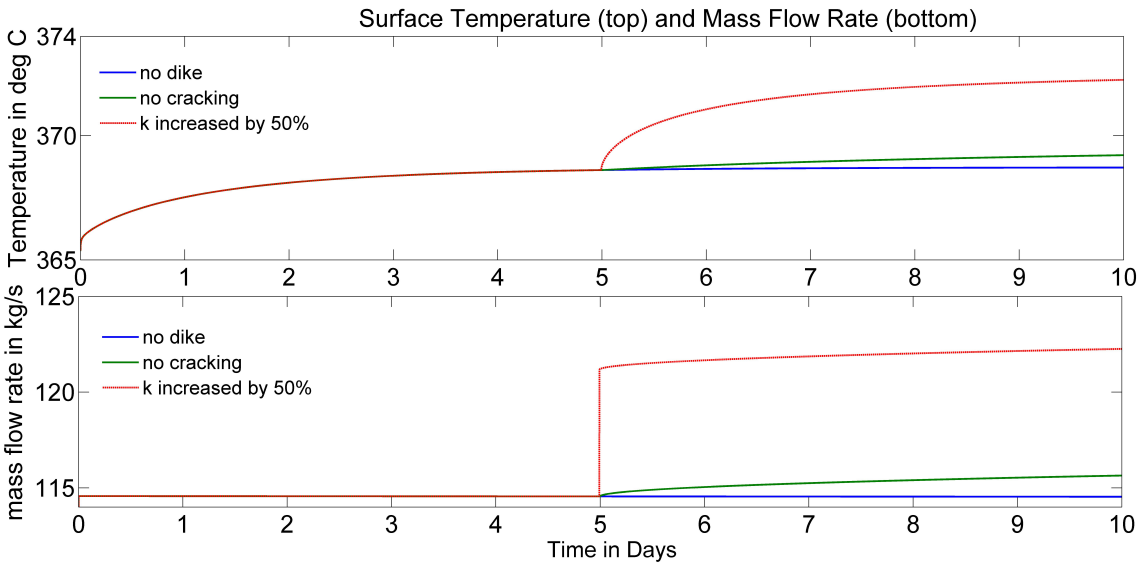

(a)

Figure A.2: Temperature at the surface (top) and mass flow rate (bottom) for the generic model in steady state (blue) and perturbed state (other colors) for no diking scenario when k in the diking zone is increased by 50%, 25 days after the event.

Appendix B

Particle in Cell Code

B.1 Main Code

Contents

- tracking parameters
- plotting axis
- declaring counters
- declaring arrays for speed
- time loops
- writing velocity values in suitable matrices
- creating an interpolant for velocity values
- querying the interpolant for velocity
- translating the particles
- plotting
- taking snapshots
- calculating del_t

```
clc
clear
load model_para.mat      % load model parameters
interpMethod = 'spline'; % declare the method for interpolating data
```

tracking parameters

```
track.startx = 0;       % first x coord for first point
track.startz = 0;       % first z coord for first point
track.dx = 20;          % gap between points
```

```
track.dz = 20;          % gap between points in z
track.numx = 1;         % number of points in the x dir
track.numz = 1;         % number of points in the z dir
track.endz  = 1500;     % maximum depth of the system, not used in code
n_t = length(time);     % number of time steps
[Pix,Piz] = track_points(track);    % function for tracking points
pxsize = size(Pix);                 % size of P x coordinate file
pzsize = size(Piz);                 % size of P z coordinate file
```

plotting axis

```
ax_minx = 400;
ax_maxx = 700;
ax_minz = 0;
ax_maxz = 1000;
```

declaring counters

```
m = 0;                      % counter
n_cx = n_z*(n_x-1);         % number of elements to be read into one array
n_cz = n_x*(n_z-1);         % number of elements to be read into one array
```

declaring arrays for speed

```
U = zeros(n_z,n_x-1);       % declaring an empty array for temp u values
V = zeros(n_x,n_z-1);       % declaring an empty array for temp v values

[X_x,Y_x] = ndgrid(dx/2:dx:max_x,0:dz:max_z);      % creating grid for u
[X_y,Y_y] = ndgrid(0:dx:max_x,dz/2:dz:max_z);      % creating grid for v

Pixt = zeros(pxsize(1),pxsize(2),n_t);  % for storing temporary x values
Pizt = zeros(pzsize(1),pzsize(2),n_t);  % for storing temporary z values

writerObj = VideoWriter('filename.avi');
writerObj.FrameRate = 20;               % frames per second
open(writerObj)                         % start writing video file
```

time loops

```
del_t = time(1)*365*24*3600;
for count = 1:17
```

writing velocity values in suitable matrices

```
    m = m+1;
    tot_t = time(m);
    % reading the correct x velocity for that time interval
    XliqVelInt = xv((n_cx*(m-1)+1):(n_cx*m));
    ZliqVelInt = zv((n_cz*(m-1)+1):(n_cz*m));

    for i = 1:1:n_x-1           % n_x-1 = 40
        for j = 1:1:n_z         % n_z = 31
            U(j,i) = 1*XliqVelInt((n_z*(i-1)+j),1);       % rows are formed by actual ro
        end
    end
    for i = 1:1:n_z-1           % n_z-1 = 30
        for j = 1:1:n_x         % n_x = 41
            V(j,i) = 1*ZliqVelInt((n_x*(i-1)+j),1);    % rows are formed by nx because t
        end
    end
```

creating an interpolant for velocity values

```
    u_interpolant = griddedInterpolant(X_x,Y_x,U',interpMethod);
    v_interpolant = griddedInterpolant(X_y,Y_y,V,interpMethod);
```

querying the interpolant for velocity

```
    u = u_interpolant(Pix, Piz);
    v = v_interpolant(Pix, Piz);
```

translating the particles

```
    Pix = Pix + u.*del_t;
    Piz = Piz + v.*del_t;
    Pixt(:,:,m) = Pix;
    Pizt(:,:,m) = Piz;
```

plotting

```
    p1 = plot(Pix, Piz, 'b');
    axis([0 max_x 0 max_z])
    %     axis([ax_minx ax_maxx ax_minz ax_maxz])
```

```
    title('Particles in the sub-surface', 'Fontsize', 15)
    xlabel('distance in meters','Fontsize', 15)
    ylabel('meters below seafloor','Fontsize', 15)
    set(gca,'YDir','Reverse')
    set(p1,'LineStyle','none')
    set(p1,'Marker','o')
    set(p1,'MarkerFaceColor','b')
    set(p1,'MarkerSize',5)
    hold off
    t1 = text(800,-50,['time=',num2str(tot_t,2),' years'], 'FontSize', 12);
    set(t1, 'FontSize', 14)
        drawnow
    frame = getframe(gcf);
    writeVideo(writerObj,frame);
```

taking snapshots

```
    b = mod(m, 2);
    if (b==1)
        filename = sprintf('disch_%d.png', round(m/2));
        saveas(gca, filename, 'png')
    end
```

calculating del_t

```
    if m == n_t
        break
    else
        del_t = (time(m+1)-time(m))*365*24*3600;
    end


end
close(writerObj)
```

B.2 Function: Track Points

```
function[Pix, Piz] = track_points(track)
Pix = zeros(track.numz,track.numx);     % array for storing x values
Piz = zeros(track.numz,track.numx);     % array for storing z values
mx = 0;
```

```
mz = 0;
for i = 1:1:track.numz
    mz = mz+1;
    mx = 0;
    for j = 1:1:track.numx
        mx= mx+1;
        Pix(i,j) = track.startx + track.dx*(mx-1);
        Piz(i,j) = track.startz + track.dz*(mz-1);
    end
end
Pix = Pix';
Piz = Piz';

end
```

B.3 Function: Writing Model Parameters

```
n_x = 41; % num nodes x
n_z = 41; % num nodes z
dx = 25;
dz = 25;
max_x = 1000;
max_z = 1000;
xv = load('x500xv_200');        % load x-velocity file
zv = load('x500zv_200');        % load z-velocity file
time = load('x500time_200');    % load time file
T = load('x500T_200');          % load Temperature file
save('model_para')              % save all infromation
```